UNIVERSITÀ DEGLI STUDI DI MILANO

Scuola di Dottorato in Fisica, Astrofisica e Fisica Applicata

Dipartimento di Fisica

Corso di Dottorato in Fisica, Astrofisica e Fisica Applicata

Ciclo 34$^{\text{th}}$

Atmospheric characterization for LSPE/Strip Observations

Settore Scientifico Disciplinare FIS/05

Supervisor: Professor Aniello MENNELLA

PhD School Coordinator: Professor Aniello MENNELLA

Tesi di Dottorato di:

Stefano Mandelli

Anno Accademico 2023-2024

Thesis Referees:

External Referee:
PARTRIGE Bruce

External Referee:
KESKITALO Reijo

Commission of the final examination:

MASI Silvia

BACCIGALUPI Carlo

MENNELLA Aniello

Final examination:

Date ??/September/2024

Università degli Studi di Milano, Dipartimento di Fisica, Milano, Italy

To my family and friends.

Cover illustration:

The Crescent Nebula - Stefano Mandelli - Virgo Observatory, Seveso, Italy, 2021.

Internal illustrations:

TBD

MIUR subjects:

FIS/05 - Astronomy and Astrophysics

PACS:

98.80.Es - Observational Cosmology

Contents

Motivation

I have looked for a way to structure this introduction for a long time. Finally, I decided to start describing who I am and the main traits that define my passions and motivations.

Since high school, I developed a keen passion for astronomy, prompted by a small optical telescope that I would use for observing the night sky. At the university, I understood that the Universe at optical range frequencies is just a small part of the whole picture. For this reason, I approached Cosmology, in particular the CMB observations.

It was just the beginning. My love for CMB (Cosmic Microwave Background) was total when I realized that the quantum processes that happened in the early Universe could be observable in the sky at cosmological scales. Thanks to inflation, the quantum-scale correlations of the Universe were stretched to cosmological ones, and now, we can observe them in the CMB, using “just” a telescope - *actually, a very sophisticated one!* -

It was clear that the CMB observations are one of the most essential scientific pieces of evidence for understanding the relation between the quantum and the cosmological scales, the fundamental physics, the Universe’s evolution, and how the Universe was born. What I have just described is super exciting and represents the core motivation of my work, but unfortunately, the motivation and being burdened with glorious purposes are not enough to make scientific results.

If we want to investigate what happened when the Universe was very young, we need a joint effort between different aspects of physics, from the small-scale process of quantum mechanics to the considerable evidence of the gravitational effects on the Universe’s large-scale structures. The scientists who have to deal with this question need to explore a wide range of energy scales to understand the quantum condition in the Universe 13.7 billion years ago, and a ground-based collider cannot explore those scales. The CMB is the unique “laboratory” that provides this information.

I started to work in the Observational Cosmology group of Milan, one of the leading groups in cosmological research in Italy and the world. Famous for the Planck satellite, the group is now involved in the next generation of CMB experiments. One of the projects is represented by the LSPE/Strip. It is a ground-based telescope that will observe CMB polarization from Teide Observatory (Tenerife).

Satellite experiments are the more advanced in data quality, but ground-based telescopes are still significant. Generally, a ground-based mission can operate longer than a satellite, and it is cheaper. Moreover, ground-based telescopes can be improved in time, repaired, and used to test new technologies and develop new techniques for future satellite missions.

In spite of that, the ground-based telescopes have to deal with *atmospheric emission* representing one of the most significant *spurious signal* for ground-based CMB polarization measurements. My PhD thesis is proficiently dedicated to this topic, which still represents an open field of research, in particular, applied to the modern technology of acquisition (telescope with large focal planes populated by thousands of detectors).

I aimed to improve my knowledge of this spurious noise with particular attention to the Strip telescope operations. The starting points were to create a reliable forecast of the atmospheric noise for Strip, recognize it in the *Time-Ordered-Data* - TOD -, and finally, mitigate it from the observations.

After three years, I can say that this work was super exciting. I could do practical work on the instrument, simulating its response and forecasting its systematics within one of the most crucial scientific frameworks that touch profound questions like describing the very early stages of our Universe and exploring new fundamental physics.

Chapter 1

Scientific Framework - Pills of Cosmology

The current understanding of the Universe is based on a wide set of observations, which together provide insight into its origin, composition and evolution during the last 13.7 billion years - Planck Collaboration et al. (2020).

The most widely accepted model of the Universe is called ΛCDM. It posits that in the far past the Universe was very dense, hot and in thermal equilibrium. It underwent an early phase of accelerated expansion leading to large-scale isotropy, homogeneity, and spatial flatness.

The evolution of the Universe can be predicted as a function of six base parameters whose values need to be fixed by experimental data. Current state-of-the-art values are based on Planck satellite measurements complemented by other cosmological probes (see Planck Collaboration et al. (2020) for the details).

In addition to the six base parameters, other variables can be taken into account for probing model extensions. For example, the tensor-to-scalar-ratio, r, which probes the relative amount of primordial tensor perturbations due to initial exponential expansion called *Inflation*. A summary of the main ΛCDM parameters is presented in table 1.1.

The aim of this chapter is to provide a brief introduction on the history of the Cosmological theories, from the first observations of the Universe to the current challenges of the ΛCDM model.

1.1 The ΛCDM model

Modern Cosmology started with the introduction of the homogeneous and isotropic model of the Universe proposed by Friedmann (1922) based on Einstein's general relativity. Subsequently, Hubble's observations, presented in Hubble (1929) and Hubble & Tolman (1935), on the receding velocity of the galaxies confirm the hypothesis of an expanding Universe. Hubble measured the receding velocities of the galaxies as a function of their distance from the observer using emission-line red-shift and cepheids.

Fig. 1.1 shows the measurements performed by Hubble (1929). The redshift z observed by Hubble is defined as

$$z + 1 = \lambda_{\rm obs}/\lambda_{\rm rest} \tag{1.1}$$

where $\lambda_{\rm obs}$ is the observed emission line of a specific element compared with the same emission line in the rest frame of the laboratory $\lambda_{\rm rest}$. Hubble observed how the red-shift

Table 1.1: Best-fit of the six ΛCDM parameters with confidence intervals at 68% from Planck+LENSING+BAO (Planck Collaboration et al. (2020)). The tensor-to-scalar ratio $r_{0.002}$ is given at 95% limits for some 1-parameter extensions to the ΛCDM model.

PARAMETERS	VALUE	DESCRIPTION
Base parameters		
$\Omega_b h^2$	0.02242 ± 0.00014	Baryon density
$\Omega_c h^2$	0.11933 ± 0.00091	Cold dark matter at the present-day
$100\theta_*$	1.04119 ± 0.00029	$100 \times$ approximation to r_*/D_A
τ	0.0561 ± 0.0071	Thomson scattering optical depth
n_s	0.9665 ± 0.0038	Scalar spectrum slope
$\ln\left(10^{10} A_\mathrm{s}\right)$	3.047 ± 0.014	Log power of the primordial curvature perturbations
Derived parameters		
H_0[km/s]	67.66 ± 0.42	The Hubble's constant
t_0 [Gyr]	13.787 ± 0.020	Age of the Universe
$r_{0.002}$	< 0.106	Tensor-to-scalar perturbation amplitude ratio
Ω_Λ	0.6889 ± 0.0056	Dark energy density scaled by ρ_crit at the present-day
Ω_m	0.3111 ± 0.0056	Matter density scaled by ρ_crit at the present-day
σ_8	0.8102 ± 0.0060	RMS matter fluctuations at the present-day, in linear theory
z_re	7.82 ± 0.71	Red-shift at which the Universe was half-reionised.
$10^9 A_\mathrm{s}$	2.100 ± 0.030	$10^9 \times$ dimensionless curvature power spectrum

was directly proportional to the galaxies distances and their receding velocity. As shown in the Hubble plot in Fig. 1.1, the velocity is proportional to the distance following the law

$$z = v/c \propto d. \tag{1.2}$$

Hubble measurements were interpreted in the context of the *General Relativity* where the dominant component of the red-shift, of distant galaxies, is due to the geometric expansion of the Universe.

In a condition of low red-shift, the link between d and z is given by $c\,z \sim H_0 d = v_r$ where H_0 is the Hubble's constant and v_r is the receding velocity of galaxies. The Hubble constant represents the expansion ratio of the Universe and, in Hubble & Tolman (1935), was first estimated $H_0 = 40 - 100$ [km/s].

In addition to Hubble's observations, the discovery of cosmic background radiation as predicted by the *Big-Bang* theory (Lemaître 1950; Alpher et al. 1948), played a crucial

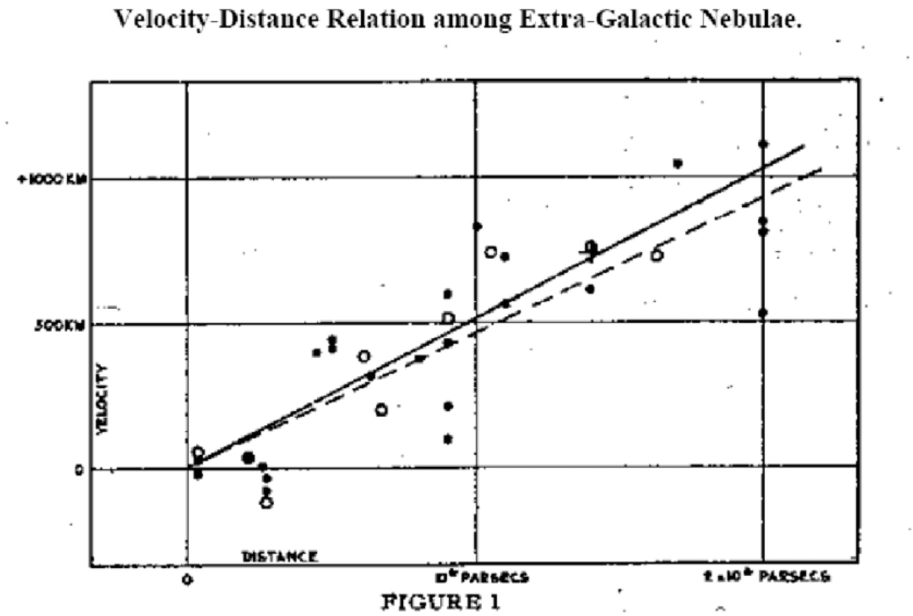

Figure 1.1: Hubble measurements of the receding velocity of the galaxies as a function of their distance from the observer (Hubble 1929).

role in supporting the hot origin of the Universe. This relic radiation was discovered by Penzias & Wilson (1965) in 1964.

Using a 4.2 GHz receiver coupled to a parabolic reflector (shown in Fig. 1.2), they detected an excess of $\sim 3\,\mathrm{K}$ in the antenna temperature that was eventually shown to have a cosmic origin. This signal was the *Cosmic Microwave Background* - CMB - radiation. These relic photons prove the hot Big-Bang origin of the Universe.

1.1.1 The Friedemann model

The theory of General Relativity posits that Hubble's observations were due to a geometric stretch of the space-time between us and the observed galaxy. This reasoning indicates that it is possible to study the evolution of the Universe passing through the study of its geometrical expansion.

The concept of *metric* is essential to give a mathematical description of the geometric evolution of the Universe. The *Friedmann-Lemaitre-Robertson-Walker* - FLRW - metric is used to introduce the scale factor in the metric tensor to consider the Universe's expansion Weinberg (1972). For a homogeneous and isotropic Universe, the metric is diagonal

$$g_{\mu\nu} = \begin{pmatrix} -c^2 & 0 & 0 & 0 \\ 0 & a^2(t) & 0 & 0 \\ 0 & 0 & a^2(t) & 0 \\ 0 & 0 & 0 & a^2(t) \end{pmatrix}. \tag{1.3}$$

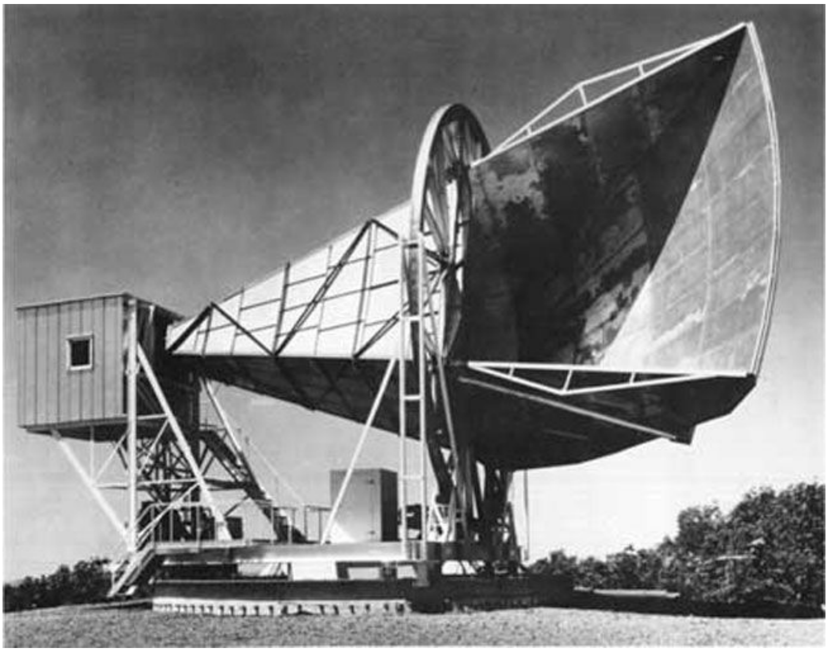

Figure 1.2: The antenna that was used by A.Penzias and R.W.Wilson in 1964 to discover the CMB. Bell Laboratory developed and manufactured the antenna in Holmdel - New Jersey. This antenna was a part of a communication system called Echo that exploited microwave bounces on a small satellite in LEO.

The *scale factor* $a(t)$ of the Universe represents its geometric evolution in time. The assumption of an isotropic Universe allows one to use spherical coordinates and the FLRW metric can be written (following Weinberg (1972))

$$ds^2 = -c^2 dt^2 + a^2(t) \left[\frac{dr^2}{1 - kr^2} + r^2 \left(d\theta^2 + \sin^2\theta \, d\phi^2 \right) \right] . \tag{1.4}$$

The equation of the FLRW metric, presented in eq. 1.4, is characterized by two terms with a dew The first one is the k term representing the curvature of space. The second one is the scale factor $a(t)$, and it multiplies the spatial part of the metric and works as an expansion term.

The term k is called *curvature term* and represents the geometry of the geodesic curves on which the particles move. It is possible to identify three different geometries: if the curvature term is $k > 0$, the curvature is positive, representing a closed, finite and bounded geometry. A negative curvature identifies $k < 0$, meaning an open and infinite geometry, while the case $k = 0$ identifies a zero-curvature, flat, geometry.

It is possible to deduce the dynamics using the field equation of the General Relativity, as described by Weinberg (1972). A more straightforward and valid approach can be made using Newtonian physics (Partridge & Partridge (1995), and Liddle (2015)).

In the left panel of Fig. 1.4, the origin O represents an observer on the Earth, and A and B are two galaxies. The Hubble's equation can be written, for each observer (located

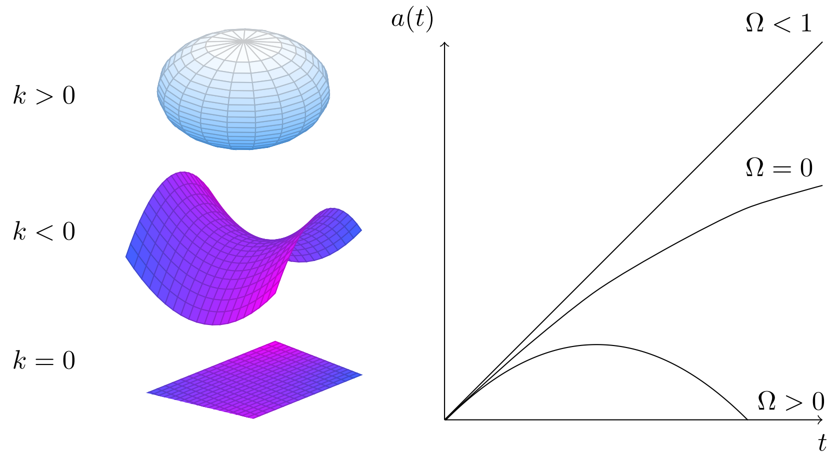

Figure 1.3: Different configurations and evolutions of the Universe as a function of the curvature parameter k and energy density $\Omega_{crit.}$. *The picture is created by TikZ, a LaTeXpackage for plotting functions*

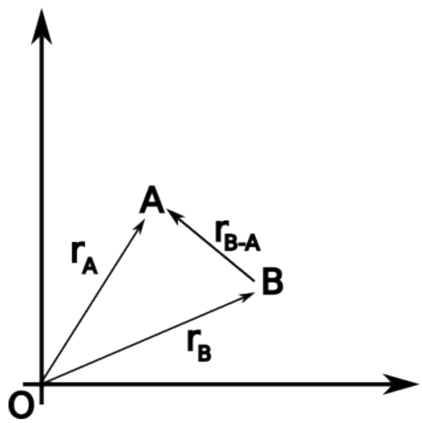

Figure 1.4: All the observers see galaxies expanding with the same Hubble's law

in O, A and B), in the same way

$$\vec{v}_{\mathrm{A}} = H_0 \cdot \vec{r}_{\mathrm{A}}, \text{ and } \vec{v}_{\mathrm{B}} = H_0 \cdot \vec{r}_{\mathrm{B}}, \tag{1.5}$$

where r and v are the position and velocity of the galaxies, respectively. In the same way, an observer of galaxy A sees the other galaxies expanding with the same law

$$v_{\mathrm{BA}} = v_{\mathrm{B}} - v_{\mathrm{A}} = H_0 \left(r_{\mathrm{B}} - r_{\mathrm{A}} \right). \tag{1.6}$$

A more convenient frame is represented by the *comoving coordinatates*. The distance between two galaxies can be expressed in terms of *comoving distance*, and in this frame, the scale factor $a(t)$ takes into account the expansion of the Universe. The Fig. 1.5 shows the distances between three different points. The actual distances between the points grow in time accordingly with the Universe expasion, while the comoving distances remain the same *1 unit* between point A-0 and *2 units* between point B-0. The Fig. 1.6 shows a

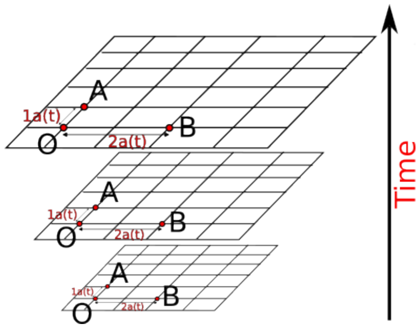

Figure 1.5: All the observers see galaxies expanding with the same Hubble's law

possible representation of massive points in the comoving frame. The masses, A, B, C, D, ... Using Birkhoff & Langer (1923) theorem, can be considered on a sphere-surface of unity radius where the gravitational force of the whole masses contained within the sphere is generated by the massive point in the origin O. Consider the acceleration of

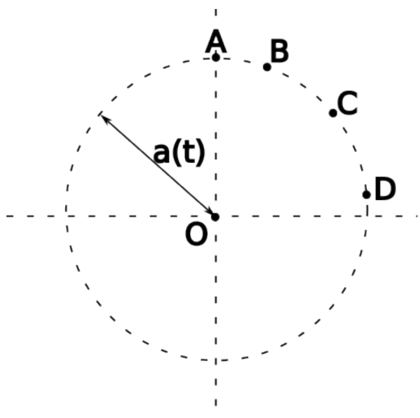

Figure 1.6: All the observers see galaxies expanding with the same Hubble's law

unit-mass on the sphere surface of radius $a(t)$ towards the origin O, that it is an arbitrary point in the expanding Universe. The acceleration on our unity mass sample is given by

$$\ddot{a}(t) = -\frac{GM}{a^2(t)}, \tag{1.7}$$

where M is the total mass contained in the sphere

$$M = \frac{4}{3}\pi a^3(t)\rho(t). \tag{1.8}$$

Note that eq. 1.8 depends on the density of the Universe at the time t. In this way, it is clear that the expansion ratio and the density of the Universe are connected.

In absence of radiation, the particles interact only due to their gravitational attraction. Under this assumption, the mass is conserved $V(t)\rho(t) = V(t_0)\rho(t_0)$. It leads to

$$\rho(t) = \frac{a^3(t_0)}{a^3(t)}\rho(t_0). \tag{1.9}$$

Consider the radius at t_0, $a(t_0) = 1$, and substitute the density expression in eq. 1.7. Using the simple chain rule of the derivatives

$$\begin{aligned} \ddot{a}\dot{a} &= \frac{d}{dt}\left(\frac{\dot{a}^2}{2}\right), \\ \dot{a}a^{-2} &= \frac{d}{dt}\left(-\frac{1}{a}\right). \end{aligned} \tag{1.10}$$

We can substitute the previous equations in this system of differential equations. Integrating to solve for $\dot{a}(t)$ the results is

$$\dot{a}^2(t) = \frac{8}{3}\pi G\rho_0 a^{-1}(t) + const. \tag{1.11}$$

The General Relativity solution connects the dynamics of the space expansion to the density and the curvature of the Universe. The integration constant *const.* is equal to $-kc^2$ and the final result for the scale factor is

$$\dot{a}^2(t) = \frac{8}{3}\pi G\rho_0 a^{-1}(t) - kc^2. \tag{1.12}$$

The eq.1.12 was derived using General Relativity principles. The present-day value of the curvature parameter is very close to zero. If we solve for $a(t)$ in the condition of $k = 0$ (de Sitter Universe) we obtain the solution for a matter-dominated Universe

$$a(t) \propto t^{2/3}, \tag{1.13}$$

and the present-day density of the Universe that corresponds to the critical density beyond which the Universe is closed and below which the Universe is opened. It is given by

$$\dot{a}^2(t_0) = \frac{8}{3}\pi G\rho_c a_0^2 \tag{1.14}$$

the Hubble's constant $H_0 = \dot{a}_0^2$ it is possible to obtain

$$\Omega_{crit} \coloneqq \rho_c = \frac{3H_0^2}{8\pi G} \tag{1.15}$$

The critical density ρ_c depends directly on the value of H_0. This allows ρ_0 to be directly connected to the curvature parameter. For example, the case $\rho_0 > \rho_c$ leads to a negative curvature and identifies a closed Universe model. In contrast, $\rho_0 < \rho_c$ leads to the open and ever-expanding Universe.

For these reasons, ρ_c represents a crucial parameter, and its knowledge plays an essential role in identifying the correct model of the Universe that accommodates the observations with the theory.

The ratio ρ_0/ρ_c is called *Critical Parameter* and is identified by a capital Omega Ω.

The curvature parameter k defines three different solutions:

$k > 0$ *Closed cosmological models*, include the re-collapse of the Universe. In the case of *high* density of the Universe, the expansion slows down due to the gravity attractive force until the reverse and the final re-collapse. It is shown in the Fig. 1.3 by the curve $\Omega > 0$.

$k < 0$ *Open cosmological models.* In this case, the Universe expands forever until its cold death. The Universe continues to increase the expanding ratio. It is represented in Fig. 1.3 by the curve $\Omega < 0$

$k = 0$ *Flat cosmological models.* It is a particular case of unlimited expansion. It is well known as the *Einstein-de Sitter* model that forecasts a uniform expansion of the Universe with a constant ratio. It is represented in the Fig. 1.3 by the curve $\Omega = 0$

A Universe composed of a mixture of matter and radiation

The radiation contribution is negligible at present-day but was fundamental in the early stages of the Universe.

Eq. 1.7 must be changed in order to take into account the density of radiation. It is possible to define the radiation density $\rho_\gamma = u/c^2$ where the u is the energy density, and $P = 1/3\, u$ its pressure

$$\ddot{a}(t) = -\frac{4}{3}\pi G(\rho + \rho_\gamma)a(t) = -\frac{4}{3}\pi G\left(\rho + \frac{u}{c^2}\right)a(t). \tag{1.16}$$

The radiation pressure P invalidates the conservation law in eq.1.9 that was based on the only mass conservation. In this framework, the mass-energy is conserved

$$\dot{\rho}(t) = -3\left(\rho + \frac{P}{c^2}\right)\frac{\dot{a}(t)}{a(t)}. \tag{1.17}$$

The eq. 1.16 and eq. 1.17 can be used to solve for $a(t)$. The result can be reached under the assumption that at the early stages of the Universe, the major contribution to the radiation density, was given by the CMB photons. Even if the CMB radiation has not been elaborated carefully yet, is possible to anticipate that ρ_γ is given by the CMB photons that are characterized by black-body emission spectrum. In this way, the energy density and pressure can be written

$$u = b\,T^4; \quad P = \frac{b}{3}T^4. \tag{1.18}$$

where b is a constant. The black-body emission curve depends only on λT and the dependency is straightforward reached

$$\rho_\gamma \propto u \propto T^4 \propto a^{-4}, \tag{1.19}$$

unlike the previous model with only matter where the matter density depends on the volume expansion

$$\rho_{matter} \propto a^{-3}, \tag{1.20}$$

the radiation density ρ_γ and the matter density ρ_{matter} depend on z with two different slopes. At the epoch of the early Universe ($z \sim 10^4 - 10^3$), the radiation played a dominant role compared with the matter, leading to the expansion of the Universe when $a(t)$ was smaller.

To emphasize better the role of the radiation and the matter it is possible to evaluate the ratio between

$$\frac{\rho_\gamma}{\rho_{matter}} \propto a(t)^{-1} \tag{1.21}$$

that depends on $(z+1)$. For a radiation dominated Universe the Einstein-de Sitter model ($k = 0$) returns a solution for $a(t)$

$$a(t) \propto t^{1/2}. \tag{1.22}$$

This equation rules the expansion of the Universe for the first thousand years after the Big Bang.

Introduction of the cosmological constant

Riess et al. (1998) and Perlmutter et al. (1999) observing supernovae, they reported an acceleration of the Universe expansion. The Perlmutter measurements are shown in Fig. 1.7. It shows an extension of Hubble's measurements up to $z \simeq 1$.

To explain the plot in Fig.1.7 the Einstein equations can be extended by introducing a term $\Lambda g_{\mu\nu}$ that preserves all the invariance. The effect of Λ depends on its sign, and it can be repulsive. Let's define $\Lambda/3$ in units of $[s^{-2}]$, the dynamic of the Universe can be written as follows

$$\begin{aligned} \ddot{a}(t) &= -\frac{4}{3}\pi\, G\, \rho\, a(t) + \frac{\Lambda}{3} a(t) \\ \dot{a}^2(t) &= \frac{8}{3}\pi\, G\, \rho\, a^2(t) + \frac{\Lambda}{3} a^2(t) - kc^2. \end{aligned} \tag{1.23}$$

Eq. 1.23 under the assumption that the Universe is dominated by Λ have the following solution

$$a(t) = \exp\left[\left(\frac{\Lambda}{3}\right)^{1/2} t\right] \tag{1.24}$$

that represents an *exponential expansion*. This result changes the context for describing the evolution of present-day Universe. Moreover, it is a probe for describing the present-day dark-energy (Guth 1981). Fig. 1.8 shows the analysis results of the supernovae measurements. A Universe with $\Lambda = 0$ is not compatible with observation and the measurements with supernovae point to a contribution of the cosmological constant of the order of $\Lambda \simeq 0.7$, and a matter contribution of $\Omega_m \simeq 0.2$

1.2 Thermal history of the Universe

The abundance of elements in the Universe provides the final proof of the hot origin of the Universe. The nucleosynthesis of the light elements, such as deuterium, helium, and

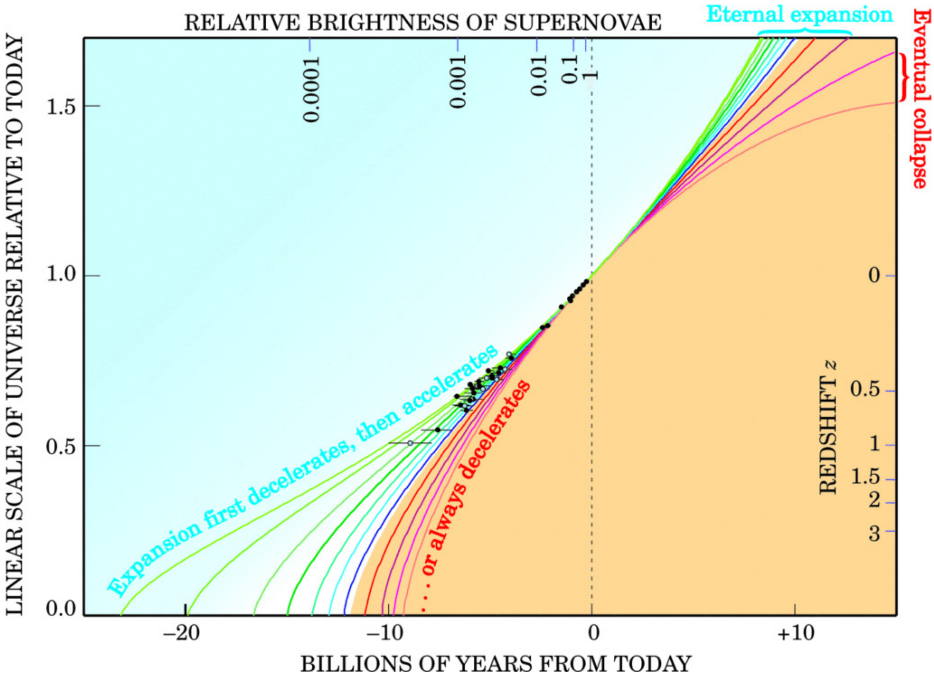

Figure 1.7: The evolution of the Universe assuming flat cosmic geometry. The scale factor $a(t) = 1$ for $t = t_0$ and scale as a function of the redshift as $1/(1+z)$. The curves in the blue region represent an accelerating Universe due to the possible domination of a cosmological constant. These curves span from $0.95\rho_c$ down to $0.4\rho_c$. The curves in the yellow region represent decelerating Universe models dominated by the mass. The mass density span up to $1.4\rho_c$, and for the last two curves the expansion halts and collapses.(Perlmutter et al. 2003)

lithium, can be explained by the hot Big-Bang model. The abundance of these elements is in agreement with the predictions of the Big-Bang model. The thermal history of the Universe is based on the extrapolation of the present-day knowledge of the Universe and particle physics back to the Planck epoch ($t \sim 10^{-43}$ sec).

The typical nuclear binding energy is around 1 MeV while the photons energies of the early Universe exceed this value so the nuclei will be immediatly disassociated and at the earliest times, the Universe was composed of a plasma of light elements. The formation of the nuclei took place when the Universe was 1 second old and this process is well kwown as *primordial nucleosynthesis*.

The balance between neutron and proton - $T \gg 1\,\mathrm{MeV}$ and $t \ll 1\,\mathrm{sec}$

At high temperatures the Universe contained protons and neutrons in thermal equilibrium. When the Universe started to cool down, the neutrons and protons started to combine to form deuterium, helium, and lithium. The balance between neutrons and protons is crucial for the formation of the light elements.

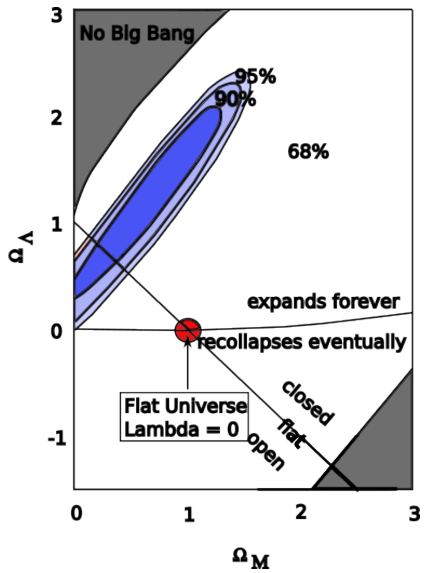

Figure 1.8: Constraint on the parameters $(\Omega_m, \Omega_\Lambda)$. The contribution of Ω_m and Ω_Λ is quantified from Type-Ia Supernovae. A curved Universe is allowed, with parameters corresponding to a flat Universe indicated by the line "flat". The model identified by the line "Flat,$\Lambda = 0$" is not allowed. The constraints from SNe require an accelerating Universe condition obtained for $\Omega_\Lambda > 0$.

When the Universe was $\sim 10^{-2}$ sec after the Big Bang, and the temperature as high as 10MeV the weak interactions maintained the balance between neutrons and protons

$$\begin{aligned} n &\longleftrightarrow p + e^- + \overline{\nu}_e, \\ \nu + n &\longleftrightarrow p + e^- \\ e^+ + n &\longleftrightarrow p + \overline{\nu}_e. \end{aligned} \tag{1.25}$$

In the condition where the rates for the weak interactions, described in eq. 1.25, are rapid compared to the expansion rate, the chemical potential of the neutron, neutrino, proton and electron, densities were in this simple relation

$$\mu_n + \mu_{\nu_e} = \mu_p + \mu_e. \tag{1.26}$$

The chemical equilibrium between neutrons and protons can be written as a function of their *mass-fraction*[1]

$$n/p := n_n/n_p = X_n/X_p \exp\left[-Q/T + (\mu_e - \mu_{\nu_e})/T\right] \tag{1.27}$$

where $Q := m_n - m_p = 1.293\,\text{MeV}$. We can state that $\mu_e/T \sim (n_e/n_\gamma) = (n_p/n_\gamma) \sim \eta = 10^{-10}$ because the Universe is neutral.

[1]The *mass-fraction* of a chemical species A(Z) is defined as $X_A := \mathrm{A} \cdot n_\mathrm{A}/n_N$ (where A is the mass and Z is the charge)

The electron neutrino number is related to μ_n/T, but the relic neutrino background has not been detected yet, and none of the neutrino lepton numbers is known. For this reason the lepton numbers are assumed small ($\ll 1$), so that $|\mu_{\nu_e}|/T \ll 1$. With these assumptions, the neutron-proton chemical equilibrium can be simplified in

$$\left(\frac{n}{p}\right)_{\rm EQ} = \exp\left[-Q/T\right]. \tag{1.28}$$

The rates (per nucleon per time) of interconversion of neutrons and protons, $\Gamma_{p+e\to\nu+n}$, due to the weak interactions can be obtained by integrating the transition rate probability. The matrix element in the transition rate probability is similar to the β-decay of the neutron, and it is weighted by the available phase-space densities of particles (for the details, see Kolb & Turner (2018)).

Comparing Γ with the expansion rate of the Universe we find that

$$\frac{\Gamma}{H} \sim \left(\frac{T}{0.8\,\mathrm{MeV}}\right). \tag{1.29}$$

When $T \gtrsim 1\,\mathrm{MeV}$ the weak interactions are more rapid than the expansion rate of the Universe and so the nuclear reactions building the light elements were in equilibrium.

Consider a system in which we are interested in knowing the density of protons, neutrons, deuterons, ^{3}He nuclei, ^{4}He nuclei and ^{12}C nuclei. At the nuclear statistical equilibrium, the mass fractions of the various nuclear species are given by:

$$\begin{aligned}
X_n, X_p &= \exp\left[-Q/T\right] \\
X_2 &= 16.3(T/m_N)^{3/2}\eta \exp\left[B_2/T\right] X_n\, X_p \\
X_3 &= 57.4(T/m_N)^{3}\eta^2 \exp\left[B_3/T\right] X_n\, X_p^2 \\
X_4 &= 113(T/m_N)^{9/2}\eta^3 \exp\left[B_4/T\right] X_n^2\, X_p^2 \\
X_{12} &= 3.22\,10^5(T/m_N)^{33/2}\eta^{11} \exp\left[B_{12}/T\right] X_n^6\, X_p^6 \\
1 &= X_n + X_p + X_2 + X_3 + X_4 + X_{12}
\end{aligned} \tag{1.30}$$

Where $B_{\rm A}$ is the binding energy of the nuclear species characterized by a nuclear mass A. The fact that light elements only form at energies much lower than 1 MeV is often identified as *the deuterium bottleneck*. At the nuclear statistical equilibrium, the densities of ^{4}He and ^{12}C (elements with much greater binding energy than deuterium) were low until temperatures below 0.3 MeV. It does not imply that the binding energy of deuterium is small but that the entropy of the Universe was very large.

The three steps of the production of the light elements

We can use the eq. 1.30 to describe the production of light elements in the Universe at different temperatures. We can identify three different steps:

- *Step-1* ($t = 10^{-2}$ sec. $T = 10\,\mathrm{MeV}$): The Universe was dominated by radiation. The relativistic particles that we can find at this epoch are positrons, electrons and the three species of neutrinos. These light elements were in nuclear statistical equilibrium, but they had a very small abundance ($\eta \sim 10^{-9}$). The components of the Universe were distributed in the following way

$$\begin{aligned} X_n, X_p &= 0.5 \\ X_2 &\sim 6\, 10^{-12} \\ X_3 &\sim 2 \times 10^{-23} \\ X_4 &\sim 2 \times 10^{-34} \\ X_{12} &\sim 2 \times 10^{-126} \end{aligned} \tag{1.31}$$

- *Step-2* ($t \simeq 1\,\mathrm{sec}$, $T = T_F \simeq 1\,\mathrm{MeV}$): During this epoch, the three neutrinos species decouple from the plasma, and little later the $e^{\pm}$ pairs annihilate. The protons and positrons entropy was transferred to the photons and thereby raising the temperature of the photons by a factor of $(11/4)^{1/3}$. During this period the weak interaction stops to interconvert neutrons in photons and vice-versa. The neutron-to-proton ratio remained quite constant and the light nuclear species were still in nuclear statistical equilibrium. A summary of the constitutes of the Universe is

$$\begin{aligned} X_n &\simeq 1/7 \\ X_p &\simeq 6/7 \\ X_2 &\simeq 10^{-12} \\ X_3 &\simeq 2 \times 10^{-23} \\ X_4 &\simeq \times 10^{-28} \\ X_{12} &\simeq 2 \times 10^{-108} \end{aligned} \tag{1.32}$$

- *Step-3* ($t = 1$ to 3 minutes, $T = 0.3$ to $0.1\,\mathrm{MeV}$): During this epoch, the neutron-to-proton ratio has decreased from $\sim 1/6$ to $\sim 1/7$ due to occasional weak interactions. At temperature $T = 0.3\,\mathrm{MeV}$ the nuclear statistical equilibrium of ^{4}He rapidly approached unity. Shortly before, the actual value of ^{4}He has fallen to the nuclear statistical equilibrium. This fact was due to the synthesis process of the ^{4}He, which was not fast enough to satisfy the steep increasing "Equilibrium demand" of ^{4}He. The synthesis process was not fast enough for two main reasons:
  - The abundance of D, ^{3}He, ^{3}H created an amount of these elements enough to reach (and exceed) their nuclear statistical equilibrium. The same abundance did not occur for heavier species that were used like "fuels" in the synthesis ^{4}He.
  - Columb barrier suppression started to be significant. The penetration of the Colomb barrier due to thermal processes presents a cross-section given by

$$\langle \sigma |v| \rangle \propto \exp\left[-2\overline{A}^{1/3}(Z_1 Z_2)^{2/3} T^{-1/3}\right] \tag{1.33}$$

    where $\overline{A} = A_1 A_2/(A_1 + A_2)$, and $\langle \sigma |v| \rangle$ is the thermally-averaged cross section times the relative velocity.

At the temperature of $T \sim 0.1\,\text{MeV}$, finally, the ^{4}He synthesis took place. The binding energy of ^{12}C and ^{16}O was large (compared with the binding energy of the ^{4}He). For this reason, the Colomb-barrier suppression was very significant. Moreover, the absence of tightly-bounded isotopes of mass 5 and 8 and the low nucleon density prevented significant nucleosynthesis beyond ^{4}He.

A significant amount of D, ^{3}He were left unburnt and their abundance is a valuable probe of the primordial nucleosynthesis.

1.3 The Cosmic Microwave Background

After 3 minutes from the Big Bang, the nucleosynthesis was over and the Universe started to cool down.

At this time, photons were still trapped in the continuous Thomson scattering interactions with the cosmic plasma, and the Universe appeared utterly opaque. At 380,000 years after the Big Bang, the temperature of the Universe had dropped enough to allow photons to decouple from matter and finally propagate in free space.

The photons that constitute the CMB are the photons that are firstly decoupled from matter and represent a radiation background, which today peaks in the microwaves. The CMB's peak in the microwaves is due to the expansion effect of the Universe.

1.3.1 The CMB emission spectrum

The CMB is characterized by an almost about black-body spectrum with some faint deviation that, at the present day, are foreseen by the theory but have never been observed yet. The black-body spectrum is obtained as a direct consequence of the thermal history of the Universe and in this section, we elaborate on the process that occurred to produce this kind of energy distribution.

For $z > 1000$ the matter was ionized and the photons scattered with the primordial plasma. The process that changes the photons' directions without changing their frequencies is Thomson scattering. Just the Thomson scattering is not enough to create a thermal spectrum.

The processes that could occur in the early Universe to relax a non-thermal spectrum into a thermal could be of two kinds:

- Creation of photons and energy redistribution in order that matter and radiation were in equilibrium;
- The reaction ratio of the previous process has to be larger than the expansion ratio of the Universe.

Both the conditions are met by the Hot Big-Bang model.

Let us assume the Universe after the last massive annihilation of couples $e^- + e^+ \to 2\gamma$. The equilibrium $e^- + e^+ \leftrightarrow 2\gamma$ was restored when the Universe was a couple of months old and the spectrum of the radiation, for $z \sim 10^9$, can be considered not distorted.

This statement can be relaxed because, independently of the emission spectrum of the radiation, for $z > 10^9$, it always relaxed into a thermal spectrum (Burigana et al. 1991a,b).

However, for $z < 10^9$ photon creation processes can be occurred via *Bremßtrahlung* and *Radiative Compton* scattering. The Bremßtrauhlung depends on the density of electrons and their energy. For these reasons, it was dominant at large z (when density and energy of the Universe were higher).

As shown by (Kompaneets 1957; Weymann 1965; Zeldovich & Sunyaev 1969; Sunyaev & Zeldovich 1970; Peebles 1971) the only Compton scattering can produce kinetic equilibrium and the photons scatter was characterized by time scale of

$$t_c = \frac{m_e c}{n_e\, \sigma_T K\, T_e} \approx 10^2 8 \left(\frac{T}{T_e}\right) \left(\Omega_b h^2\right)^{-1} (z+1)^{-4}\ sec. \tag{1.34}$$

It depends on the mass of the electron m_e, electrons density n_e and the baryon density Ω_b. It was dominant for

$$z_c \gtrapprox 10^4 \left(\frac{T}{T_e}\right)^{1/2} \left(\Omega_b\, h^2\right)^{-1/2} \tag{1.35}$$

Under the assumption that the initial spectrum ($z \sim 10^9$) was not too distorted, and a kinetic equilibrium was easily established for $z > 10^4$ with only Compton scattering (it is not needed a process of photon creation like Radiative Compton), the spectrum of thermal radiation that was constituted by photons (bosons) was driven by Bose-Einstein distribution

$$\eta = \frac{1}{\exp\left(h\nu/kT_e + \mu\right) - 1} \tag{1.36}$$

where η is the occupation number for a given energy state. The constant μ is the *chemical potential* and it is zero for a perfect black body spectrum. The previous equations ensure that for $z > z_c$ any kind of spectrum can be relaxed into a Bose-Einstein emission spectrum.

Moreover, also the works by Kompaneets (1957); Weymann (1965); Zeldovich & Sunyaev (1969); Sunyaev & Zeldovich (1970); Peebles (1971) show that for z high enogh the chemical potential tents to zero, and the spectrum relax into a perfect black-body emission.

To create thermal equilibrium the double Compton and Bremßtrauhlung processes must produce photons and redistribute them on the various energy levels.

The evolution of the chemical potential, as a function of the radiative Compton (RC) and Bremßtrauhlung (B) can be written following Burigana et al. (1991a)

$$\frac{d\mu}{dt} = -\frac{1.7}{\phi(\mu) M(\mu)} \int_0^\infty \left[\left(\frac{\partial\mu}{\partial t}\right)_B + \left(\frac{\partial\mu}{\partial t}\right)_{RC}\right] x_e^2\, dx_e \tag{1.37}$$

where the term $x_e := h\nu/kT$, and

$$\begin{aligned} \phi(\mu) = &\ \frac{1}{2.404}\int_0^\infty \frac{x_e^2 dx_e}{\exp x_e + \mu - 1}, \\ M(\mu) = &\ 3\frac{d}{d\mu}\ln f(\mu) - 4\frac{d}{d\mu}\ln\phi(\mu), \end{aligned} \tag{1.38}$$

and

$$f(\mu) = \frac{1}{6.494} \int_0^\infty \frac{x_e^3 \, dx_e}{\exp\left[x_e + \mu\right] - 1}. \quad (1.39)$$

Evaluating numeriucally $\partial\eta/\partial t$ in the Bremßtrahulung and double Compton cases, Burigana et al. (1991b) shows that $\mu \to 0$ for

$$z_{th} \gtrapprox 10^6. \quad (1.40)$$

Independently from the initial values of the chemical potential, this shows that the spectrum of the radiation for $z > z_{th}$ is thermal.

Spectral distortions

As shown in the previous section, any kind of energy distribution of the photons at $z > 10^6$ thermalized to a thermal spectrum. For this reason, the expected spectrum for CMB radiation has to be very close to a perfect Black-Body.

The state-of-the-art in CMB spectrum measurements is that measured by COBE-FIRAS (Fig. 1.9) which differs from a perfect black body less than 1% emphasizing the high level of homogeneity of the early Universe.

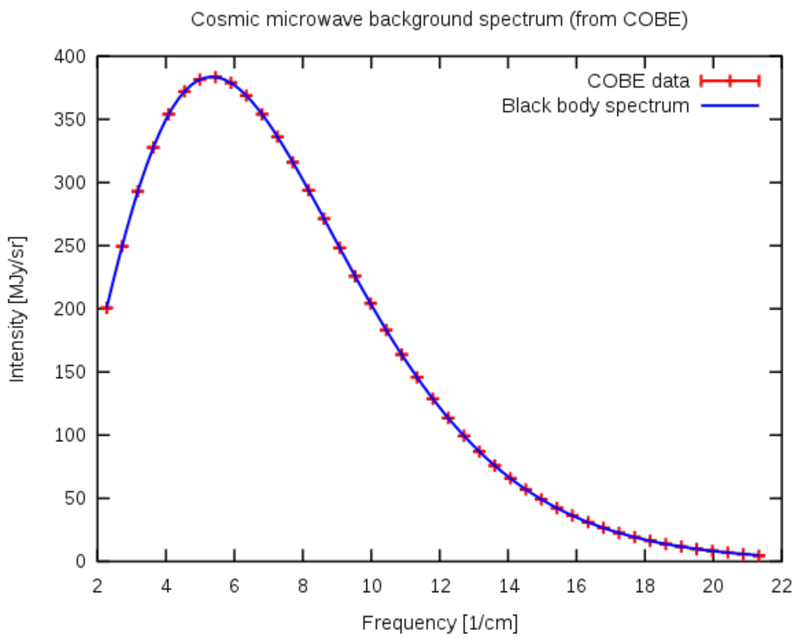

Figure 1.9: The CMB spectrum that was measured by the COBE-FIRAS spectrometer. In the picture, the measurements are represented by the red points. It is possible to appreciate that the measures do not significantly differ from a perfect Black-Body emission spetrum (Watts et al. 2018)

The possible processes that occurred $10^6 < z < 1$, and could distort the emission spectrum can be summarized in

- Energy released as primordial anisotropies. The loss of kinetic energy could be transformed into heat and so in photons.
- Energy released as smaller scale vorticity, turbulence, pressure waves or gravity waves were damped
- Gravitational energy released as galaxies of other large-scale structures formed
- The radiative decay of long-lived exotic particles
- Evaporation of primordial black-holes
- Scattering of the CMB radiation photons by electrons with a kinetic temperature higher than the CMB temperature (inverse Compton effect)

Future experiments devoted to measuring the CMB spectral distortions are already planned. For example, I report the COSMOS experiment leads by the University of Roma La Sapienza (Masi et al. 2021).

1.4 Inflationary Cosmology

The fundamentals described in previous sections were developed in the first half of '900, and they played a crucial role in describing the thermal history of the Universe. The CMB discovery in 1964 confirmed the hot origin of the Universe. Subsequent observations revealed three main limits of the Friedemann model:

i **Flatness of the Universe:** In the approximation of a Universe dominated by Radiation until now, the scale factor was $a(t) \propto t^{1/2}$. In this approximation, $(\Omega(t) - 1) \propto t$ means that the Universe rapidly depends on flatness. The flatness of the Universe that we can observe now would have been created only by a *particular conditions* that occurred for $t \approx 10^{-34} sec.$.

ii **Horizon problem:** The horizon problem arises from the observation of the high-level homogeneity of the CMB all over the sky ($\Delta T/T \sim 10^{-5}$). This level of homogeneity suggests causal interactions between the constitutions of the Universe until the recombination era. The comoving Hubble's radius at that time, projected on the angular distribution of the CMB, suggests a casual correlation only within $\sim 2\,\mathrm{deg}$. This could be possible only considering an extremely homogeneous Universe also before the recombination era.

iii **The CMB anisotropies:** The Big-Bang model assumes that the Universe is homogeneous and isotropic on a large scale. But this assumption contradicts the visible Universe around us, composed of a zone of high-density galaxies clusters and a large vacuum. The formation of these structures can be described only by considering a non-homogeneous Universe.

These limits were resolved using the Inflation paradigm introduced by Guth (1981). The inflation assumes that the Universe has gone through an accelerated exponential expansion phase when the Universe was between $t = 10^{-36}$ sec and $t = 10^{-34}$ sec.

Since the Inflation ended at some point we need a dynamic mechanism to manage the inflation regime's beginning and end. In summary, we need a clock for inflation.

1.4.1 A clock for the inflation: The Inflaton

Under the hypothesis of a homogeneous and isotropic Universe, we can consider it a perfect fluid. The energy-momentum tensor for the case of a perfect fluid can be written

$$T_{\mu\nu} = (\rho + P)u_\mu u_\nu + P g_{\mu\nu}, \tag{1.41}$$

where ρ is the density, P the pressure, u_μ is the 4-velocity of the fluid elements and $g_{\mu\nu}$ is the metric tensor. Using eq. 1.41, eq. 1.4 and Einstein's equation, the Friedmann equations can be written as

$$\begin{aligned} H^2 &= \frac{8\pi G}{3}\rho - \frac{k}{a^2} \\ \frac{\ddot{a}}{a} &= -\frac{4\pi G}{3}(\rho + 3P) \end{aligned} \tag{1.42}$$

where H is the Hubble parameter defined as $H = \dot{a}/a$. The only requirement to obtain an accelerated expansion of the Universe is $\ddot{a} > 0$. This constraint corresponds to obtaining a negative pressure of the primordial fluid $P < -\rho/3$.

In the case of $P \simeq -\rho$ the evolution of the scale factor is given by an exponential expression

$$a(t) = a_i \exp\left[H_i(t - t_i)\right] \tag{1.43}$$

where the subscript i indicates the beginning of the inflationary period. In this context is useful to introduce the Hubble's radius defined as

$$R_{\mathrm{H}} \coloneqq 1/H(t) \tag{1.44}$$

that identifies the size of the Universe causally connected at each time. In this case we can approximate $R_{\mathrm{H}} \propto ct$. In a *de Sitter* model the physical Hubble's radius is fixed in time while the physical lengths continue to grow thus being able to exit the Hubble's radius at some "horizon-crossing" time.

The requirement of sufficiently long inflation corresponds to that scales can exceed the Hubble's radius during the inflation.

Nowadays, the Universe does not appear in exponential expansion. For this reason, a sort of a *clock* has to be introduced to define the start and the end of the inflationary expansion.

The *Inflaton* (identified by the greek letter ϕ) is a scalar field introduced by A. Guth (Guth 1981) in 1981, to explain a possible dynamic of the starting of the inflation and how it ended. This scalar field can be introduced following Guth (1981); Partridge & Partridge (1995); Kolb & Turner (2018) in order to emphasize the work done by Linde (1982), and

Albrecht & Steinhardt (1982) to extend the Guth's work. At the present day, it is known as the *"new inflation"*.

Even if the nature of the scalar field ϕ is unknown, let us assume its existence and its interaction given by the potential $V(\phi)$. A possible potential shape is presented in Fig. 1.10.

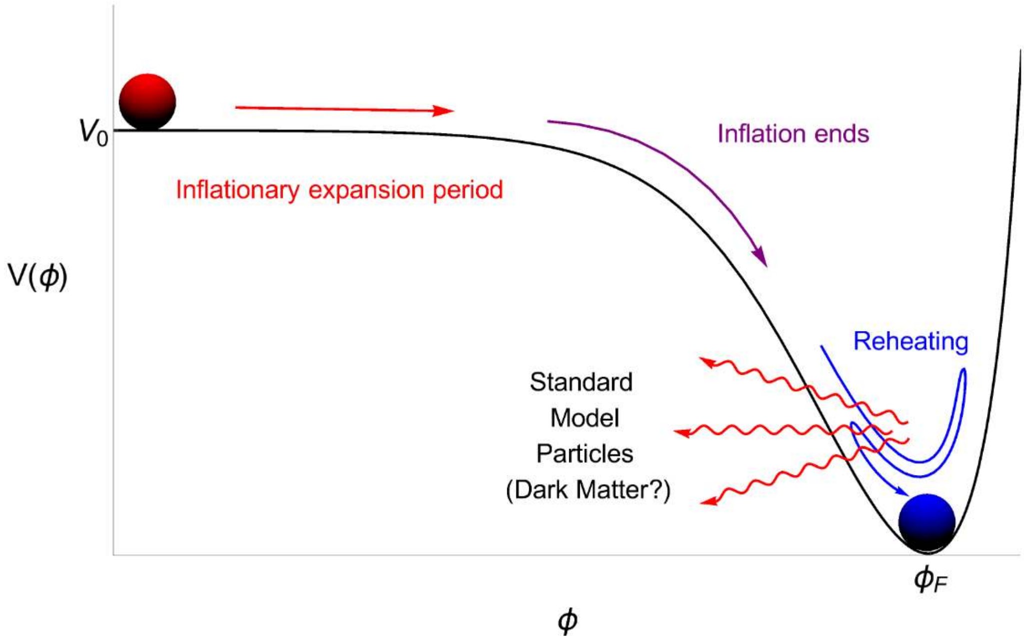

Figure 1.10: Inflaton potential in slow-roll regime. (Baumann 2009)

For $\phi = 0$, $V(0) \neq 0$, which represents the initial condition of the Universe. A minimum of $V(\phi)$ occurs for $\phi_F \neq 0$ and the slope of $V(\phi)$ for $0 < \phi < \phi_F$ is small for a wide range of ϕ.

If the product $\lim_{\phi \to 0} G\, V(\phi)/c^2$ is large, the expansion is exponential and the Universe is dominated by the Inflaton energy density.

In the assumption that the inflaton potential depends on the temperature, we can identify two different regimes. If the temperatures $T > T_*$, at the beginning of the inflation, the potential is described by a parabolic shape with a minimum in $\phi = 0$. At temperatures lower than $T < T_*$ the potential assumed a Mexican-hat shape. The minimum $\phi = 0$ did not satisfy the ground state condition and a phase transition occurred and the state moved from $\phi = 0$ to the real potential minimum.

Impact on the Friedmann equations and the scale factor

For a smmetry-breaking scale of 10^{14} GeV, the inflation is e^{100}, and it leads to an inflationary period duration of 10^{-32} sec. The energetic transition of the inflaton from high-energy state to the minimum did not occur instantly. The first step in the transition symmetry-breaking involves the presence of a barrier that has to be overcome.

As shown by Coleman (Coleman 1977), the process can proceed by quantum/thermal tunneling with the nucleation of bubbles. In some regions of the Universe, the scalar field ϕ was spatially uniform and far from the barrier still far from the minimum of the potential. One ϕ has made its way around the barrier, its evolution to the true vacuum is classical. In this case, it is possible to write a classical equation for the scalar field ϕ

$$\ddot{\phi} + 3\dot{\phi} + V'(\phi) = 0 \tag{1.45}$$

where the prime in $V'(\phi)$ is $\partial V/\partial\phi$.

The stress-energy tensor can be written as a function of the covariant derivatives. In the case of a flat Universe, the covariant derivatives are represented by the simple partial derivatives

$$T_\mu^\nu \left(\phi, \dot{\phi}\right) = diag(-\rho c^2, P, P, P) \tag{1.46}$$

where

$$\begin{aligned} \rho(\phi, \dot{\phi})c^2 &= \frac{1}{2}\dot{\phi}^2 + V(\phi) \\ P(\phi, \dot{\phi}) &= \frac{1}{2}\dot{\phi}^2 - V(\phi) \end{aligned} \tag{1.47}$$

The accelerated expansion has to be enough long to solve the flatness and horizon problems. In addition to the condition $V(\phi) \gg 1/2\dot{\phi}^2$, we need that $|\ddot{\phi}| \ll |3\mathrm{H}\dot{\phi}|$ to slow down the evolution. These conditions are known as *slow-roll* conditions. In this context, the Friedmann equations can be written

$$\begin{aligned} &3\mathrm{H}\dot{\phi} + V'(\phi) = 0 \\ &|\ddot{\phi}| \ll |3\mathrm{H}\dot{\phi}| \end{aligned} \tag{1.48}$$

It explains large-scale homogeneity and the flatness of the Universe ($k \sim 0$).

In this context, we can explain the initial energy density $V(\phi \sim 0)$ like vacuum energy density

$$V(\phi \sim 0) = \frac{\eta E^4}{(\hbar c)^3} \tag{1.49}$$

where η is a dimensionless number (Kolb & Turner 2018). From a point of view of Universe dynamics, the equation for $\dot{a}(t)$ becomes

$$\dot{a}(t) = \frac{8\,\pi\, G}{3c^2} V(\phi \sim 0)\, a^2(t) = \frac{8\pi\,\eta\, G\, E^4}{3\,\hbar^3\, c^5}\, a^2(t) \tag{1.50}$$

$$a(t) = \exp\left[\left(\frac{8\pi\eta\, G\, E^4}{3\,\hbar\, c^5}\right) t\right]. \tag{1.51}$$

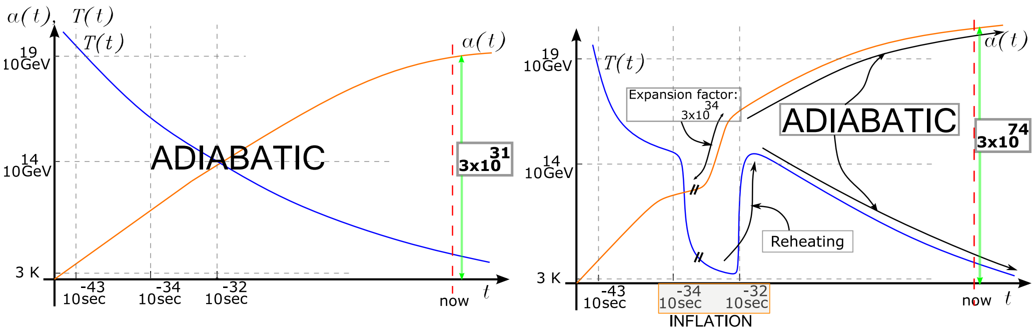

Figure 1.11: Comparison of the time evolution of the scale factor $a(t)$ and temperature in the Big Bang cosmology (left panel) and in the inflationary cosmology (right panel). At the end of the inflation, the entropy of the Universe varies with a very steep inclination ($\propto a^3T^3$)

1.4.2 Gravitational Wave production

The inflation theory not only answers the problem of the flatness and horizon. It permits a description of the primordial fluctuation of the scalar field ϕ. The scalar perturbations of the metric are coupled to the density perturbations of the primordial plasma. These perturbations can be considered the first seeds of the large-scale structures that we see now in our Universe.

The tensor perturbations are not coupled with the density matter therefore they are not involved in the formation process of the large-scale structures. The tensor perturbations of the metric are coupled to the gravitational-waves formation that left anisotropies onto CMB. These anisotropies turn out to be a unique pattern in the CMB polarization. if they will be detected, they represent a smoking gun in favor of the inflation theory.

The canonical quantization, in this context, is particularly useful because permits the introduction of annihilation and creation operators. The definition of these operators is very simple and their linear combinations can be managed in order to construct very complex operators (called *field operators*). The dynamic and the expectation values of these complex operators, using this formalism, can be evaluated using Gell-Mann and Low theorem (Molinari 2007) and Wick's contractions (Wick 1950). The dynamic of the system is described in terms of the evolution of the field operator that describes the system interations at the ground state. The dynamic is straightforwardly formalized using Heisenberg's picture[2].

For example, consider a harmonic oscillator

$$\frac{d^2\widehat{x}}{dt^2} + \omega^2\widehat{x} = 0. \tag{1.52}$$

The $\hat{x}$ is the field operator that represent the general interaction defined by $\hat{x}$, and it can

[2]The Heisenberg picture, also known as Heisenberg-Langevin's equation, is discussed by any book of the quantum mechanic. I can suggest Fetter & Walecka (2012); Landau & Lifshitz (2013)

be rewritten as a function of the constructor and annihilation operator $\hat{a}^\dagger$ and $\hat{a}$

$$\hat{x} = v(\omega, t)\hat{a} + v^*(\omega, t)\hat{a}^\dagger \tag{1.53}$$

Detailed structures of the field operators and definition of canonical commutation rules - CCR - are discussed in Appendix-A.

The expectation value is represented by

$$\langle \hat{x}^2 \rangle = |v(\omega, t)|^2 \tag{1.54}$$

that in this case, for the oscillator in eq. 1.52 the variance is $1/2\omega$.

Now we have to deal with infinite harmonic oscillators, one for each Fourier mode $\vec{k}$. Every modes is coupled with a pairs of annihilation and creation operators $\hat{a}, \hat{a}^\dagger$.

The evolution of these operators is described by a combination of negative and positive frequencies. The vacuum expectation is independent of time and position and can be subtracted (no real particles are produced). The vacuum state is evolving due to expansion. The first particles produced were the *Gravitons* that form the gravitational waves. The variance of that fluctuations is directly connected to the power spectrum of the fluctuations due to the production of gravitational waves. The perturbation of the metric, following the representation described by Dodelson (2003), can be written as

$$\delta g_{ij} = a^2(t) h_{ij}^{TT}(t, x), \;\; h_{ij}^{TT} = \begin{pmatrix} h_+ & h_\times & 0 \\ h_\times & -h_+ & 0 \\ 0 & 0 & 0 \end{pmatrix} \tag{1.55}$$

where h_+ and $h_\times$ are two functions that are considered small. The perturbation of metric, represented in eq. 1.55, is simplified because the oscillation of the perturbations is constrained on the $x - y$ plane, and consequently the wave-vector $\vec{k}$ is directed in the z direction.

The perturbed metric tensor is described by the two functions h_+ and $h_\times$ each of which follow

$$\ddot{h} + 2\frac{\dot{a}}{a}\dot{h} + k^2 h = 0 \;\; (h = h_+, h_\times). \tag{1.56}$$

try to resolve this equation like a quantum harmonic oscillator

$$\hat{\tilde{h}}(\vec{k}, \eta) = v(k, \eta)\hat{a}_k + v * (k, \eta)\hat{a}_k^\dagger \tag{1.57}$$

Following the note in Appendix-A, the operator $\widehat{\tilde{h}}$ is the field-operator[3] of the tensor perturbations. The expectation value is given by

$$\begin{aligned} \langle \widehat{\tilde{h}}^\dagger, \widehat{\tilde{h}} \rangle &= \frac{16\pi G}{a^2} |v(k, \eta)|^2 (2\pi)^3 \delta_D^{(3)}(\vec{k} - \vec{k}') \\ &:= P_h(k, \eta)(2\pi)^3 \delta_D^{(3)}(\vec{k} - \vec{k}') \end{aligned} \tag{1.58}$$

where $P_h(k, \eta)$ represents the power spectrum of the tensor perturbation produced by the gravitational waves.

[3]Bacause it is composed by a linear combination of annihilation and creation operators

In this section we have seen, starting from the perturbation of the metric, how is possible to evaluate the correlation between them. It was discussed by a theoretical point of view, but from an instrumental outlook, we have to assess the observables that can be measured to prove the theory. Since this work has a deep roots in the experimental and instrumental observation of the CMB, The chapter is devoted in describing the CMB observation concerns and the cosmological informations that we can extract by its features.

Chapter 2

The CMB observation

A. Penzias and R. Wilson measured the CMB as homogeneous background radiation of $\sim 3\,\mathrm{K}$. After the CMB discovery, the technological development of the radiometers permits the detection firstly of the *temperature anisotropies* and then Kovac et al. (2002) the CMB *polarization anisotropies*.

The largest temperature anisotropy that we can measure is the *dipole*. This anisotropy has not a cosmological origin but is due to the motion of the Earth in the rest frame of the CMB. For satellite experiments, the dipole works as a calibrator.

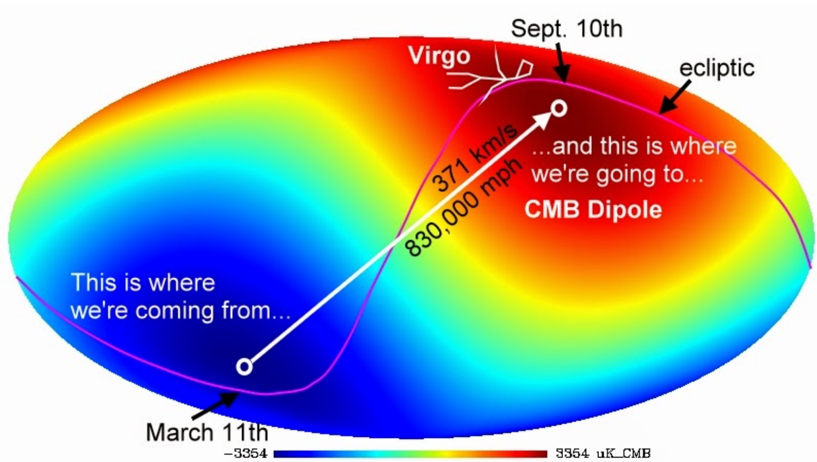

Figure 2.1: The picture shows the CMB dipole in temperature. The anisotropy in temperature is of the order of $3354\mu K \pm 24\mu K$ and it is due to the motion of the Solar System with respect to the CMB rest frame. It is directed towards the Virgo constellation at roughly $371km/s$. In the same way, we can evaluate also the movement of the center of our galaxy which is roughly $600km/s$ towards the same direction.

2.1 The Dipole

On the celestial sphere this kind of anisotropy is represented by the spherical harmonics with $l = 1$ and this is the representation of a dipole. This anisotropy hides a deep physical meaning because by analyzing the dipole direction and magnitude we can create a model of the movements of the solar system with respect to the rest frame of the CMB.

Figure 2.1 shows the magnitude and direction of the dipole. The colors represent the dipole temperature in μK_{CMB}. The red zone represents a slight increase in temperature that corresponds to a blu-shift and it represents the direction where we are going. The blue zone represents the opposite direction and it is the direction where we are coming from.

The magnitude and direction of the dipole are not compatible with the composition of the movements of the sun in our galaxy and our galaxy in the Local Group. The dynamic is more complicated and it is represented in Fig. 2.2.

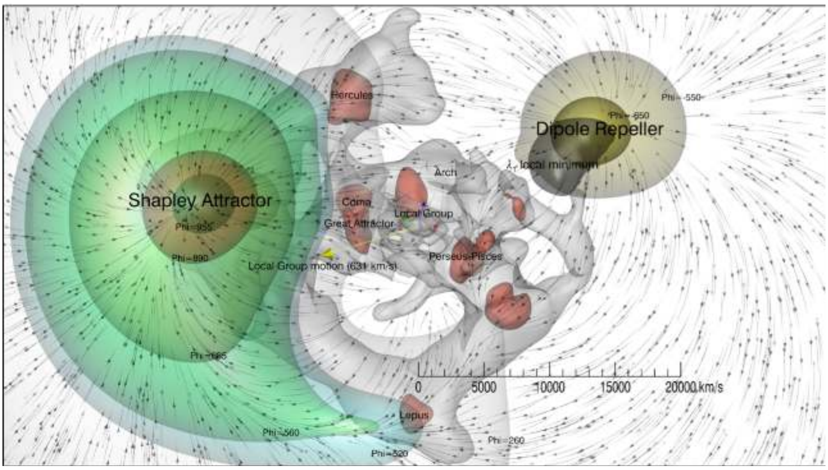

Figure 2.2: Three different elements of the flow are presented: mapping of the velocity field utilizing streamlines, red and grey surfaces presenting the knots and filaments of the V-web, respectively and equipotential surfaces are shown in green and yellow. The potential surfaces enclosing the Dipole Repeller (in yellow) and the Shapley Attractor (in green) dominate the flow. The yellow arrow indicates the direction of the CMB dipole. (Hoffman et al. 2017)

The galaxies move within a complex network of large-scale structures. The *Shapley Attractor* dominates largely (but not completely) the flow of the Local Group. It is located in the Shapley Supercluster of galaxies and it is characterized by an extremely large density. Moreover, the Local Group is affected by other close density regions like the gravitational influence of the other galaxies in the Local Group and by the *Great Attractor* in the Coma and by the *Perseus-Pisces* galaxies clusters. The result is a non-trivial composition of flows given by the mass distribution represented in Fig. 2.2. This image is taken by the work of Hoffman et al. (2017).

2.2 High order anisotropies

In the previous section, I presented the well-accepted model of the Universe and its evolution. The scientific focus is on the Hot Big-Bang origin of the Universe, and its subsequently exponential expansion due to inflation.

The eq. 1.58 represents the statistics of the tensor perturbation due to the primordial gravitational waves. It is possible to evaluate how these perturbations affect the CMB radiation and temperature and polarization patterns that are correlated with the physical processes that happened in the early Universe.

The representation of the Universe is given by the cosmological parameters that are the degrees of freedom of the model and can be evaluated as the best fit between the CMB observations (in particular the statistics of the temperature and polarization anisotropies) and those expected by the theoretical model.

The procedure that is adopted consists of the construction of the CMB temperature/polarization anisotropies using a two-point angular correlation function and comparing that with the correlation function predicted by the model.

For the case of temperature anisotropies, in Fig. 2.3 is represented the temperature fluctuations measured by Planck satellite (LIV 2018).

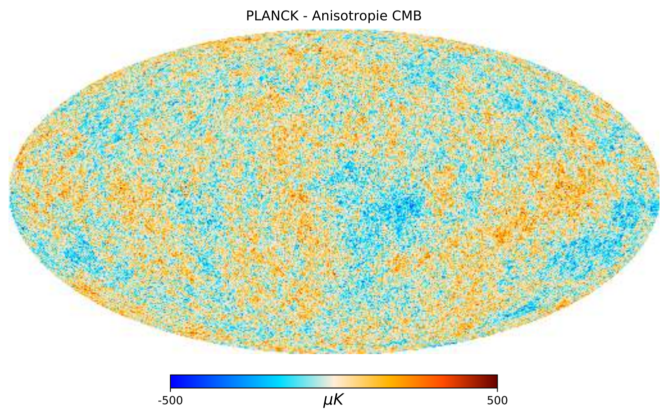

Figure 2.3: Temperature anisotropies measured by Planck satellite

The anisotropies on the sky can be expanded in spherical harmonics

$$\frac{\Delta T(\alpha,\beta)}{\bar{T}} = \sum_{l=0}^{\infty} \sum_{m=-l}^{+l} a_{lm} Y_{lm}(\alpha,\beta) \tag{2.1}$$

where $\Delta T(\alpha,\beta)$ represent the temperature anisotropy, respect to the CMB average $\bar{T}$, measured in the point of the sky of coordinates (α,β).

The two-points correlation function can be written as

$$\langle a^*_{l,m}, a_{l'm'} \rangle = \delta_{l,l'} \delta_{m,m'} C_l. \tag{2.2}$$

The CMB power spectrum is given by all the C_l coefficients for different angular scales l. if the two points of the correlation function are both temperature fluctuations, the C_l coefficients represent the TT spetrum.

In Fig. 2.4 is shown the CMB angular power spectrum for the temperature anisotropies.

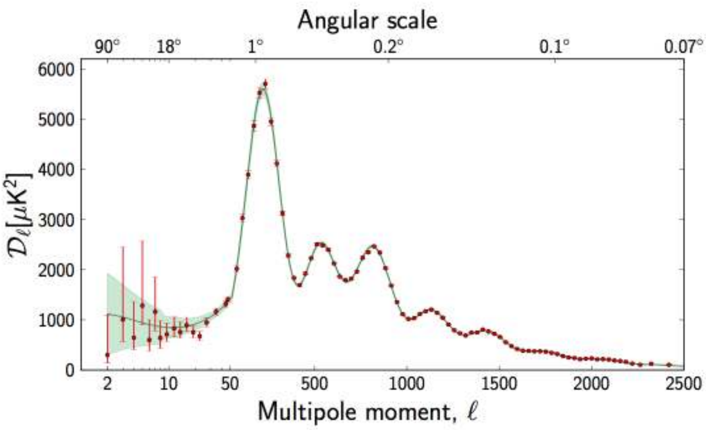

Figure 2.4: Temperature power spectrum measured by PLANCK satellite

The maximum likelihood with the angular power spectrum forecasted by the theory returns the cosmological parameters. Planck satellite measured that with unprecedented precision, in particular

- **Hubble's constant:** the expansion ratio of the Universe

$$H_0 = (67.8 \pm 0.9)\mathbf{km\ s}^{-1}\mathrm{Mpc}^{-1} \tag{2.3}$$

- **Baryonic Acoustic Oscillation (angular scale):** The measure of the seven acoustic peaks permitted to evaluate the tipycal BAO angular scale

$$\theta_* = 0.59636° \pm 0.00027° \tag{2.4}$$

- **Baryonic density:** The density of the baryonic matters depends on the height of the baryonic peaks

$$\Omega_b h^2 = 0.02222 \pm 0.00023 \tag{2.5}$$

- **Dark matter density:** Even the dark matter density can be extracted by the acoustic peak height

$$\Omega_c h^2 = 0.1197 \pm 0.0023 \tag{2.6}$$

- Dark energy limit: Planck estimated the dark energy limit at

$$\Omega_\Lambda = 0.685 \pm 0.013 \tag{2.7}$$

- **Spectral index:**

$$n_s = 0.9655 \pm 0.0062 \tag{2.8}$$

- **Optical depth:** depends of the Thomson optical depth at the re-ionization era. Planck measured the optical depth

$$\tau = 0.078 \pm 0.019 \tag{2.9}$$

The CMB polarization is evaluated at the same way using the spherical harmonic with spin=2 because the polarization fields is a "handless" vector field. The polarization can be written in term of Stokes parameters and the polarization tensor

$$\mathbf{P} = \begin{pmatrix} Q & U \\ U & -Q \end{pmatrix} \tag{2.10}$$

Using the tensor decomposition theorem can be written as a function of two kinds of spherical harmonics

$$P(\alpha, \beta) = \sum_l \sum_{m=-l}^{+l} a_{lm}^E Y^E(\alpha, \beta)_{l,m} + a_{lm}^B Y^B(\alpha, \beta)_{l,m} \tag{2.11}$$

Fig. 2.5 shows the current state-of-the-art of the CMB angular power spectra measurements for temperature and polarization anisotropies. The black points represent the performance forecast of the LiteBIRD satellite that will be launched at the end of the 2020s decay.

The temperature power spectrum at the medium scale $2 < l < 500$ was covered by WMAP and Planck satellites. Recently, the high multipole orders have been covered by the large ground-based telescope with a high optical resolution like ACT, POLARBEAR, BICEP/Keck and SPT.

In the same way, the scalar polarization spectrum E-modes (EE-spectrum) is almost complete along with the whole order of multipoles.

The B-modes (BB spectrum) due to the lensing and the primordial gravitational waves are partially covered only for high multipole orders where the lensing contribution is dominant.

The instrumental cosmology is dealing with the measurements of the B-modes power spectrum because for low l, the contribution of the lensing is minimum and can be observed in the large-scale structures of the polarization due to the primordial gravitational waves.

The detection of the B-modes represents a great challenge for modern cosmology because their detection will firmly confirm the inflation theory. For this reason, the aspect of the polarization is worth to be elaborated on in the detail and it is what I am going to do in the next section.

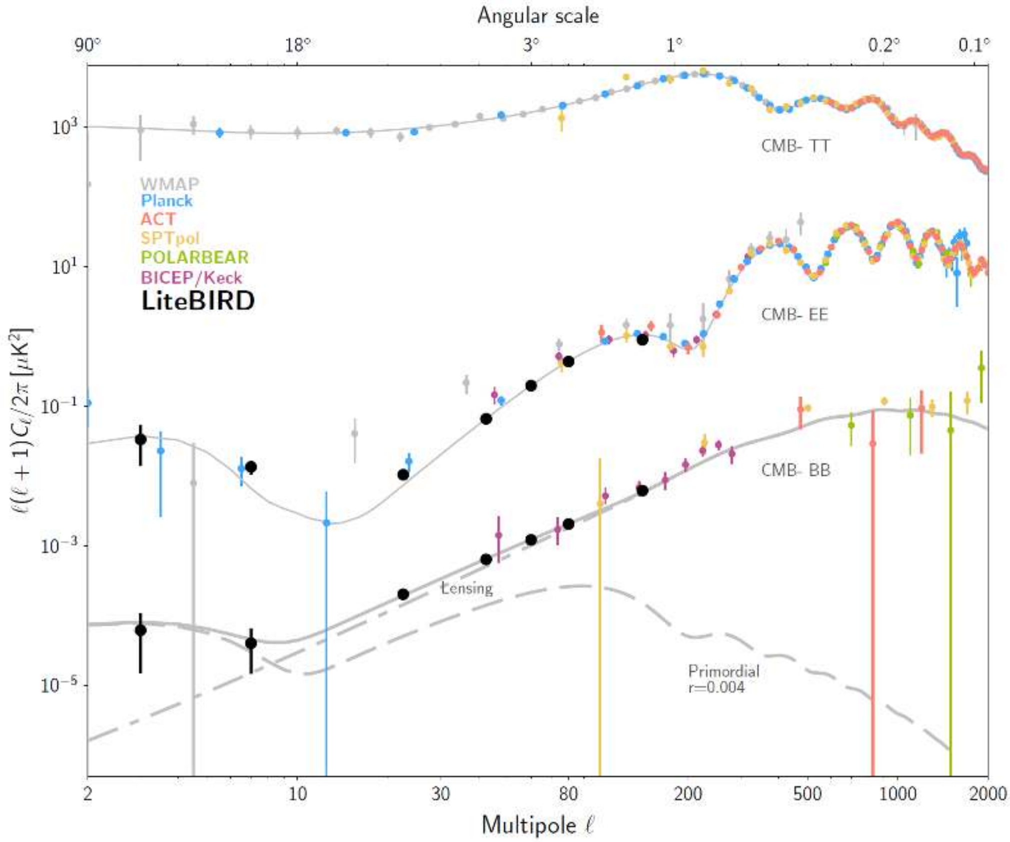

Figure 2.5: The state of the art of the power spectra measurements and the forecast for the future LiteBIRD mission. This image is taken by the LiteBIRD JCAP paper - 2022 (LiteBIRD Collaboration et al. 2022)

2.3 The CMB polarization

The photons of the CMB are partially linear polarized. Their polarization is due to the Thomson scattering with the electrons in a condition of quadrupole anisotropies of the radiation field.

The distribution of the quadrupole anisotropies can be scalar or tensor, accordingly to the physical processes that produced them. The possibility to measure and discriminate the nature of the physical process that produces that unique polarization pattern is one of the more interesting challenges of modern cosmology. The discovery will be transversal within a lot of physical fields. Moreover the interest of modern cosmology, the B-modes detection would also have strong repercussions on other fields of physics like particle physics.

Tensor and primordial gravitational waves perturbations led to the production of a unique pattern of polarization that can not be confused with scalar perturbation on large-scale structures and it can be a smoking gun for inflation theory.

Detecting the CMB polarized signal is a real technological challenge because only 10% of the CMB intensity is polarized. Moreover, the polarization signal deviates from the average by only a few μK. Detecting this very faint signal requires sensitive instruments and fine control of the systematic effects.

Theory

The CMB Polarization anisotropies can be only generated by Thomson scattering and the angular dependency of the outgoing scattered light is given by the differential cross-section

$$\left\langle \frac{dP(t)}{d\Omega} \right\rangle_t = \frac{d\sigma}{d\Omega} \langle |\vec{S}(t)| \rangle_t = \frac{d\sigma}{d\Omega} \propto |\hat{m}' \, \hat{m}|, \tag{2.12}$$

where the $\hat{m}$' represents the polarization versor of the incident radiation and $\hat{m}$ is the polarization versor of the outgoing scattered light. The polarization is represented in the sky by *headless* vector. The vectors are headless because the EM field is invariant under rotations of multiples of π.

To characterize the polarization of the sky, I introduce some useful mathematical structures in flat-sky approximation and Fourier expansion of the anisotropies fields. This approximation works only for small angular scales but can be easily extended using the *generalized* Fourier expansion (in spherical harmonics).

Let us consider radiation characterized by a polarization direction $\hat{m}$ and propagation direction $\hat{m} \cdot \hat{p} = 0$, where $\hat{p}$ being the wavevector of the radiation.

The radiation flux impinging on the surface does not depend on the polarisation direction $\hat{m}$. For this reason, we cannot measure the polarisation of the incident radiation with a simple flux measurement (e.g., the power absorbed by the surface of a detector). However, we must introduce a polarization-dependent description of the EM field.

This description is possible with the Stokes parameters I, Q, U, V that are defined, in the case of radiation propagating along $\hat{z}$ axis, as

$$\begin{aligned} I &= E_x^2 + E_y^2 \\ Q &= E_x^2 - E_y^2 \\ U &= 2E_x E_y \cos(\delta) \\ V &= 2E_x E_y \sin(\delta) \end{aligned} \tag{2.13}$$

Using the Stokes' parameters we can define the *polarization tensor.* In the case of linear polarization, the tensor description is defined

$$\mathbb{I} = \begin{pmatrix} I+Q & U \\ U & I-Q \end{pmatrix}. \tag{2.14}$$

obtaining a 2×2 symmetric matrix. For unpolarized radiation $I_{ij} \propto \delta_{ij}$ because $U = 0$.

The term I is the intensity, Q and U describe the polarization and together with V are well known as *Stokes Parameters.* A graphical representation of the parameters is represented in Fig. 2.6. The parameter V is non-zero only for circular polarization. Since the CMB photons are linear polarized, V can be neglected.

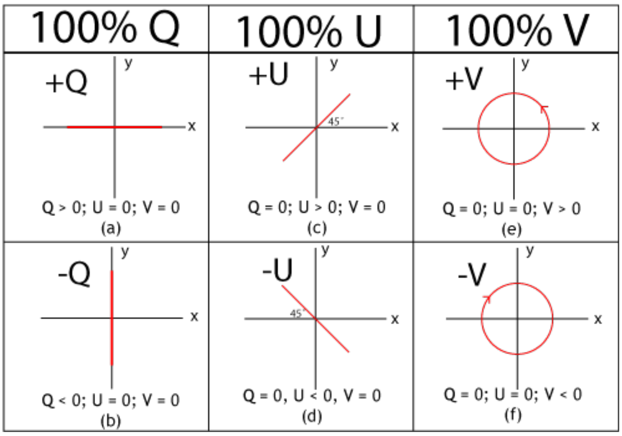

Figure 2.6: Figure (Dan Moulton January 2008)

The polarization tensor can be decomposed into scalar-vector-tensor contribution similarly to what has been done for decomposing the metric tensor

$$I_{ij} = I\delta_{ij} + I^T_{ij} \tag{2.15}$$

where the information needed for the two polarization states is given by the traceless part $I^T_{i,j}$ that can be decomposed in

$$I^T_{i,j} = 2\left(\frac{l_i l_j}{l_2} - \frac{1}{2}\delta_{i,j}\right) E(l) + I^{TT}_{i,j}(l). \tag{2.16}$$

The parameter l is the Fourier vector (we are working in flat-sky approximation) and $I^{TT}_{i,j}$ is the transverse-traceless tensor.

The scalar component E is coupled to the scalar and the tensor part of the metric tensor, while the transverse traceless component is coupled only to the tensor perturbation of the metric.

To show this dependence from the metric, first of all, the scalar and tensor part of the polarization tensor have to be written as a function of Stokes parameters

$$\begin{aligned} E(l) &= \frac{l^i l^j}{l^2} I^T_{ij} = \\ &= Q(l)\left(\cos^2\phi_l - \sin^2\phi_l\right) + U(l)\left(2\sin\phi_l\,\cos\phi_l\right) = \\ &= Q(l)\cos 2\phi_l + U(l)\sin 2\phi_l \end{aligned} \tag{2.17}$$

where ϕ_l is the azimuthal angle of the vector $\vec{l} = (l_x, l_y) = |l|(\cos\phi_l, \sin\phi_l)$[1].

[1] In the flat-sky approximation, a position θ in the sky can be treated as a 2D vector in the x-y plane. The vector $\vec{l}$ is the Fourier counterpart of the of θ and it represents the planar representation of the multipole order l and m in spherical coordinates.

The transverse traceless component of the polarization tensor can be written

$$\begin{aligned} I_{12}^{TT} &= I_{1,2}^{T} - 2\frac{l_1 l_2}{l^2}E(l) \\ &= U(l) - \sin 2\phi_l \left(Q(l)\cos 2\phi_l + U(l)\sin 2\psi_l\right) = \\ &= U(l)(1-\sin^2 2\phi_l) - Q(l)\sin 2\phi_l \cos 2\phi_l = \\ &= B(l)\cos 2\phi_l \end{aligned} \tag{2.18}$$

and thus, using trigonometric idendities we can solve for $B(l)$

$$B(l) = U(l)\cos 2\phi_l - Q(l)\sin 2\phi_l \tag{2.19}$$

The remaining terms of I_{ij}^{TT} can be written in terms of $B(l)$

$$\frac{1}{2}\left(I_{1,1}^{TT} - I_{2,2}^{TT}\right)(l) = -B(l)\sin 2\phi_l \tag{2.20}$$

in order to describe the polarization tensor only as a function of $E(l)$ (the scalar part) and $B(l)$(the tensor part). The final decomposition results as

$$I_{ij}^{T}(l) = E(l)\begin{pmatrix} \cos 2\phi_l & \sin 2\phi_l \\ \sin 2\phi_l & -\cos 2\phi_l \end{pmatrix} + B(l)\begin{pmatrix} -\sin 2\phi_l & \cos 2\phi_l \\ \cos 2\phi_l & \sin 2\phi_l \end{pmatrix} \tag{2.21}$$

The pattern of $E(l)$ and $B(l)$, as a function of the quadrupole intensity is represented in Fig. 2.7.

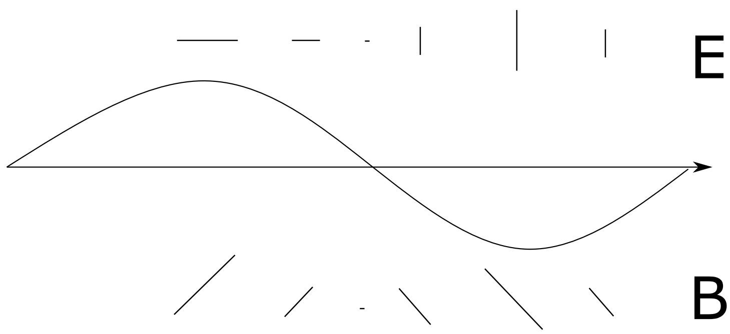

Figure 2.7: E-modes and B-modes representation

Polarization from Compton scattering

The formalism of the polarization tensor can be used to evaluate the features of the polarization signal given by the Compton scattering. Let us consider unpolarized radiation, and let $\hat{z}$ the scattering direction.

Fig. 2.8 and Fig. 2.9 show different scenarios of possible Thomson scattering that could involve photons with the primordial plasma. The first panel of Fig. 2.8 shows Thomson scattering for a plane wave that produces polarized radiation. The case, represented in

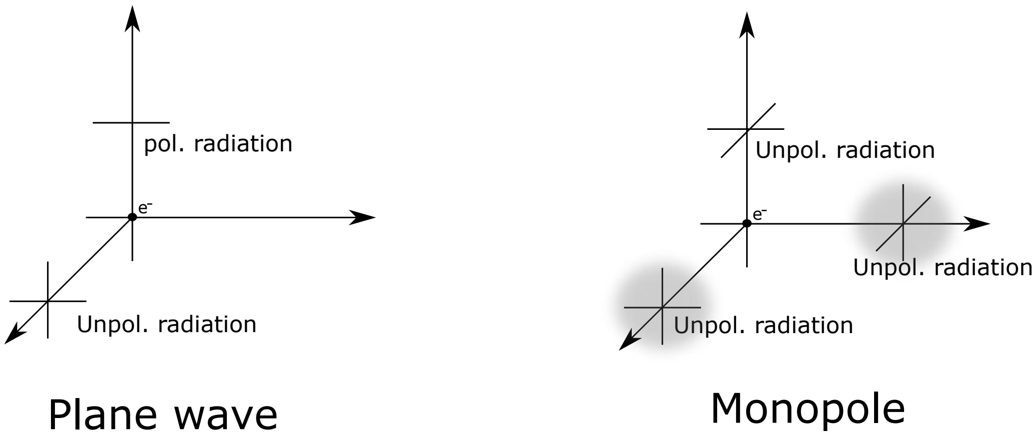

Figure 2.8: Outgoing radiation produced by Thomson scattering in condition of single plane wave and monopole distribution

the right panel is so much frequent and it represents a monopole. The monopole does not produce polarized radiation.

In the same way, the dipole represented in the left panel of Fig. 2.9 does not produce polarized radiation. The scattered radiation is unpolarized and the intensity of the components is the average between the hot and cold components. The only case that produces polarized radiation is represented by a non-zero quadrupole of the radiation represented in the right panel of Fig. 2.9.

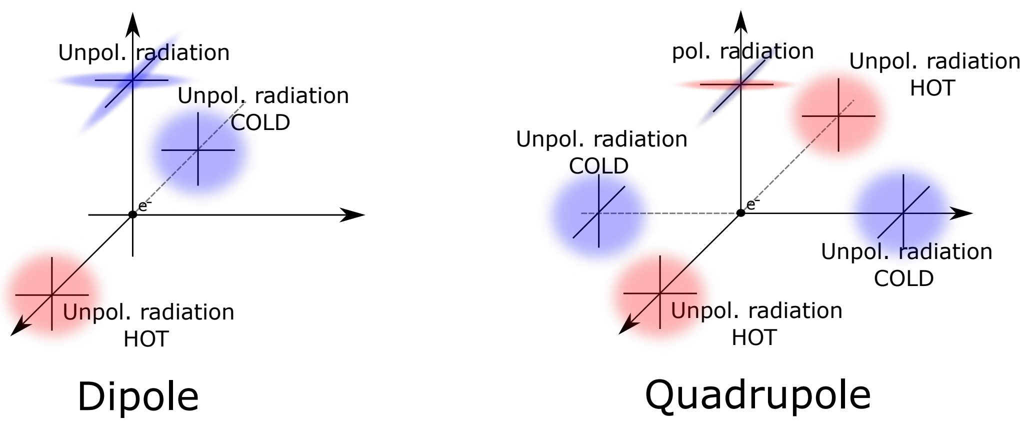

Figure 2.9: Dipole and Quadrupole

For example, the right panel in Fig. 2.9 represents a quadrupole anisotropy and the resulting radiation is characterized by $Q < 0$, $U = 0$ Stokes parameters. If the system would be rotated of $\pi/4$ the scattered radiation had only the U component.

Before the recombination era, electrons and photons were tightly coupled and the radiation field had a small quadrupole moment. For this reason, we expect a polarization signal dimmer than in temperature.

The results depicted in Fig. 2.8 and Fig. 2.9 show the simple case of a plane wave. To generalize these results the system has to be considered as a photon gas and manipulated with the Bose-Einstein statistics (the photons are bosons).

Description of the perturbations in terms of Stokes' parameters

In this section, the Stokes' parameters will be rewritten as a function of perturbation distribution $f(n)$ for a single plane wave in a more general reference. We consider only one constrain on the outgoing scattered radiation, which has to be directed along with the $\hat{z}$ axis.

Let us consider the system shown in Fig. 2.10, the figure represents a generic polarization axes identified by $\hat{n}$ with the two orthogonal axes represented by $\hat{xi}_1'$ and $\hat{\xi}_2'$. The outgoing polarization axes is in $\hat{z}$ direction, and the two orthogonal axes are represented by $\hat{xi}_1$ and $\hat{\xi}_2$ aligned with $\hat{e}_x$ and $\hat{e}_y$, respectively.

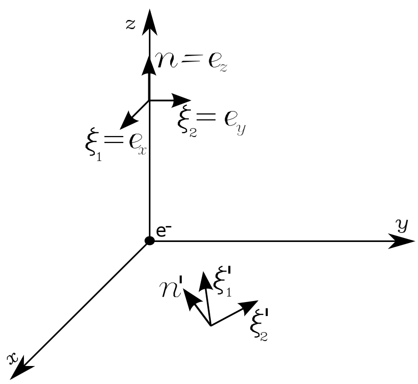

Figure 2.10: Random incident angle

Starting to calculate the Q polarization using its definition. The Q component is sourced by the difference between the contributions for $i = 1$ and $i = 2$ that are $\hat{e}_x$ and $\hat{e}_y$, respectively

$$Q(\hat{e}_z) = A \int d\Omega' f(\hat{n}') \sum_{j=1}^{2} \left(|\hat{e}_x \cdot \xi_j'(\hat{(n)}')|^2 - |\hat{e}_y \cdot \xi_j'(\hat{(n)}')|^2 \right) . \tag{2.22}$$

The coefficient A is a normalization constant. The function f depends only on $\hat{n}'$ and not on j because the incident radiation is unpolarized. To evaluate the dot product between the versor $\hat{e}$ and $\hat{\xi}$ these versors have to be written in Cartesian coordinates

$$\begin{aligned} \hat{n}' &= (\sin\theta' \cos\phi', \sin\theta' \sin\phi', \cos\theta') \\ \xi_2(\theta', \phi') &= (-\sin\phi', \cos\phi', 0) \\ \xi_1(\theta', \phi') &= (\cos\theta' \cos\phi', \cos\theta' \sin\phi', -\sin\theta') . \end{aligned} \tag{2.23}$$

Explicitating the dot products in eq. 2.22 and using trigonometric identites we reach

$$\begin{aligned} Q(\hat{e}_z) &= A \int d\,\Omega' f(\hat{n}) \left[\cos^2\theta' \cos^2\phi' + \sin^2\phi' - \cos^2\theta' \sin^2\phi' - \cos^2\phi'\right] = \\ &= -A \int d\,\Omega' f(\hat{n}') \sin^2\theta' \cos 2\phi' \end{aligned} \tag{2.24}$$

The angular dependence is proportional to $Y_{2,2} + Y_{2,-2}$ and a nonzero Q can be produced only if the incident radiation has a quadrupole moment. The component U of the polarization is given by

$$U(\hat{e}_z) = -A \int d\Omega' f(\hat{n}') \sin^2\theta' \sin 2\phi' \tag{2.25}$$

the angular dependence is proportional to the difference $Y_{2,2} - Y_{2,-2}$ and again only incident radiation with quadrupole moment can produce non-zero U polarization.

Following the integration in Dodelson (2003), substituting $f(\hat{n}')$ with a representation of a perturbation of the photon density we can obtain pure E-modes for scalar perturbations.

In the same way, substituting the tensor perturbation, following Hu & White (1997), we can obtain the polarization pattern for the primordial gravitational waves (B-modes).

2.4 Galactic Foregrounds

Several astrophysical signals emit in the CMB frequencies. These include line emission from galactic CO, free-free emission, Bremßtrahlung radiation produced by free electrons interacting with ions in our galaxy and anomalous microwave emission from spinning dust grains.

The synchrotron and thermal dust emit polarized radiation and introduce a significant spurious polarization contribution in the measurements of the sky dedicated to searching the CMB B-modes polarization.

A brief description of the main polarized sources can be summarized as follow:

Thermal dust

The relevance of thermal dust for B-mode measurements rose after Ade et al. (2014) and the follow-up study made by Ade et al. (2015). In 2014 the BICEP collaboration misinterpreted the foreground signal of the thermal dust as cosmological B-modes. The misinterpretation was resolved by the joint analysis with Planck data in 2015.

The galactic dust is made of grains with sizes ranging from a few nm to several μm. They are heated by ultraviolet and visible light and re-emit in the far-infrared.

However, the tail of their emission law is also relevant to microwaves. The latest constraints from the Planck satellite XII (2020) show that the dust emission law is consistent with a modified black-body with temperature $T_d = 19.6\,\mathrm{K}$. The spectral index is $\beta_d = 1.59$, while the polarised angular power spectrum is consistent with a power-law $C_l \propto l^\alpha$ with $\alpha = -2.45 \pm 0.02$. The dust emission affects the high frequency and, in particular, the power spectrum to large angular scales where the B-modes signal is dominant compared with the lensing contribution.

Synchrotron

At low frequencies, the synchrotron contribution play a significant role in CMB measurements. The synchrotron emission is produced by cosmic-ray electrons spiraling around the galactic magnetic field. The emission spectrum is well described by a power-law ν^{β_s} steeply decreasing, $\beta_s = -3.16 \pm 0.40$ (see Planck Collaboration et al. (2015)). Also, the angular power spectrum follows a power law $C_l \propto l\alpha$, with $\alpha \in [-3.0, -2.6]$, depending on the galactic latitude. This results was presented by La Porta et al. (2008). At high galactic latitudes, the emission is polarised at 10% - 40% level (see Planck Collaboration et al. (2015)) and has to be taken into account for B-mode studies (see Krachmalnicoff et al. (2016)).

Point sources

Some galaxies host an active galactic nucleus, which is thought to be the accretion of a massive black hole. These galaxies have a strong synchrotron emission and are loud in the radio frequencies. These sources can be polarised, typically between 1% and 5%, which makes them a potential foreground for small scales CMB B-mode measurements.

2.5 Component separation in future B-modes measurements

Compared to previous CMB measurements, the detection of primordial B-modes is particularly challenging because the target signal is dominated by the galactic foregrounds. The right panel of Fig. 2.11 shows the spectra emission of the synchrotron, thermal dust and the CMB. Only in a narrow band around 100 GHz the level of the CMB signal reaches the same order as the foregrounds. At lower and higher frequencies the foregrounds largely dominate.

Foregrounds can be distinguished from the CMB signal owing to the different frequency dependence of their spectrum. The process of reconstructing the CMB from a mixture of CMB and foregrounds, measured at multiple frequencies, is called *component separation.*

Until a few years ago the approach of most of the ground-based B-mode experiments was to observe in one frequency band only a region of the sky known to have negligible foreground emission. Recent studies (Krachmalnicoff, Baccigalupi, Aumont, Bersanelli, & Mennella 2016) have demonstrated that no sky area can be safely considered foreground-free, especially if the large scales are to be probed. All the CMB experiments are upgrading their hardware, in order to have the multi-frequency coverage needed for component separation.

In the design of forthcoming experiments, it is crucial to assess how a given configuration will perform in terms of component separation. Errard et al. (2011) developed an efficient framework for accomplishing this task, enabling the quick exploration of large sets of experimental configurations.

Such techniques have been heavily used in designing and optimizing the future installments of the Polarbear observatories, including PolarbearII and Simons Array.

A key assumption in this method is that the sky model adopted in the component separation process matches the actual sky emission (*Stompor et al. - 2016* Stompor et al.

(2016)).

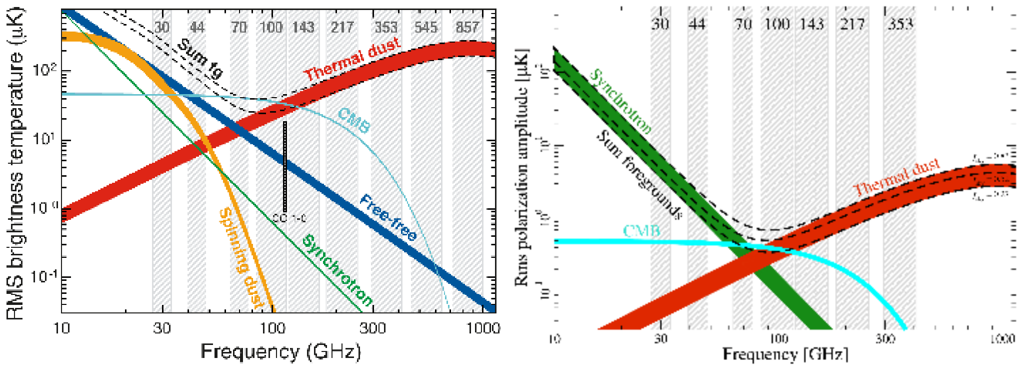

Figure 2.11: Intensity (left) and polarised (right) spectrum of the CMB and the galactic foregrounds. Figure credits: *Planck*

2.6 Future experiment devoted to the CMB B-modes polarization

The density perturbations of the primordial plasma result in only *E-modes* polarization that had been discovered by DASI and characterized by Kovac *et al.*(Kovac et al. 2002). Nowadays, the CMB community has moved his scientific interest to the detection of the *B-modes* signal, which originates by *Primordial inflationary Gravitational Waves*(Guth 1981) - PGW, and by the weak lensing of the foregrounds large scale structures.

The PGW B-modes have never been observed yet, but measurements on lensing *B*-modes, performed by SPT(Wu et al. 2019), and recently by BICEP3(Collaboration et al. 2021), set an upper limit to the tensor to scalar ratio $r_{0.05} = 0.014 \pm 0.010$ ($r < 0.036$ at 95% C.L.).

In this context a synergistic approach between different experiment philosophies is fundamental. Space satellite-like WMAP[2], PLANCK[3], and the future LiteBIRD(Sekimoto et al. 2020; Montier et al. 2020; Hazumi et al. 2020) are essential to cover all the 4π sky in order to detect the very low-l PGW B-modes bump on the power spectrum. Similarly, a new generation of ground-based telescopes like CMB-S4(Abazajian et al. 2016), Simon Observatory(Ali et al. 2020), CLASS(Watts et al. 2018), QUIJOTE(Rubiño-Martín et al. 2010), GroundBIRD(Oguri et al. 2016) and LSPE(The LSPE collaboration et al. 2020) are devoted to observe large part of the sky from different geographical sites in order to cover as much as possibile the fraction of sky-map and characterized the polarized foreground at large angular-scales.

This information combined with the previous stage of CMB experiments devoted to observing small patches of the sky like BICEP2/Keck(Ade et al. 2016), POLARBEAR(P. A. R. Ade et al. 2014), ACT(Kosowsky 2003), SPT(Wu et al. 2019), QUIET(Samtleben

[2] http://map.gsfc.nasa.gov/

[3] http://www.esa.int/Science_Exploration/Space_Science/Planck

2008) will play a crucial role in constraining the gravitational lensing potential at small and medium angular-scales, and in characterizing different aspects of the millimetric and submillimetric sky.

The challenge of the atmosphere

The ground-based CMB experiments have to deal with atmospheric emissions. It led to an extra optical load on the detectors, increasing the total white noise. Moreover, the water vapor in the atmosphere is hardly concentrated, and it introduces correlated noise on the single detector and cross-correlation between the focal plane. This kind of noise affects the large angular scales structures of the reconstructed maps degrading the angular power spectrum estimation for low-l. Today, the problem of the atmospheric spurious correlation and cross-correlation remains an open problem. It is very complicated to attain general rules because the atmospheric contribution depends on the geographical sites, instrumental properties, scanning strategies, day/night fluctuations, seasonal fluctuations, and many other variables (instrumentals and environmental) that are very difficult to take under control.

For this reason, the new class of ground-based telescopes dedicated to observing the polarization of CMB will adopt new hardware and data analysis solutions to reduce the spurious contribution from the atmosphere.

The LSPE/Strip experiment will use coherent radiometer technology to directly measure the Q and U Stokes' parameters from the sky. In this way, the non-polarized contributions are mitigated like the atmospheric emission that is mostly unpolarized. The instrumental leakage from total intensity I to polarized channel P represents the dominant contribution of the atmospheric emission.

Chapter 3

The Large Scale Polarization Explorer (LSPE)

The *Large Scale Polarization Explorer* - LSPE - is an international experiment with Italian leadership designed to measure the polarization of the CMB at large angular scales.

The experiment is composed by two instruments. Strip is the low-frequency instrument and it is sensitive at 43 GHz and 95 GHz. Strip will observe the sky from the ground and will be located at Teide Observatory. SWIPE is the high-frequency instrument sensitive at the frequencies 140 GHz, 210 GHz and 240 GHz. SWIPE is conceived as a balloon and will observe the sky from the stratosphere.

The primary goal of the LSPE experiments is to measure the CMB polarization *B-modes* and constrain the tensor-to-scalar ratio to $r \leq 0.01$, at 68% of confidence level.

LSPE will also measure the Galactic polarized foregrounds, in particular, synchrotron and thermal dust emissions. The synchrotron emission is due to charged particles, mostly electrons, that move at a relativistic velocity within the galactic (Milky-Way) magnetic field.

Another accessible goal of the mission includes point-sources characterization like Tau-A, Cas-A, and Cyg-A. The point-sources characterization represents a possible transferable knowledge to other balloons/satellite experiments for beam shape reconstruction and polarization angle calibration (e.g. LiteBIRD and CMB-S4).

Moreover, another important target of the LSPE experiment concerns the study and characterization of the sky quality at Observatorio del Teide (Tenerife) for CMB polarization measurements. This last target of the experiments does not concern cosmology, but anyway it plays a key role in mitigating the atmospheric spurious contribution in the CMB polarization measurements and to promote this site as a possible solution for the future CMB polarization experiments.

3.1 Strip and SWIPE instruments

The two different instruments of LSPE (SWIPE and Strip) will permit to observe about the 25% of the Northern sky hemisphere.

The observation strategies of the two instruments is shown in Fig. 3.1. The green area represents the sky overlap between the two observed sky areas which is the 85% of the sky observed by each instrument. The blue dashed line represents the SWIPE scanning strategy, while the red dashed line represents the Strip scanning strategy.

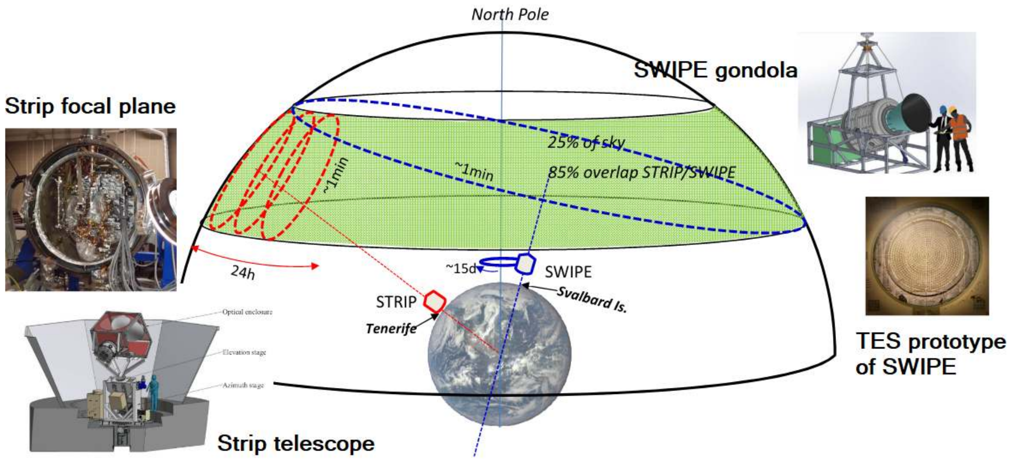

Figure 3.1: The green sky fraction represents the part of the sky observed by both the instruments Strip and SWIPE. The inserts on the left side represent a picture of the Strip focal plane and a 3D-view of the telescope. On the right side, we see the SWIPE instrument mounted on the gondola, and a spider-web TES prototype produced in Genova by INFN. Image from LSPE The LSPE collaboration et al. (2020)

Table 3.1 describes the main performance of the experiment in terms of frequency, bandwidth, angular resolution and expected noise as well as the expected duty cycle, sky coverage and mission duration.

Table 3.1: Summary of the LSPE forecast performance

Instrument	Strip	SWIPE
Site	Tenerife	Balloon (North Pole)
Freq (GHz)	43, 95	140, 210, 240
Bandwidth	16%, 8%	**30%**
Angular resolution FWHM (arcmin)	20, 10	85
Detectors technology	HEMT	TES multimoded
Number of detectors N_{det}	49, 6	162, 82, 82
Detector noise		
equivalent temperature ($\mu K_{\mathrm{CMB}} \cdot \sqrt{s}$)	593, 1347	12.7, 15.7, 30.9
Mission duration	2 years	$\sim$ 15 days
Duty cycle	50%	90%
Sky coverage f_{sky}	37%	38%

3.2 The LSPE/SWIPE Instrument

SWIPE is a stratospheric balloon that will measure the microwave sky at 145 GHz, 210 GHz and 240 GHz during a long-duration flight around the North Pole currently scheduled for winter season. We are currently considering two possible options for the flight, both shown in Figure 3.2.

In the first scenario, the balloon will be launched from Kiruna, a small village in the northern part of Sweden. In the second scenario (our current baseline), the balloon will be launched from the Svalbard islands. This is the best solution because, during the whole flight, the payload will always be in the Earth's shadow. Kiruna, on the other hand, is more favorable from the point of view of the launch logistics.

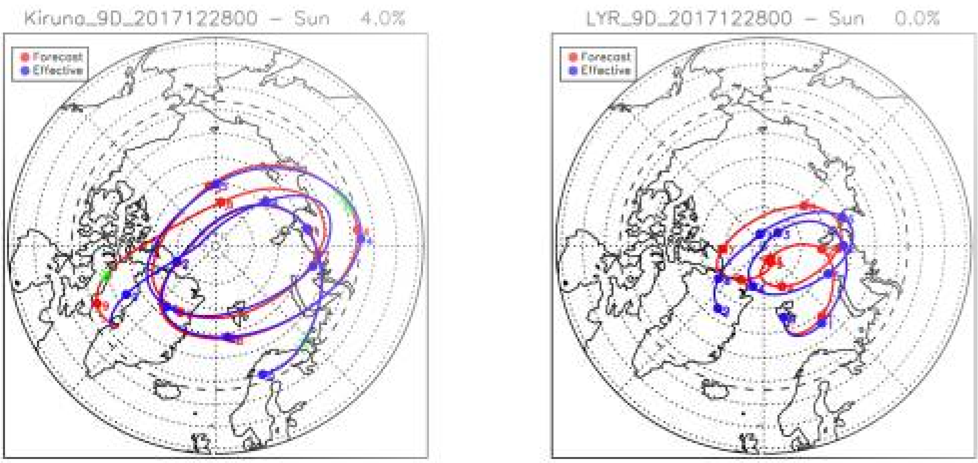

Figure 3.2: *Left panel:* shows the forecasted SWIPE orbit in the case of his launch from Kiruna. The blue and red orbits represent two different forecasts using the median and the average, respectively. *Right panel*: shows the same information as the left ones in the case of the launch from Svalbard islands.

A cutaway of the SWIPE instrument is shown in Fig. 3.3. The main part is represented by the cryostat. It is designed to be hooked to a gondola module that ensures the azimuth pointing of the instrument. The two focal planes are populated with 326 TES detectors that work on three different frequency ranges. The low-frequency channel is centered at 140 GHz (with 30% of bandwidth). In addition, there are two ancillary channels with central frequencies centered at 210 GHz and 240 GHz.

Despite the low number of detectors, SWIPE can reach excellent sensitivity using multi-modal horns. The IR filters mitigate the total load on the detectors, and a polarization modulator, based on a rotating half-wave plate, is used to modulate the polarization of the scientific signal (the CMB polarized photons). The low-frequency correlated noise is separated in the frequency domain during the post-processing analysis.

The multi-mode design permits them to shine homogeneously on the detectors as

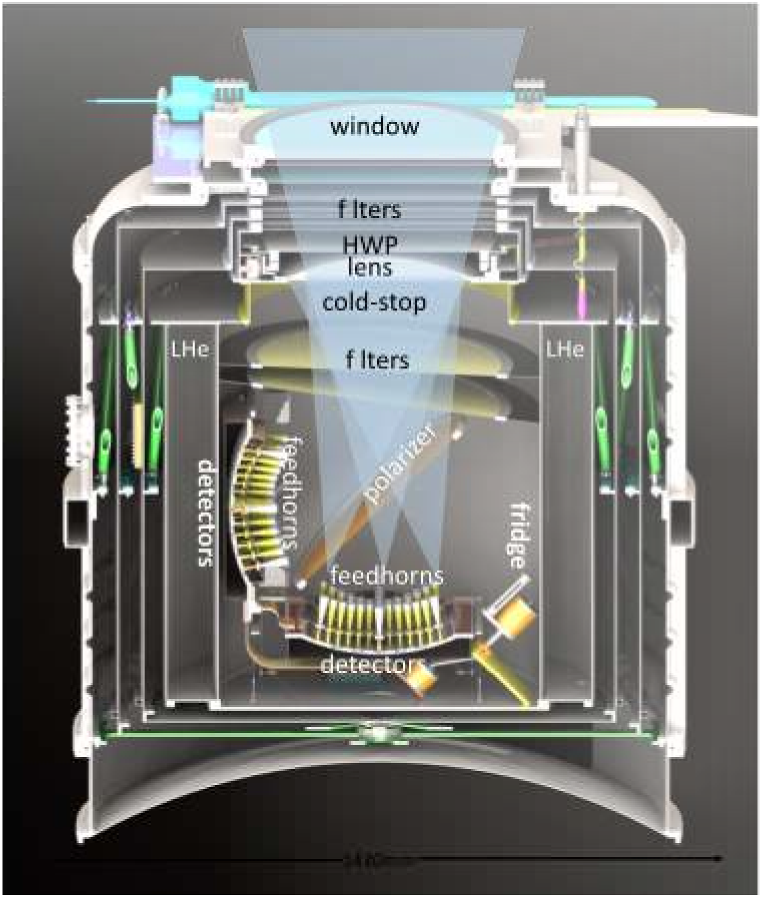

Figure 3.3: Cutaway of the 3D model of the LSPE/SWIPE Instrument cryostat. The optical components are cooled down to $\sim 15\,\mathrm{K}$ and the detectors to $\sim 300\,\mathrm{mK}$. Image from LSPE The LSPE collaboration et al. (2020)

shown in Fig. 3.4 that displays the simulated radiation pattern for the feed-horn beam (top panel) and the electromagnetic response of the telescope illuminated with the multi-modal horn (bottom panel).

Differently from the single-mode, the multi-modal feed-horns are characterized by a flat-top response that distributes the photon homogeneously on the detector surface. The number of photons acquired grows accordingly with the ratio $S_{\mathrm{ill}}/S_{\mathrm{tot}}$ where S_{tot} is the physical surface of the detector, and S_{ill} represents the detector area illuminated by the radiation.

3.2.1 Instrument description

As described in the previous section, SWIPE presents interesting solutions to overcome the correlated low-frequency noise and improve sensitivity. The rotating HWP allows us

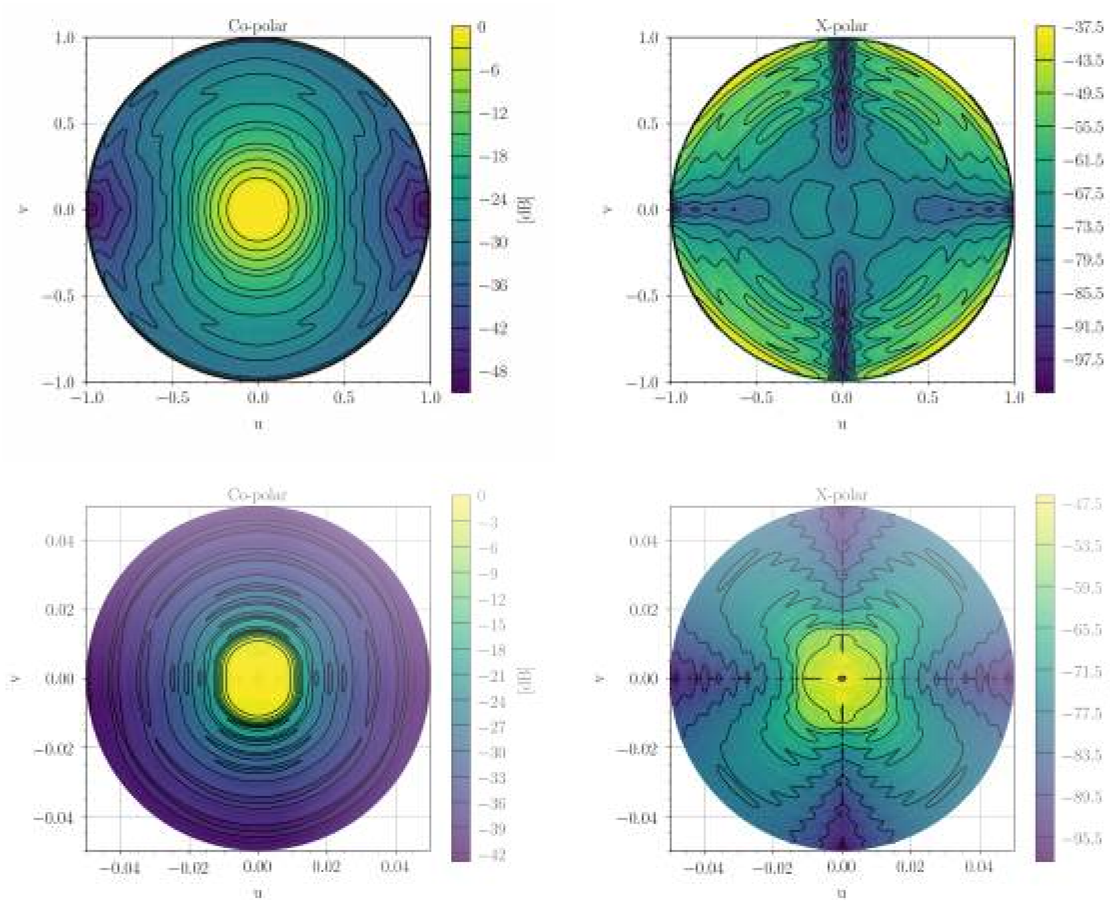

Figure 3.4: *Top panel:* multi-modal feed-horn simulation. *Bottom panel:* the optical response of the SWIPE telescope.

significant mitigation of the spurious correlations and the multimode feedhorns allow us to increase the signal-to-noise ratio.

Now, I describe more in detail the main parts of the instrument:e

- **Cryostat:** the cryostat has a volume of 250 liters and it contains super-fluid helium. It is realized in aluminium to ensure the weight constrain as developed for the cryostats used in OLIMPO (Presta et al. 2020), PILOT (Mangilli et al. 2018), BOOMERanG (Lange et al. 1995), and ARGO (De Bernardis et al. 1993). Two vapor-cooled intermediate shields, separated by super-insulation blankets, are used to minimize the radiative heat load on the LHe bath. The main cryostat provides the base temperature to cool down the polarization modulator and the optical system, and to operate a double stage ^{3}He evaporator (Coppi et al. 2016). The latter cools down to 0.3 K the detector arrays. The hold time forecast for the LHe in the main cryostat is $\sim$ 20 days, while the ^{3}He refrigerator has a hold time of $\sim$ 7 days, and can be recycled in flight. The main front window is designed to accommodate a series of IR-filter to minimize the heat load on the detectors. The design of the window and filters is similar as developed for the EBEX (Zilic et al. 2017) experiment.

- **Polarization modulator:** A rotating *Half Wave Plate* - HWP modulates the polarized signal with a fixed frequency f_{HWP}. The HWP operates by rotating the plane of linearly polarized light by twice the angle (because the polarization vector is headless) between the retarder's fast axis and the input plane of polarization. In this way, the signal produced by the modulator is the convolution between a low-frequency fluctuating signal (the spurious non-polarized components) and a high-frequency signal produced by the rotation of the polarization angle of the only polarized signal acquired by the telescope. The result is a Fourier representation of the signal where the low-frequency and the high-frequency contribution are well separated in frequency. The low-frequency part, which contains all the unpolarized signals, can be easily eliminated with a frequency filter with minimal loss of scientific information. The SWIPE Half-Wave Plate is made of metal mesh material developed by Pisano et al. (2015b) in Cardiff. This technology consists of anisotropic metal grids, stacked together and embedded into polypropylene, which mimic the behavior of a birefringent plate (Pisano et al. 2012, 2015a). In order to ensure a continuous rotation of the HWP with enough speed ($\sim$ Hz) the system floats and rotates due to a superconducting magnetic bearing designed by Matsumura et al. (2016). The electromagnetic actuators for keeping the rotator in a precise position were developed by Columbro et al. (2018) and it is composed of a set of frictionless clamp/release devices.

- **Multi-mode horns:** The radiation is coupled to the detectors using smooth conical horns feeding multi-moded waveguides (Legg et al. 2016). Waveguides act as filters, selecting a frequency-dependent number of modes, thus determining the effective pixel throughput. The contributions from the individual modes have been evenly weighted. SWIPE uses a full-field polarizer to split polarization into two independent focal planes, for this reason, the polarization properties of the individual pixel assembly are negligible for the end-to-end performance evaluation. Therefore, no concern arises due to the co-polar and cross-polar response behavior of the horns. In order to simplify the design and production cycle of the horns, no additional optimization was performed at the pixel level. Instead, further suppression of power at large angles from the sky is performed by heavily over-illuminating the cold aperture stop. The multi-moded beam of each horn thus ensures a very uniform illumination pattern of the telescope optical system maximizing the aperture efficiency. The unwanted power pickups in the horn sidelobes are mitigated by cold, stable, highly absorptive surfaces assembled inside the telescope tube. Additional large-angle pickups due to strong beam truncation at the aperture will be mitigated through an absorptive external baffle. The multi-moded approach ensures a homogeneous illumination of the detectors and increases the effective area of the telescope, but these features come at the price of a lower angular resolution of the receiver. It is acceptable since the main scientific target of SWIPE is polarization detection at large angular scales.

- **Detectors:** The focal plane of LSPE/SWIPE uses Transition-Edge Sensors (TES) detectors, custom-designed for an adequate coupling between the radiative power propagated by the multi-modes feedhorns. They are made in Si with Au absorber deposited on a central free-standing Si_3N_4 membrane. The collecting area of $15{\times}15\,\mathrm{mm}^2$ is designed to optimize the coupling with the propagating modes ad effectively reject cosmic rays. The sensors are located aside from the spiderweb and are in contact with the gold absorber. Each TES is made in $\mathrm{Au-Ti}$ bilayer and the critical temperature from normal to superconducting phase is around $T_c = 500\,\mathrm{mK}$. The absorption requirement can be reached by the spiderweb design of the detectors that ensures a wide sensitive area homogeneously illuminated by the feedhorns' waveguides. The waveguides are characterized by a custom design similar to a cavity to sum all the modes and shine homogeneously the detectors.

- **Electronics:** the 326 TES are read-out by *Superconducting Quantum Interference Devices* - SQUIDs - using a *Frequency-Domain Multiplexing* - FDM - scheme, in which each sensor represents a RLC circuit with a proper resonant frequency. Each DC-SQUID is sensing 16 TES (Vaccaro et al. 2019). In the FDM scheme, a group of detectors is read with a single SQUID by connecting in parallel several RLC chains in which R is given by the TES variable resistance, and the LC filters define different frequencies. A single signal containing all the different frequencies is therefore needed to bias all TES simultaneously. The readout electronic chain is composed of a "cold" section inside the cryostat, at the same temperature as the detector arrays, and a "warm" section, outside the cryostat. SQUID boxes each LC board is connected with a custom low-inductance flat cable to a SQUID box placed at 1.6 K. Each box is used to thermalize and shield three SQUIDs used for the readout of the TES signals.

3.3 The LSPE/Strip instrument

The LSPE/Strip is a coherent polarimeter array designed to observe the microwave sky at 43 GHz and 95 GHz from Izana - Tenerife. The telescope is based on a dual-reflector crossed Dragone design: providing low aberrations, cross-polarization, and high symmetry over a wide focal plane. Strip has a parabolic primary mirror with an aperture of 1.5 m, and a hyperbolic secondary mirror, providing an angular resolution of $\sim$ 20' in the Q-band (43 GHz) and $\sim$ 10' in the W-band (95 GHz).

The focal plane is composed of 49 polarimeters sensitive in the Q-band with a central frequency of 43 GHz. In addition, the focal plane is also provided with 6 polarimeters sensitive in the W-band, with a central frequency of 95 GHz. The first channel is dedicated to acquiring scientific data, while the W-band channel is reserved for atmospheric monitoring.

The Strip polarimeters use coherent technology exploiting low noise, High Electron Mobility Transistor (HEMT) amplifiers, and high-performance wave-guide components. The instrument is cooled to 20 K by a two-stage Gifford-McMahon cooling system.

The coherent technology permits excellent mitigation of the $1/f$ noise due to gain fluctuations, and temperature-to-polarization leakage, without the need to introduce extra optical elements to modulate the polarized signal.

3.3.1 The Site

The Strip telescope will be deployed at the Teide Observatory in Tenerife, 2390 m above sea level. The median precipitable water vapor is 3.5 mm, reaching values below 2 mm during the dryest months.

Figure 3.5 shows the observing site area with the Strip platform. The Strip experiment will complement two other CMB experiments observing from Tenerife: QUIJOTE (10-40 GHz) (Rubiño-Martín et al. 2010) and GroundBIRD (145-225 GHz) (Tajima et al. 2012). All three experiments (QUIJOTE, LSPE-Strip, and GroundBIRD) will measure approximately the same area in the northern sky at degree scales, opening the possibility of future joint analyses. The Strip measurements are scheduled to start between 2024 and 2024, and the telescope will continue to acquire measurements for at least two years.

3.3.2 The telescope: optics and mount

The Strip telescope consists of two reflectors, a parabolic primary mirror and a hyperbolic secondary mirror, arranged in a Dragonian cross-fed design, originally developed for the CLOVER (Taylor et al. 2004) experiment.

The main requirements for the optics are cross-polar discrimination better than -30 dB and a level of side-lobes rejection of -55 dB and -65 dB for near and far side-lobes, respectively. The detectors-array is placed in the focal region, ensuring no obstruction of the field of view.

The telescope will be surrounded by a co-moving baffle made of aluminum plates lined with a millimeter-wave absorber, to reduce the ground peaks-up contamination.

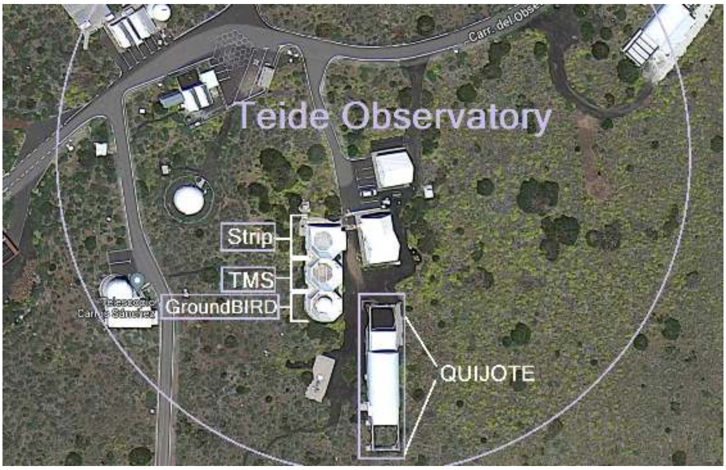

Figure 3.5: Overview of the Strip observing site at the "Observatorio del Teide". Strip will be located on the North platform. The central platform will be dedicated to the *Tenerife Microwave Spectrometer* (TMS) and the South platform is used by GroundBIRD. Few meters eastward we find the QUIJOTE Observatory.

The optical design had been studied by S. Realini in her Ph.D. thesis. The simulated electromagnetic response of the telescope and the details of the optical model can be found in Realini et al. (2022).

The mechanical structure is composed of an Alt-Az mount. The structure was initially developed for the CLOVER (Taylor et al. 2004) telescope. The design was then modified for Strip and a complete structural analysis was performed to certify the mechanical stability of the structure. As of today, we are in the process of manufacturing the missing parts to proceed to the final integration and testing of the whole telescope.

The power and the data are connected to the telescope using a rotary joint and allowing the telescope to rotate continuously and scan the sky as a spinner. The data from a star camera and a tiltmeter, placed on the optical assembly structure, combined with the motor encoder's data allow us to reconstruct the pointing taking also into account the thermo-mechanical structure deformations.

3.3.3 Focal plane

The left panel of Fig. 3.7 shows a schematic of the Strip cryostat. The Strip focal plane array of corrugated feed horns is placed inside the dewar surrounded by a radiative shield cooled to 80 K by the cooler first stage. Copper thermal straps connect the focal plane and the cooler cold head allowing the polarimeters' chain to be cooled down to 20 K. The cryostat aperture is an *Ultra-High Molecular Weight Polyethylene* - UHMWP - window followed by IR filters to reduce the radiative load from the 300 K environment.

The detector assembly is based on coherent polarimeters connected to an optical chain constituted of corrugated feedhorns, each coupled to a *Polarizer-OrthoMode Transducer* - OMT - system at 43 GHz and to a septum polarizer at 95 GHz (Peverini et al. 2021).

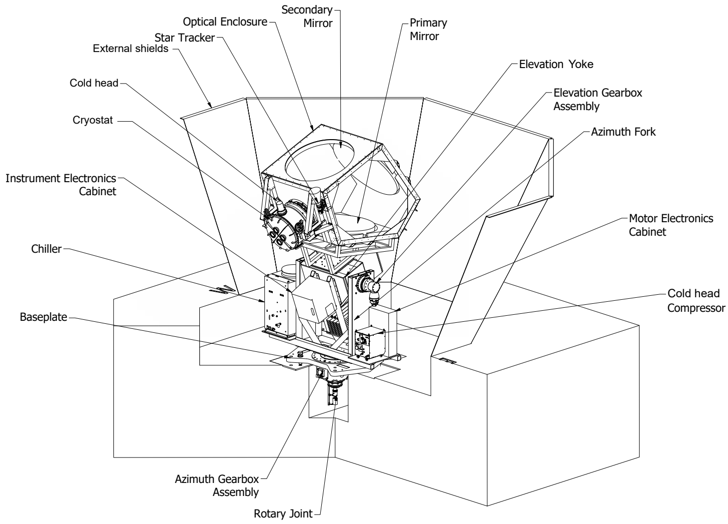

Figure 3.6: 3-D model of the Strip telescope placed in its basement and surrounded by ground shields.

The right panel of Fig. 3.7 shows the focal plane of corrugated feedhorn arrays: 49 Q-band antennas, arranged in modules of 7 units each, and 6 W-band antennas, located along the focal plane perimeter. Each feedhorn is connected to a polarizer-OMT assembly that converts linear into left- and right-circular polarization, and then to a coherent polarimeter that detects directly the Q and U Stokes parameters (The LSPE collaboration et al. 2020).

The W-band polarimeters are the best 6 (in terms of $T_{\rm noise}$) used by QUIET. The Q-band array uses a combination of 18 QUIET modules and 31 additional units specifically developed accordingly to the same design.

3.3.4 The Electronic Readout

The acquisition system is composed of seven twin boards. Each unit controls eight polarimeters, providing the biasing currents (48 HEMT LNAs, 16 phase-shifters and 32 GaAs detectors) and handling the data acquisition. As described in The LSPE collaboration et al. (2020), the bias voltages can be set and monitored by the bias boards. The phase switches are synchronized by the master-clock signal generated by the onboard GPS + Master Clock boards (produce a pulse per seconds reference).

The DAQ boards serve as telescope command interpreters and for acquiring scientific data generated by the 4 detectors of each polarimeter. Each board acquires 32 signals (8 polarimeters $\times$ 4 diodes per polarimeter) at the sample rate of 1 MHz, demodulates the scientific data at the fast phase switch rate of 4 KHz, prepares the scientific packets with housekeeping data and time tags obtained by the GPS+master-clock system. Finally, the packets are sent to the main computer using a copper-ethernet connection and stored on the local disk.

A *Field Programmable Gate Array* - FPGA - on the DAQ board is devoted to pro-

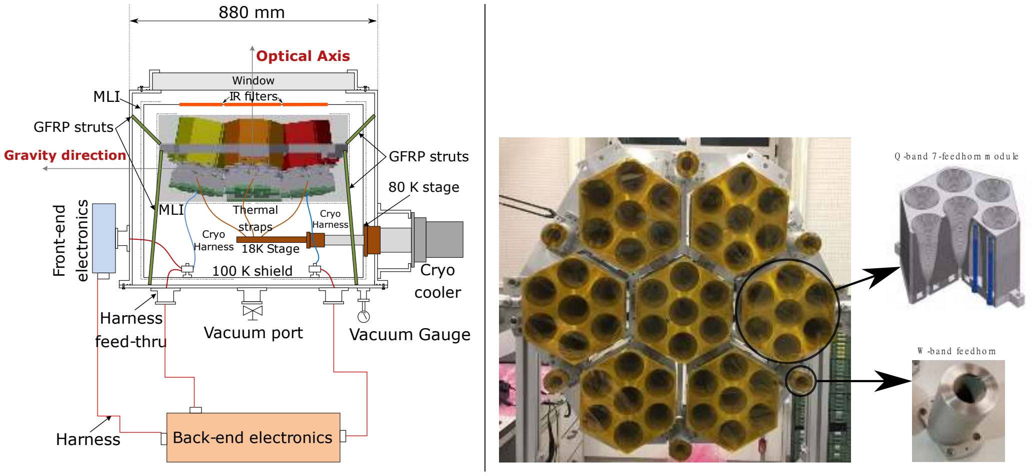

Figure 3.7: *Left Panel:* schematic representation of the Strip instrument. The focal-plane is connected to the cooler cold-head (at 18 K) by means of thermal straps. *Right panel:* optical front-end of the focal plane composed by 49 corrugated feedhorns working at 43 GHz and 6 corrugated feedhorns at 95 GHz.

cessing the mathematical operations for the demodulation as well as the *digital-to-analog* - DAC - and *analog-to-digital* - ADC conversions. A microcontroller handles the communication with the main computer, decodes and routes the commands towards the FPGA and assembles the data packets.

3.3.5 Design of the Polarimeter Modules

The Q-band and the W-band channels of LSPE/Strip instrument are based on coherent polarimeters. Eighteen polarimeters of the Q-band and six polarimeters of the W-band are the same polarimeters that were mounted on the QUIET focal plane. The other thirty-one polarimeters of the Q-band were built following the QUIET polarimeters design (Cleary 2010).

They are based on cryogenic *High Electron Mobility Transistors* - HEMT - low noise amplifier (LNA) with coherent technique, following the tradition of polarization-sensitive experiments such as CBI(Padin et al. 2001), PIQUE and CAPMAP(Barkats et al. 2005), COMPASS(Farese et al. 2004), WMAP(Kogut et al. 2003), and Planck-LFI(Bersanelli & Mandolesi 2000).

Unlike those experiments, however, QUIET and Strip use a miniaturized design suitable for large arrays (Lawrence et al. 2004). The waveguides are replaced with a *Monolitic Microwave Integrated Circuit* - MMIC - device.

In Figure 3.8 we show a picture of a Q-band QUIET polarimeter that highlights the various components in the chain. Fig. 3.9 shows a schematic view of the pseudo-correlation design of the Strip polarimeters, that allows one to detect directly the Stokes parameters Q and U from the left- and right-circularly polarized inputs provided by the

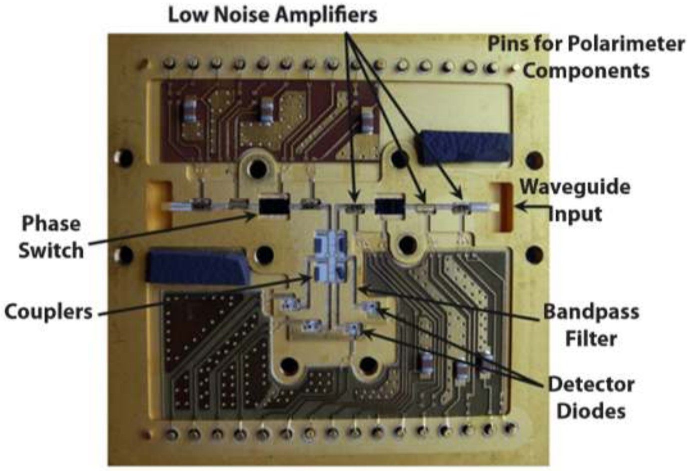

Figure 3.8: Q-band QUIET polarimeter with the various components identified and labelled. The size of the device is 5cm×5cm

polarizer-OMT assembly. For the W-band, the polarization of the radiation is separated and converted into circular polarization by septum-polarizers. In the case of the Q-band, the same process is performed by a polarizer - OMT septum (Peverini et al. 2021).

Following Fig. 3.8, I describe each component of the polarimeter module and give its Jones matrix. This will allow us to compute how the signal is acquired and processed by the polarimeter module.

- **Low Noise Amplifiers - LNAs:** The whole chain is characterized by three HEMT transistors in series (the W-band LNAs have four HEMTS each). All three HEMTs in the LNA have a common drain and gate voltage. Each leg has three LNAs, together they combine to give gain g_{A} on leg A, and g_{B} on leg B. The Jones Matrix for the amplifiers is given by:

$$S^{\mathrm{amp}} = \begin{pmatrix} g_{\mathrm{A}} & 0 \\ 0 & g_{\mathrm{B}} \end{pmatrix}. \tag{3.1}$$

The input and output states have basis vectors (E_{A} ,E_{B}), where A and B refer to the module legs. The noise in the module is dominated by the noise from the LNAs, and it comes primarily from thermal noise. To reduce thermal noise, the module is cryogenically cooled to a stable temperature of $\sim 20\,\mathrm{K}$. Moreover, the LNA noise scales with the bandwidth, which in practice scales with the frequency of interest. As a result, LNAs operating at higher frequencies will have higher noise. The lower limit for noise in an LNA is fundamentally set by quantum mechanics: the noise cannot be lower than the quantized energy of a photon at the detector frequency, which will have an associated temperature given by:

$$kT_q = h\nu \to T_q = \frac{h\nu}{k} \tag{3.2}$$

where h is Planck's constant, ν is frequency, and k is Boltzmann's constant. At 43 GHz, this is 1.9 K, and at 95 GHz this is 4.3 K. The best performing Q-band module operates at $\simeq$ 11.5 times the quantum limit, and the best performing W-band module is operating at $\simeq$ 14 times the quantum limit.

- **Phase Switches:** Each polarimeter module has two phase-switch circuits, one on each leg of the module. A single-phase switch operates by sending the signal down one of two paths within the phase switch circuit. One path has an added length of $\lambda/2$ to give the signal a phase of 180° compared to the other segment. Two Indium-Phosphide MMIC PIN (p-doped, intrinsic-semiconductor, n-doped) diodes control which path the signal will take. When forward biased, the diode allows the current to flow; when reverse biased, it stops current flow. With only one of the two diodes biased, the signal will be sent down whichever path has the forward-biased diode. When neither or both PIN diodes are biased, the signal cancels. PIN diodes are capable of fast switching, and they can switch between the two different phase states at a rate of 4 kHz. The Jones matrix for the phase switch is given by:

$$S^{\mathrm{PS}} = \begin{pmatrix} e^{i\phi_{\mathrm{A}}} & 0 \\ 0 & e^{i\phi_{\mathrm{B}}} \end{pmatrix} \quad (\phi_{\mathrm{A}}, \phi_{\mathrm{B}}) \in \{0,\, 2\pi\} \tag{3.3}$$

- **Phase Discriminator:** The phase discriminator consists of two hybrid couplers, each of which is composed of Schiffman phase delay lines (Pozar 2011) and broad-band branch line stripline couplers. The first part is composed of a π coupler that is represented by the Jones matrix:

$$S^{\pi} = \frac{1}{\sqrt{2}} \begin{pmatrix} 1 & 1 \\ 1 & \text{-1} \end{pmatrix} \tag{3.4}$$

The outputs of the π coupler propagate through a pair of power splitters. One of the outputs of each splitter is sent to the detectors and the second part is sent through a phase-delay. The power-splitter is represented by

$$S^{\mathrm{PowSplit}} = \frac{1}{\sqrt{2}} \begin{pmatrix} 1 & 0 \\ 0 & 1 \end{pmatrix} \tag{3.5}$$

and the $\pi/2$ phase-delay and coupler is represented by

$$S^{\pi/2} = \frac{1}{\sqrt{2}} \begin{pmatrix} 1 & \mathrm{i} \\ \mathrm{i} & 1 \end{pmatrix} \tag{3.6}$$

After the second phase delay, the second part of the signal is read out by the second pair of detectors.

In the previous list, I presented all the main parts of a polarimeter. Now, I present the signal acquired by the detectors. Let's start to consider the Q signals

$$\begin{pmatrix} E_{Q_1} \\ E_{Q_2} \end{pmatrix} = S^{\mathrm{PowSplit}} S^{\pi} S^{\mathrm{amp}} S^{\mathrm{PS}} \begin{pmatrix} E_{\mathrm{A}} \\ E_{\mathrm{B}} \end{pmatrix}^{\mathrm{in}} \tag{3.7}$$

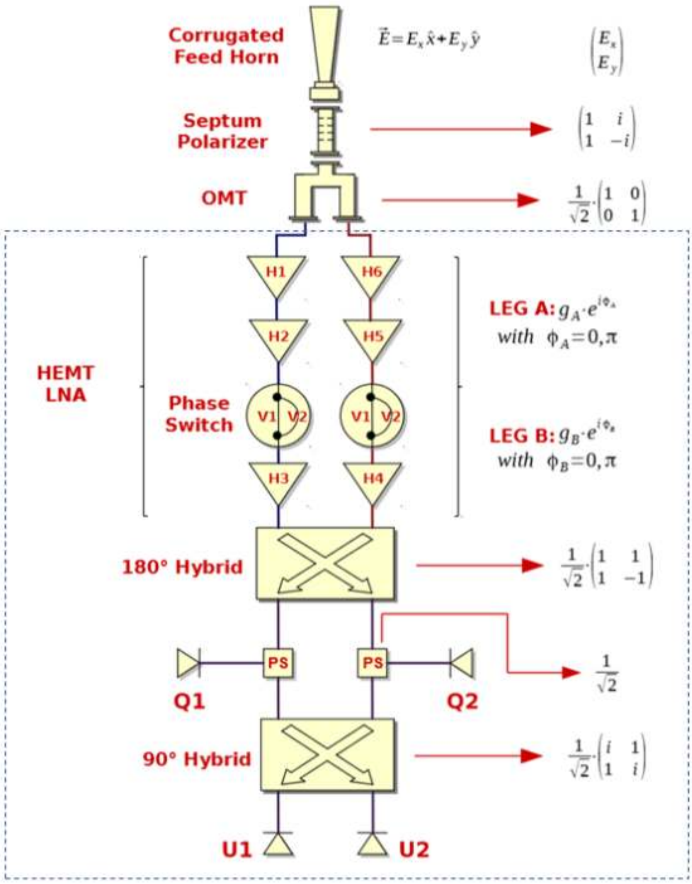

Figure 3.9: Schematic diagram of the polarimeter module. The components labeled on the diagram are described in the body of the text. The dashed line encloses the components which are phisically integrated into MMIC device.

Substituting the Jones matrixes into eq. 3.7 we obtain:

$$\begin{pmatrix} E_{Q_1} \\ E_{Q_2} \end{pmatrix} = \frac{1}{\sqrt{2}} \begin{pmatrix} 1 & 0 \\ 0 & 1 \end{pmatrix} \frac{1}{\sqrt{2}} \begin{pmatrix} 1 & 1 \\ 1 & \text{-1} \end{pmatrix} \begin{pmatrix} g_\text{A} & 0 \\ 0 & g_\text{B} \end{pmatrix} \begin{pmatrix} e^{i\phi_\text{A}} & 0 \\ 0 & e^{i\phi_\text{B}} \end{pmatrix} \begin{pmatrix} E_\text{A} \\ E_\text{B} \end{pmatrix}^{\text{in}} \tag{3.8}$$

In the same way, the description for the U signal is similar

$$\begin{pmatrix} E_{Q_1} \\ E_{Q_2} \end{pmatrix} = S^{\pi/2} S^{\text{PowSplit}} S^{\pi} S^{\text{amp}} S^{\text{PS}} \begin{pmatrix} E_\text{A} \\ E_\text{B} \end{pmatrix}^{\text{in}} \tag{3.9}$$

with the additional Jones matrix term of the $\pi/2$ hybrid

$$\begin{pmatrix} E_{U_1} \\ E_{U_2} \end{pmatrix} = \frac{1}{2\sqrt{2}} \begin{pmatrix} 1 & \text{i} \\ \text{i} & 1 \end{pmatrix} \begin{pmatrix} 1 & 0 \\ 0 & 1 \end{pmatrix} \begin{pmatrix} 1 & 1 \\ 1 & \text{-1} \end{pmatrix} \begin{pmatrix} g_\text{A} & 0 \\ 0 & g_\text{B} \end{pmatrix} \begin{pmatrix} e^{i\phi_\text{A}} & 0 \\ 0 & e^{i\phi_\text{B}} \end{pmatrix} \begin{pmatrix} E_\text{A} \\ E_\text{B} \end{pmatrix}^{\text{in}} \tag{3.10}$$

Signal acquired by detector

An expression of the signal acquired by the detectors with input from an OMT can be reached using this approximation: the phase switch on leg A has transmission 1, and leg B is switched. The phase can be represented as $(e^{i\phi_A}, e^{i\phi_B}) = (1, \pm 1)$. The output of OMT is left- and right-circularly polarized so we can write

$$\begin{pmatrix} E_\text{A} \\ E_\text{B} \end{pmatrix}^{\text{in}} = \frac{1}{\sqrt{2}} \begin{pmatrix} E_\text{LHCP} \\ E_\text{RHCP} \end{pmatrix} = \frac{1}{\sqrt{2}} \begin{pmatrix} E_\text{L} \\ E_\text{R} \end{pmatrix} = \frac{1}{\sqrt{2}} \begin{pmatrix} E_x + iE_y \\ E_x - iE_y \end{pmatrix} \tag{3.11}$$

Substituting eq. 3.11 into eq. 3.8 we obtain

$$\begin{pmatrix} E_{Q_1} \\ E_{Q_2} \end{pmatrix} = \frac{1}{2\sqrt{2}} \begin{pmatrix} g_\text{A} E_\text{L} \pm g_\text{B} E_\text{R} \\ g_\text{A} E_\text{L} \mp g_\text{B} E_\text{R} \end{pmatrix}. \tag{3.12}$$

The U signal is obtained substituting eq. 3.11 into eq. 3.10

$$\begin{pmatrix} E_{U_1} \\ E_{U_2} \end{pmatrix} = \frac{1}{4} \begin{pmatrix} (1+i) g_\text{A} E_\text{L} \pm (1-i) g_\text{B} E_\text{R} \\ (1+i) g_\text{A} E_\text{L} \mp (1+i) g_\text{B} E_\text{R} \end{pmatrix} \tag{3.13}$$

The eq. 3.8 and eq. 3.10 show the field at the Q_1, Q_2 and U_1, U_2 diodes. Now, we can see that the diodes square signal can be directly connected to the Q and U Stokes' parameters. The square module can be rewritten as

$$\begin{pmatrix} |E_{Q_1}|^2 \\ |E_{Q_2}|^2 \end{pmatrix} = \begin{pmatrix} Q_1 \\ Q_2 \end{pmatrix} = \frac{1}{8} \begin{pmatrix} g_\text{A}^2 E_\text{L} E_\text{L}^* + g_\text{B}^2 E_\text{R} E_\text{R}^* \pm g_\text{A} g_\text{B} \left(E_\text{L} E_\text{R}^* + E_\text{R} E_\text{L}^* \right) \\ g_\text{A}^2 E_\text{L} E_\text{L}^* + g_\text{B}^2 E_\text{R} E_\text{R}^* \mp g_\text{A} g_\text{B} \left(E_\text{L} E_\text{R}^* + E_\text{R} E_\text{L}^* \right) \end{pmatrix} \tag{3.14}$$

$$\begin{pmatrix} |E_{U_1}|^2 \\ |E_{U_2}|^2 \end{pmatrix} = \begin{pmatrix} U_1 \\ U_2 \end{pmatrix} = \frac{1}{8} \begin{pmatrix} g_\text{A}^2 E_\text{L} E_\text{L}^* + g_\text{B}^2 E_\text{R} E_\text{R}^* \pm i g_\text{A} g_\text{B} \left(E_\text{L} E_\text{R}^* - E_\text{R} E_\text{L}^* \right) \\ g_\text{A}^2 E_\text{L} E_\text{L}^* + g_\text{B}^2 E_\text{R} E_\text{R}^* \mp i g_\text{A} g_\text{B} \left(E_\text{L} E_\text{R}^* - E_\text{R} E_\text{L}^* \right) \end{pmatrix} \tag{3.15}$$

The eq. 3.14 and eq. 3.15 can be rewritten in terms of Stokes' parameters using the identities

$$\begin{aligned} I &= E_\text{L} E_\text{L}^* + E_\text{R} E_\text{R}^* = |E_\text{L}|^2 + |E_\text{R}|^2 = |E_x|^2 + |E_y|^2 \\ Q &= E_x E_x^* - E_y E_y^* = |E_x|^2 - |E_y|^2 = 2\Re \left[E_\text{L}^* E_\text{R} \right] \\ U &= -2\Im \left[E_\text{L}^* E_\text{R} \right] \\ V &= |E_\text{L}|^2 - |E_\text{R}|^2 \end{aligned} \tag{3.16}$$

For circular polarization, we can also use the following identities

$$
\begin{aligned}
E_{\mathrm{L}}E_{\mathrm{L}}^{*} &= \frac{I+V}{2} \\
E_{\mathrm{R}}E_{\mathrm{R}}^{*} &= \frac{I-V}{2} \\
\Re\left[E_{\mathrm{R}}E_{\mathrm{L}}^{*}\right] &= \Re\left[E_{\mathrm{R}}^{*}E_{\mathrm{L}}\right] \\
\Im\left[E_{\mathrm{R}}E_{\mathrm{L}}^{*}\right] &= -\Im\left[E_{\mathrm{R}}^{*}E_{\mathrm{L}}\right] \\
E_{\mathrm{R}}E_{\mathrm{L}}^{*} &= \Re\left[E_{\mathrm{R}}E_{\mathrm{L}}^{*}\right] + i\Im\left[E_{\mathrm{R}}E_{\mathrm{L}}^{*}\right] = \frac{Q}{2} - i\frac{U}{2} \\
E_{\mathrm{L}}E_{\mathrm{R}}^{*} &= \Re\left[E_{\mathrm{R}}E_{\mathrm{L}}^{*}\right] - i\Im\left[E_{\mathrm{R}}^{*}E_{\mathrm{L}}\right] = \frac{Q}{2} + i\frac{U}{2} \\
E_{\mathrm{L}}E_{\mathrm{R}}^{*} + E_{\mathrm{R}}E_{\mathrm{L}}^{*} &= Q \\
E_{\mathrm{L}}E_{\mathrm{R}}^{*} - E_{\mathrm{R}}E_{\mathrm{L}}^{*} &= iU
\end{aligned}
\tag{3.17}
$$

that can be substituted into the eq. 3.14 end eq. 3.15 to obtained

$$
\begin{pmatrix} Q_1 \\ Q_2 \end{pmatrix} = \frac{1}{8}\begin{pmatrix} g_{\mathrm{A}}^2(I+V)/2 + g_{\mathrm{B}}^2(I-V)/2 \pm g_{\mathrm{A}}g_{\mathrm{B}}Q \\ g_{\mathrm{A}}^2(I+V)/2 + g_{\mathrm{B}}^2(I-V)/2 \mp g_{\mathrm{A}}g_{\mathrm{B}}Q \end{pmatrix} \tag{3.18}
$$

$$
\begin{pmatrix} U_1 \\ U_2 \end{pmatrix} = \frac{1}{8}\begin{pmatrix} g_{\mathrm{A}}^2(I+V)/2 + g_{\mathrm{B}}^2(I-V)/2 \pm ig_{\mathrm{A}}g_{\mathrm{B}}(iU) \\ g_{\mathrm{A}}^2(I+V)/2 + g_{\mathrm{B}}^2(I-V)/2 \mp ig_{\mathrm{A}}g_{\mathrm{B}}(iU) \end{pmatrix} \tag{3.19}
$$

The terms $\propto g_A g_B$ change their signs under the action of the phase switches that can oscillate between the values $0, 2\pi$. The signal acquired by the diodes in a different configuration of the phase switches can be differenced ('demodulated') in order to remove those terms which are constant between the two phase-switches states. After the demodulation we obtained

$$
\begin{pmatrix} Q_1 \\ Q_2 \\ U_1 \\ U_2 \end{pmatrix}^{\text{demod.}} = \frac{1}{4}\begin{pmatrix} g_A g_B Q \\ -g_A g_B Q \\ -g_A g_B U \\ g_A g_B U \end{pmatrix} \tag{3.20}
$$

In this way, the differenced voltage on the Q diodes is a measure of the Q Stokes's parameter, and the differenced voltage on the U diodes is a measure of the U Stokes' parameter.

3.3.6 Leakage from intensity to polarization

In the previous section, we consider a perfected balanced system and only the signal of one leg was modulated by a phase switch. In this section, we consider the two legs characterized by different transmission coefficients and we modulate the phase of both legs of the polarimeter. The possible states for $e^{i\phi_{\mathrm{A}}}$ now are $(1, \beta_{\mathrm{A}})$, and similarly for $e^{i\phi_{\mathrm{B}}}$ that can assume values between $(1, \beta_{\mathrm{B}})$.

To evaluate the effects of the legs imbalance we start from the Jones matrix for an imbalanced phase switch circuit and discuss the impact of switching both legs.

Thus phase switching the B leg between 1 and $-\beta_{\mathrm{B}}$ will yield two possible output values, depending on the phase-switch state of leg A (one for $e^{i\phi_{\mathrm{A}}}=1$, one for $e^{i\phi_{\mathrm{A}}}=-\beta_{\mathrm{A}}$).

$$\begin{pmatrix} e^{i\phi_{\mathrm{A}}} & 0 \\ 0 & e^{i\phi_{\mathrm{B}}} \end{pmatrix} = \begin{pmatrix} {}^{+1}_{-\beta_{\mathrm{A}}} & 0 \\ 0 & {}^{+1}_{-\beta_{\mathrm{B}}} \end{pmatrix} \tag{3.21}$$

Differencing the signal between the two phase-switches states on the B leg will yield a demodulated stream, for two example diodes, of:

$$\begin{pmatrix} (1,1)-(1,-\beta_{\mathrm{A}}) \\ (-\beta_{\mathrm{A}},1)-(-\beta_{\mathrm{A}},-\beta_{\mathrm{B}}) \end{pmatrix}^{Q_1} = \frac{1}{4}\begin{pmatrix} g_{\mathrm{B}}^2(1-\beta_{\mathrm{B}}^2)E_{\mathrm{R}}E_{\mathrm{R}}^* + g_{\mathrm{A}}g_{\mathrm{B}}(E_{\mathrm{L}}E_{\mathrm{R}}^* + E_{\mathrm{R}}E_{\mathrm{L}}^*) \\ g_{\mathrm{B}}^2(1-\beta_{\mathrm{B}}^2)E_{\mathrm{R}}E_{\mathrm{R}}^* + \beta_{\mathrm{A}}g_{\mathrm{A}}g_{\mathrm{B}}(E_{\mathrm{L}}E_{\mathrm{R}}^* + E_{\mathrm{R}}E_{\mathrm{L}}^*) \end{pmatrix} \tag{3.22}$$

$$\begin{pmatrix} (1,1)-(1,-\beta_{\mathrm{A}}) \\ (-\beta_{\mathrm{A}},1)-(-\beta_{\mathrm{A}},-\beta_{\mathrm{B}}) \end{pmatrix}^{U_1} = \frac{1}{4}\begin{pmatrix} g_{\mathrm{B}}^2(1-\beta_{\mathrm{B}}^2)E_{\mathrm{R}}E_{\mathrm{R}}^* + ig_{\mathrm{A}}g_{\mathrm{B}}(E_{\mathrm{L}}E_{\mathrm{R}}^* - E_{\mathrm{R}}E_{\mathrm{L}}^*) \\ g_{\mathrm{B}}^2(1-\beta_{\mathrm{B}}^2)E_{\mathrm{R}}E_{\mathrm{R}}^* + i\beta_{\mathrm{A}}g_{\mathrm{A}}g_{\mathrm{B}}(E_{\mathrm{L}}E_{\mathrm{R}}^* - E_{\mathrm{R}}E_{\mathrm{L}}^*) \end{pmatrix} \tag{3.23}$$

In this case, the diodes stream contains the term $g_B^2(1-\beta_B^2)E_RE_R^* = g_B^2(1-\beta_B^2)(I-V)/2$. This contribution represents the leakage from total power, represented by the Stokes' parameter I, into polarization and it is dependent on the gain in only one leg (in this case, g_B).

This polarimeter design permits getting rid of the intensity of polarization leakage. The signal can be demodulated to have no contributions from total power and depend on the gain from both legs equally. Phase switching a second time and differencing again (this process is called *double demodulation*)

$$\begin{pmatrix} Q_1 \\ Q_2 \\ U_1 \\ U_2 \end{pmatrix}^{doubleDemod.} = \frac{1}{4}\begin{pmatrix} g_Ag_B(1+\beta_A)(1+\beta_B)Q \\ -g_Ag_B(1+\beta_A)(1+\beta_B)Q \\ -g_Ag_B(1+\beta_A)(1+\beta_B)U \\ g_Ag_B(1+\beta_A)(1+\beta_B)U \end{pmatrix} \tag{3.24}$$

The result presented in eq. 3.24 does not depend on the total intensity I. The diode streams depend on the gain of amplifiers and transmission terms that can be measured and characterized in a laboratory with a *Vector Network Analyzer* - VNA.

Characterization of the Q-band polarimeter

Previously, we described how the polarimeter module works and the expected signals at the diode levels in case of balance (with only one operating phase switch) and imbalance (with both operating phase-switch on both legs).

We described each component of the polarimetric chain in terms of Jones' matrix of a *theorethical components*, with no imperfections. The real components are affected by unavoidable imperfections due to natural manufacturing limits. For this reason, we expected a non-zero leakage from the total intensity to the polarized channel that can be assessed only by directly measuring the components with a VNA.

Fig. 3.10 shows only a part of the measurements performed by Virone et al. (2014). In the plots are represented the leakage coefficients from total intensity to the measure of Q and the measure of U (see Virone et al. (2014) for more details on the measurements). The system frame of Q and U represented in these plots is concerning the focal plane. For this reason, we can call them Q_{fp} and U_{fp}. The Q_{sky} and U_{sky} are not aligned with those given with respect to the focal plane system. A constant elevation scan creates a polarization field rotation in the frame of the sky, and polarization leakage from $I \rightarrow Q_{fp}$ can be considered equally distributed by Q_{sky} and U_{sky}.

In spite of the Fig. 3.10 shows a higher level of leakage from $I \rightarrow Q_{pf}$, in this work we can consider a general leakage from $I \rightarrow P$ (where P, is a generic polarized channel Q, U, with respect to the sky system) of the order of 1%.

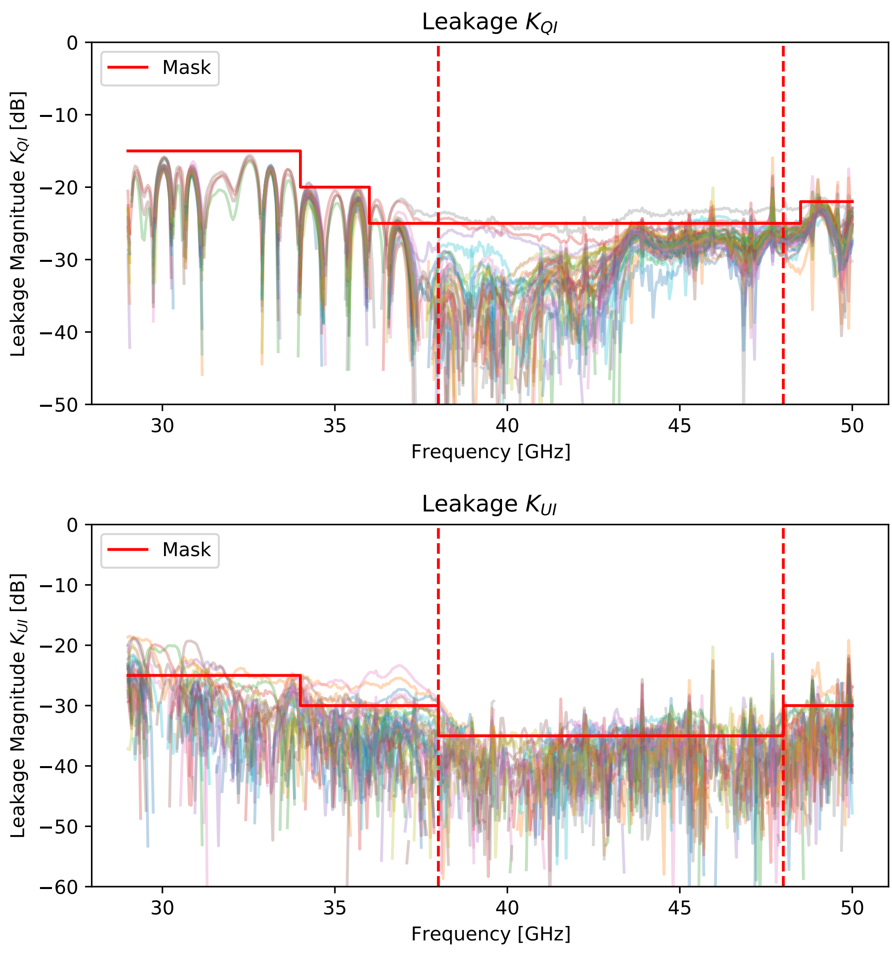

Figure 3.10: Leakage from intensity to polarization generated by the polarizer-OMT assembly evaluated for Q and U defined in the frame of reference of the focal plane.

Chapter 4

The Atmospheric Model

The atmosphere is a dispersive medium characterized by a complex electrical permittivity $\varepsilon = \varepsilon_{\mathrm{R}} + i\varepsilon_{\mathrm{I}}$. The contribution to the complex permittivity is due mostly to the water vapor H_2O and dioxygen molecules O_2 that are dissolved in the atmosphere. The imaginary part of ε is proportional to the atmospheric absorption coefficient α_ν: $\varepsilon_{\mathrm{I}} = \lambda\alpha_\nu/4\pi$, while the real part is proportional to the atmospheric refractive index n: $\varepsilon_{\mathrm{R}} \propto s\sqrt{n}$.

The O_2 molecules are well mixed in the atmosphere but the water vapor is distributed inhomogeneously creating significant spatial distribution fluctuations of its concentration. The spatial fluctuations are blow by wind creating a non-trivial dynamic. The theory of water-vapor flutuactions dynamic was firstly described by Frisch & Kolmogorov (1995) that was proficiently refined for wave propagation in a random medium by Chernov (2017) and Tatarski (2016) for electromagnetic wave propagation in a turbulent medium.

A telescope, with a given focal plane, that observes the sky through these structures, inevitably detect these spurious correlations observing a non-zero cross-correlations between near detectors. This spurious correlations have to be removed by the CMB correlations in order to obtain the cosmological information.

Several algorithms are used to remove correlated noise from radiometric time-streams, like the *MADAM* by Keihänen et al. (2010); Kurki-Suonio et al. (2009), assuming that the cross-correlated noise among the various detectors is negligible. It is not the case for fluctuations induced by the atmosphere. This can be seen in Fig. 4.1, which shows a simulation of the correlation between the Strip detectors for the typical month of January. The details of the simulations are discussed in the next chapter.

Another atmospheric effect involved in the CMB ground-based measurements is due to the fluctuations of the atmospheric refractive index. The real and imaginary parts of ε are linked by Kramers (1927) and Krönig (1926) relations. For this reason, a change in water vapor density affects both the absorption coefficient and the refractive index. The refractive index fluctuations affect the telescope pointing direction introducing an extra source of uncertainties in the pointing of each detector.

This work does not cover this effect because, as shown by Church (1995), the impact of the ε_R fluctuations on the cosmological information is of the secondary order compared with the atmospheric absorption. We have not investigated the effects of a fluctuating refractive index on the cosmological target yet, but we started to assess this effect which will be the main topic of a dedicated paper (*M. Maris et al. - in preparation*).

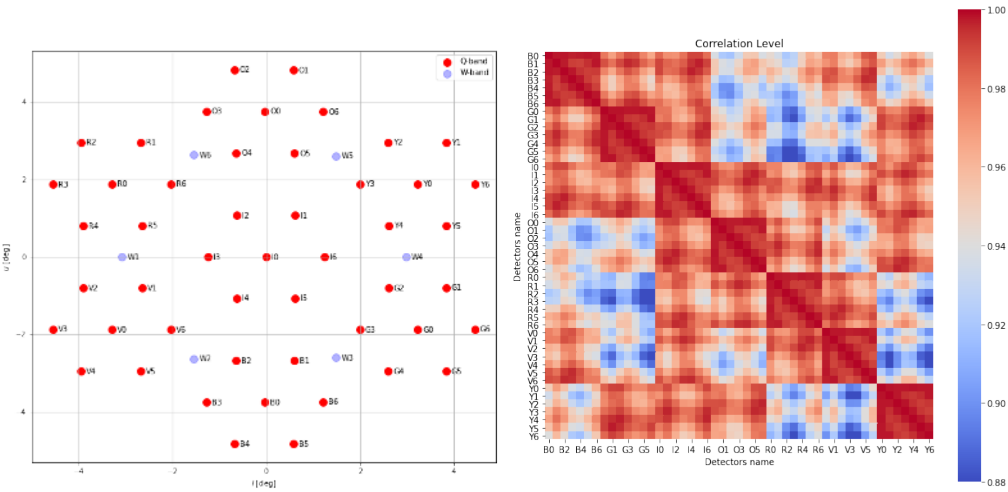

Figure 4.1: *Left panel:* sky projection of the Strip focal plane. Q-band receivers are represented in red, W-band receivers in blue *Right panel:* correlation level among the detectors of the focal plane after one month of observations during a typical January. We can see that the level of cross correlation is particularly strong, in particular among detectors within the same hexagonal module.

4.1 The equation of the atmospheric radiative transfer

Radiation absorption and emission in the atmosphere are controlled by the *radiative transfer equation*. In our case the radiative transfer equation can be used in *Earth Low Atmosphere* - ELA - approximation (with this term, we want to identify the troposphere that starts from the ground up to about 10 km). The radiative transfer equation in this approximation is given by:

$$\frac{dI_\nu}{ds} = -\alpha_\nu I_\nu + j_\nu, \tag{4.1}$$

where I_ν is the specific intensity, s is the path along the line of sight, α_ν is the absorption coefficient and j_ν is the emission coefficient. This equation tells us that the atmosphere absorbs a part of the incoming radiation and emits its own radiation because of excitation and subsequently decay of the vibrational and rotational levels of the H_2O and O_2 molecules.

At the full thermodynamic equilibrium, the relationship between absorbed and emitted radiation is given by the *Kirkchhoff equation*:

$$B_\nu(T) = \frac{j_\nu(T)}{\alpha_\nu(T)}. \tag{4.2}$$

Kirchhoff's law, shown in eq. 4.2, is valid also for systems at *local* thermodynamic equilibrium (LTE) like the atmosphere in earth low approximation. The proposition *local* is mandatory ELA atmosphere because it is represented by gas at the thermodynamical equilibrium where the molecules have a Maxwellian velocity distribution. However, it is in a nonequilibrium radiation field (generated mostly by the sun during the day, the cold dark sky at night, and the anisotropic ground emissions).

The relationship between the specific intensity, I_ν, and the brightness temperature, $T_\mathrm{b}(\nu)$, is provided by:

$$T_\mathrm{b}(\nu) \stackrel{\mathrm{def}}{=} \frac{I_\nu c^2}{2k_\mathrm{B}\nu^2}, \tag{4.3}$$

that allows one to convert the specific intensity, I_ν, from MJy/sr to $\mathrm{K_{RJ}}$.

Equation 4.1 can be solved numerically using various algorithms. The codes considered in this work are *Atmospheric Model* - AM by Paine (2019), which uses vertical atmospheric profile and *Cmb Atmospheric Library* - CAL by Mandelli et al. (2021), developed by me and based on the TOAST framework developed by Kisner et al. (2020).

At the LTE regime, the emission coefficient can be rewritten using the Kirkchhoff law

$$j_\nu = \alpha_\nu \, B_\nu\left(T^\mathrm{ph}_\mathrm{atm}\right), \tag{4.4}$$

and a possible solution of the equation 4.1 is given by:

$$\begin{aligned} \frac{1}{\alpha_\nu}\frac{dI_\nu}{ds} &= -\frac{dI_\nu}{d\tau} = -I_\nu + B_\nu\left(T^\mathrm{ph}_\mathrm{atm}\right) \\ \int_0^{\tau_A} e^{-\tau}\frac{dI_\nu}{d\tau}d\tau &= \int_0^{\tau_A}\left[I_\nu - B_\nu\left(T^\mathrm{ph}_\mathrm{atm}\right)\right]\, e^{-\tau}\, d\tau \\ I_\nu(\tau=\tau_\mathrm{A})\, e^{-\tau_\mathrm{A}} - I_\nu(\tau=0) &= B_\nu\left(T^\mathrm{ph}_\mathrm{atm}\right)\, (e^{-\tau_A}-1). \end{aligned} \tag{4.5}$$

where τ is the atmospheric optical depth. Using the equations 4.2 and 4.3, we can rewrite the solution 4.5 as follows:

$$T_\mathrm{cmb}(\nu)\cdot e^{-\tau_\mathrm{A}(\nu)} - T_\mathrm{sky}(\nu) = T^\mathrm{ph}_\mathrm{atm}\left(e^{-\tau_\mathrm{A}(\nu)}-1\right) \tag{4.6}$$

$$T_\mathrm{sky}(\nu) = T_\mathrm{cmb}(\nu)\, e^{-\tau_\mathrm{A}(\nu)} + T^\mathrm{ph}_\mathrm{atm}\left(1-e^{-\tau_\mathrm{A}(\nu)}\right). \tag{4.7}$$

In the RJ approximation, the CMB contribution $T_\mathrm{cmb}\, e^{-\tau_\mathrm{A}}$ is not negligible so we must account for it in estimating the atmosphere brightness temperature. Both the numerical codes return the atmosphere optical depth, so for any ν, we can correct the T_sky in order to obtain only the atmospheric antenna temperature $T^\mathrm{A}_\mathrm{atm}$. We are interested in the T_atm because we want to compare our simulation with QUIJOTE data that are released in terms of T_atm without the CMB contribution.

$$T^\mathrm{A}_\mathrm{atm} = T_\mathrm{sky} - T_\mathrm{cmb}\cdot e^{-\tau_\mathrm{A}} \tag{4.8}$$

The brightness temperature of the atmosphere is also dependent on the thickness of the air column. Following Kasten & Young (1989), the air mass function m and the zenithal angle ϑ_zth are linked by the relation:

$$m(\vartheta_\mathrm{zth}) = \frac{1}{\cos(\vartheta_\mathrm{zth}) + 0.50572(96.07995-\vartheta_\mathrm{zth})^{-1.6364}}. \tag{4.9}$$

Therefore, we can write the atmosphere optical depth at a given zenith angle, $\vartheta_{\rm zth}$, as $\tau_{\rm A}(\vartheta_{\rm zth}) = \tau_{\rm A,0} \times m(\vartheta_{\rm zth})$, where $\tau_{\rm A,0}$ is the optical depth at the zenith.

For zenith angles up to $\sim 70°$ we can use the following approximation, which is accurate to better than 1%:

$$m\left(\vartheta_{\rm zth}\right) \approx \frac{1}{\cos(\vartheta_{\rm zth})}. \tag{4.10}$$

4.2 The statistical picture of the atmosphere

In this section is presented the atmosphere statistics using a limited set of parameters: the precipitable water vapor, PWV, the surface temperature, $T_{\rm s}$, the surface pressure, $P_{\rm s}$, and wind velocity and direction. The cumulative distribution function - CDF - of each parameter is used to prepare the initial conditions of a typical atmosphere on Teide observatory.

The data used to create the CDFs are provided by ERA-5[1] reanalysis dataset. An atmospheric reanalysis - like ERA-5 - estimates the history of the atmosphere using a numerical model to assimilate historical measurements, it means that ERA-5 reanalysis relies on a mathematical model - the *General Circulation Model* GCM - algorithm (McGuffie & Henderson-Sellers 2014), which uses the measurements to add additional forcing terms into the GCM model to correct the numerical exponential divengencies and produce data homogeneously gridded with high spatial and temporal resolution.

I used the reanalysis data because the weather measurements recorded are not evenly distributed around the globe, and are not homogeneous in time. Climate reanalysis resolves this problem by combining current and past observations with the GSC weather model to deliver a complete and consistent description of the weather over time.

For example, we can imagine the past weather as a series of jigsaw puzzles with pieces missing in some places or overlapping in others. The various pieces are characterized by weather observations from ground-weather stations, weather balloons, aircraft, ships, satellites, and often data from local weather services. The reanalysis combines and processes all the information from those pieces to blend overlapping pieces and recreate the missing parts to complete consistently the weather picture of all over the globe through time with 1-hour time resolution from the Earth's surface to the top of the atmosphere.

In my work, I have generated the CDFs of the atmosphere parameters of the atmosphere above Teide Observatory extracting from the ERA-5 historical dataset from 1980 to 2020 with a 1-hour time resolution.

A graphical representation of a collection of CDFs of the PWV is shown in the left panel of Fig. 4.2. It is composed of twelve matrices, one for each month. Each row represents the CDF of a specific hour, of a typical day of that month. For example, row zero of the January matrix represents the cumulative PWV distribution function for a typical day of January at midnight UTC.

The right panel of Fig. 4.2 represents the same information seen from another point of view. In particular, each plot represents a specific hour of the day. For every hour,

[1] `https://www.ecmwf.int`

the plot displays the CDF of the PWV for each month and compares the PWV seasonal fluctuations at the same UTC hour.

All the CDFs are stored in a `.fits` file of few MB, that I call *weather-file*. This file can be used by instrument simulation frameworks like TOAST (Kisner et al. 2020), $\text{QUBIC}_{\text{Soft}}$[2] and Stripeline[3].

We chose to store the CDFs rather than probability density functions because the former is more reliable and easy to handle than the PDFs. Given the dataset, the CDFs can be built with a simple sorting algorithm. For example, Fig. 4.3 represents a collection of CDFs of the PWV that were evaluated at two different confidence levels - C.L. Every pixel represents the CDFs of that specific hour of a typical day of that specific month, evaluated at a certain C.L.

For the specific purpose of my thesis, I developed a specific C++ framework based on TOAST, called *CMB Atmospheric Library* - CAL -, in order to produce atmospheric simulations for a ground-based telescope. The modular nature of this framework is such that it can be compiled and used by other instrumental frameworks even if written in different languages.

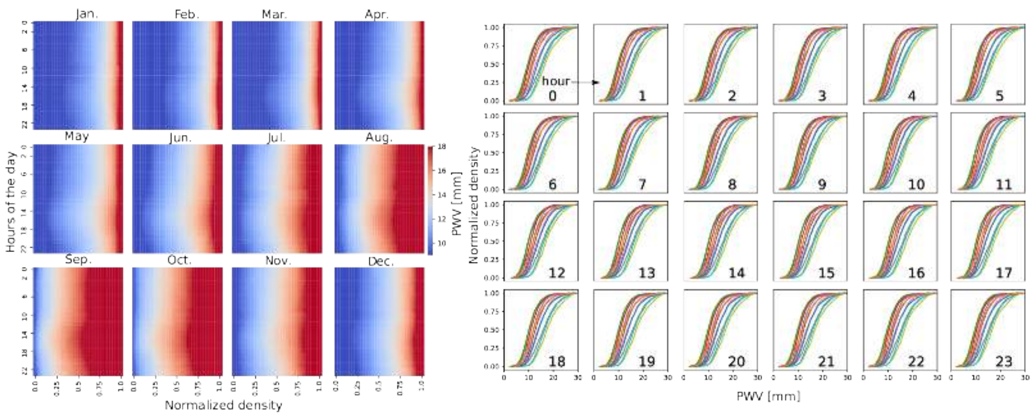

Figure 4.2: *Left-Panel*: CDFs of the PWV above the Teide Observatory obtained from the ERA5 data. Every row represents the CDF associated which that hour of a typical day of that month. In this way, we can extract a random atmospheric realization described by the parameters (PWV, T_0, P_0), where PWV is the precipitable water vapor (in mm), T_0 is the surface temperature and P_0 is the surface pressure. The same CDF organization is also repeated for T_0 and P_0. *Right-Panel*: same CDFs of the left-panel with a particular focus on the hour of the day. Each plot is relative to an hour of the day and contains twelve CDFs, one for each month. This representation is convenient for assessing the seasonal fluctuations of the PWV at the same UTC hour.

[2]`https://github.com/qubicsoft/qubic`
[3]`https://github.com/lspestrip/Stripeline.jl`

Example of input data

In this section, I present a possible representation of the atmospheric statistical realization that it used as input data of the TOAST framework (and, more in general, of all those frameworks that are based on TOAST). The file with the CDFs, presented in Fig. **??**, actually represents a statistical picture of the atmosphere. From the CDFs is difficult to see that, but if we evaluate them at a given CL value and plot the value as a function of the hour of the day of a typical day of a given month, the meaning can be more clear. This is what is represented in Fig. 4.3. Independently from the C.L., the Fig. 4.3 can be

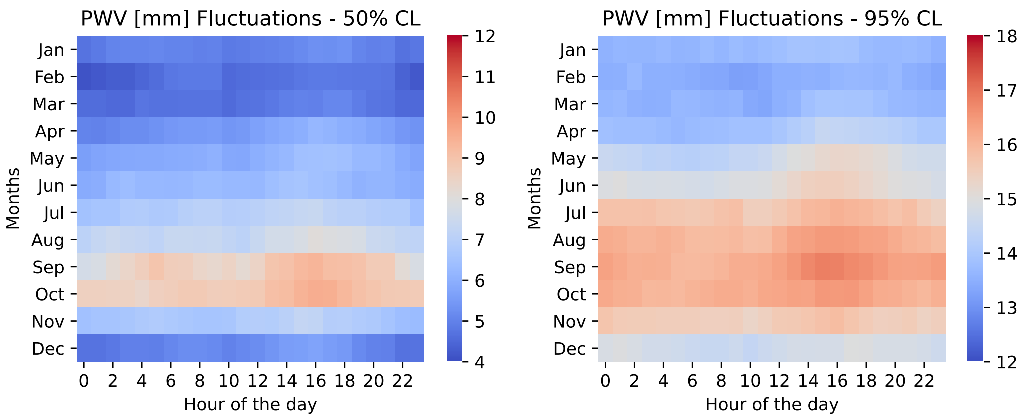

Figure 4.3: In this example we report the PWV CDFs above Teide Observatory at two different confidence levels (C.L.), 50% (left panel) and 95% (right panel). The first one represents the median of the PWV fluctuations, and compared with the second one, the first is the most representative of the actual weather conditions above the Strip telescope. In the first case rare events like very bad weather conditions, heavy rain, snow and extremely strong wind gusts are not considered, as in these cases the telescope will not take measurements.

read as, for each row, that represents a typical (median or 95% of CL) day of the month on the label, we can observe the PWV fluctuation as a function of the hour of the day. Similarly, each column represents the seasonal fluctuation of the PWV at the same UTC hour. Consider the worst condition represented by the 16:00 UTC. The column of that hour represents how the PWV changes as a function of the seasons. It peaks between Aug. - Oct (the summertime in the northern hemisphere) and the minimum is between Dec. - Jan. - Feb. during the wintertime.

4.2.1 The spatial resolution

The ERA-5 reanalysis data are released with a spatial resolution of $\sim (0.25^\circ \times 0.25^\circ)$ over the entire Earth's surface. These data represent the state-of-the-art meteorological reanalysis of the Earth's weather fluctuations on long-time scales. This resolution, however, is not enough for our purpose.

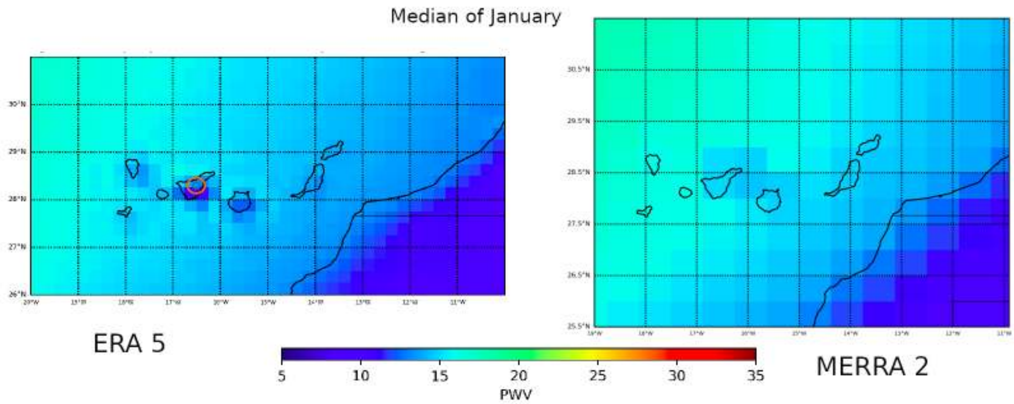

Figure 4.4: Median January PWV above the Canary islands derived from ERA5 (left panel) and MERRA2 (right panel) reanalyses.

We are interested in simulating the atmospheric fluctuations on both long (seasonal fluctuations) and short (sampling period) time scales. On the one hand, we have to consider the seasonal variation of the weather parameter, but we also have to take into account the changes in turbulent structures caused by the winds.

Reanalysis data like MERRA2 and ERA5 lack the necessary spatial resolution to reproduce the weather in a small location like Teide Observatory, characterized by a small land environment surrounded by the ocean. For example, in Fig. 4.4 I show the January PWV median above the Canary Islands obtained from ERA5 (left panel) and MERRA2 (right panel) reanalyses. Although the data shown in Fig. 4.4, are self-consistent the spatial resolution is not enough to describe accurately the atmospheric conditions above Tenerife, because the land surface is of the order of the surface of one resolution element (31 km×36 km in the case of ERA5).

Fig. 4.5 shows an example that highlights the problem of spatial resolution. In the top panels we see the PWV distribution above the Canary Islands during the day 01 - Jan. - 1980 at the hour 00:00 UTC. We see that the Tenerife island is covered only by a few pixels and the Pico del Teide is covered only by a small portion of only one pixel. The same problem also affects the maps of the surface temperature and surface pressure.

The pixel is surrounded by a purple box that contains the Strip observation site, but it covers also a portion of the island with altitudes below the 2390 m.o.s.l. and a part of the ocean. Therefore, the atmosphere behavior in the area covered by this pixel results from three different contributions: **(i)** the observation site, **(ii)** lands at altitudes below 2390 m and **(iii)** the ocean (which is the dominant contribution).

In the next sections, I will show how I mitigated the problem caused by the low spatial resolution of ERA-5 reanalysis with a combination of vertical atmospheric profiles acquired at Izaña during 2018 and of radiometric measurements performed with the QUIJOTE instrument.

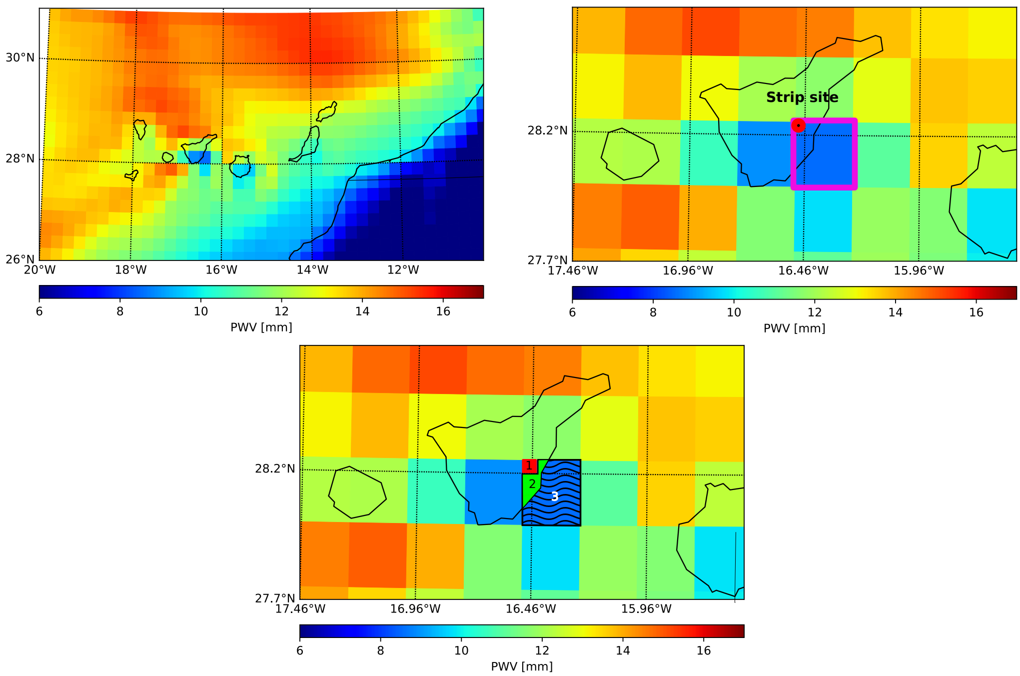

Figure 4.5: *Top-Left panel*: PWV spatial distribution derived from ERA-5 above the Canary islands on 1 - January - 1980 at 00:00 UTC. The data are released by ERA-5 spatially gridded with a pixel-size of 31 × 36 km. *Top-Right Panel*: A magnification of the left panel over Tenerife Island. The red point shows the location of the LSPE/Strip telescope. The red boxed pixel was used for building the CDF of the weather parameters. *Bottom Panel*: The pixel that contains the Strip site has been divided into three different parts: **1 - red zone**: the LSPE/Strip site, **2 - green zone**: Tenerife lands of Tenerife below 2390 m and **3 - blue, wavy zone**: the ocean.

4.2.2 Comparison of simulations with QUIJOTE data

I checked the weather CDFs obtained with CAL by comparing the simulated atmosphere brightness temperatures using eq. 4.1 with those obtained from the QUIJOTE (Rubiño-Martín et al. 2010) experiment.

In my simulations, I extracted the weather parameters using a Monte Carlo process with the acceptance ratio that is given by the CDFs evaluated before.

For QUIJOTE I used T_{atm} data measured by the *Multi-Frequency Instrument* - MFI, that operates since November 2012 in four frequency bands centered at 11.2 GHz, 12.9 GHz, 16.7 GHz, and 18.7 GHz.

Fig. 4.3 shows that the median PWV fluctuations are significantly higher for an excellent observational site like Pico del Teide. For the winter season, the PWV dissolved in the atmosphere oscillates between 4-5 mm at CL 50%, and 12-15 mm at CL 95% compared with the 2.5mm measured at Izaña.

In Fig. 4.6 I show the comparison between the data simulated with CAL, and the atmospheric temperatures derived by QUIJOTE measurements. We can appreciate a mismatch, in particular for the higher frequency channels. The simulations performed with CAL using the ERA-5 statistical picture predict a higher T^{A}_{atm} compared to QUIJOTE measurements. In Fig. 4.7 I show the same comparison using the data distribution functions. We see that the distance between the two peaks increases with frequency, confirming the results in Fig. 4.6.

The discrepancy presented in Fig. 4.6 and Fig. 4.7 results from the poor spatial resolution of the ERA-5 data, which leads to an overestimate of the water vapor taken into account to evaluate the atmospheric brightness temperature compared to the true weather situation above the Pico del Teide. In the simulations, most of the water vapor comes from the ocean and lands below 2390 m (see bottom panel of Fig. 4.5).

To solve this discrepancy, I have used the measurements of the atmospheric parameters (temperature, pressure, PWV) vertical profiles measured by the Izaña weather center during the year 2018. The balloon probe measurements more closely represent the atmosphere above the site and can be used to calibrate the simulations.

The vertical profiles are characterized by low temporal resolution because of the slow vertical speed of the balloon. A balloon probe can measure up to two profiles per day, and the various measurements can be used to obtain seasonal or yearly statistical vertical profiles. In Fig.. 4.8 I show the median yearly vertical profile derived from balloon measurements.

Using the median yearly vertical profile shown in Fig. 4.8, I simulated the atmosphere brightness temperature with the AM software and compared them with CAL simulations based on ERA-5 data.

Because the brightness temperatures derived with AM using the measured vertical profiles and those derived with CAL using the ERA5 CDFs should in principle be compatible as they represent the statistical picture of the same area we can use the AM simulations to calibrate CAL.

In Fig. 4.9 I show the distribution of the weather parameters derived using CAL with the ERA-5 dataset. The median of the parameters is presented in Tab. 4.1.

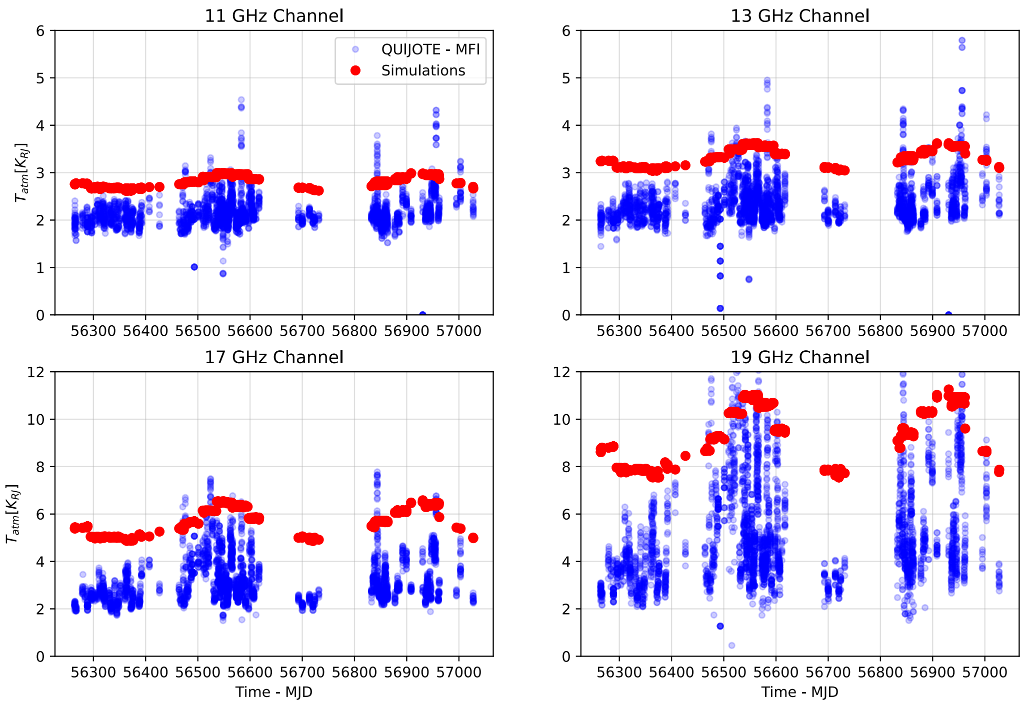

Figure 4.6: Comparison between the data simulated with the RAW CDFs derived from ERA5 and those derived from QUIJOTE measurements. We can appreciate that the atmospheric brightness temperatures simulated with CAL are always higher than the measured ones.

Table 4.1: Median of the weather parameters realization, performed with CAL.

Parameter	Median
Precipitable water vapor	12.5 mm
Surface temperature t_0	289.1 K
Surface pressure p_0	92764 Pa

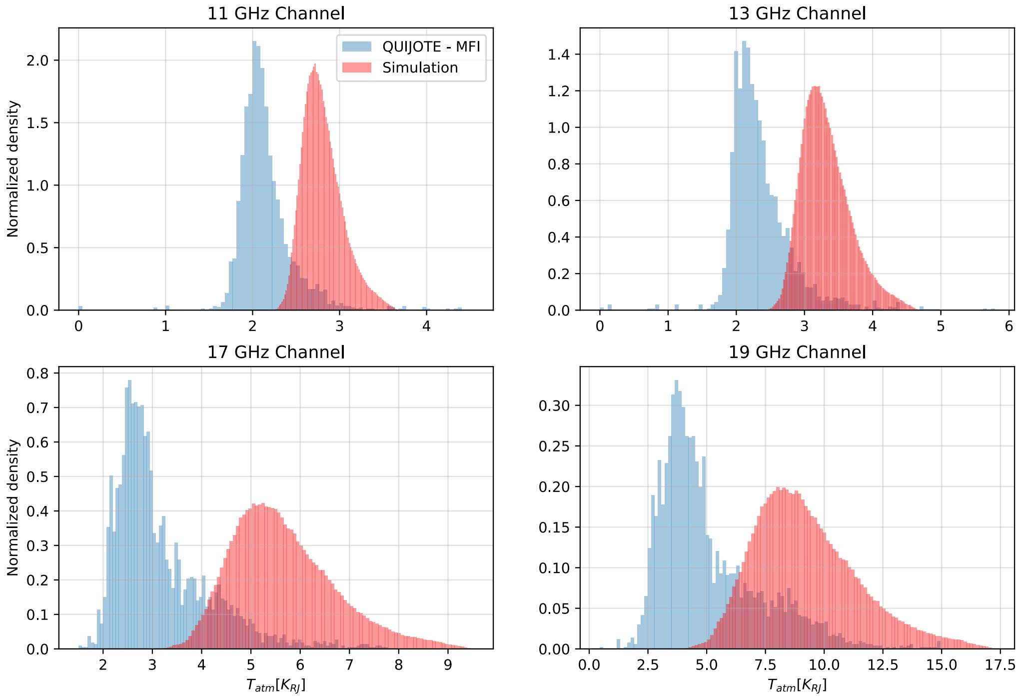

Figure 4.7: Comparison between the distributions of the atmosphere brightness temperature simulated with CAL and measured by QUIJOTE. This comparison confirms the mismatch between measurements and simulations shown in Fig. 4.6.

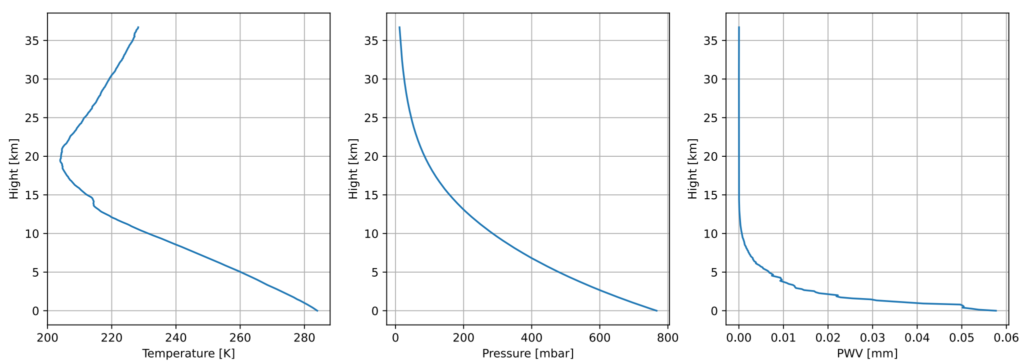

Figure 4.8: Annual median of all vertical profiles of atmosphere parameters acquired during 2018 by the Izaña weather center.

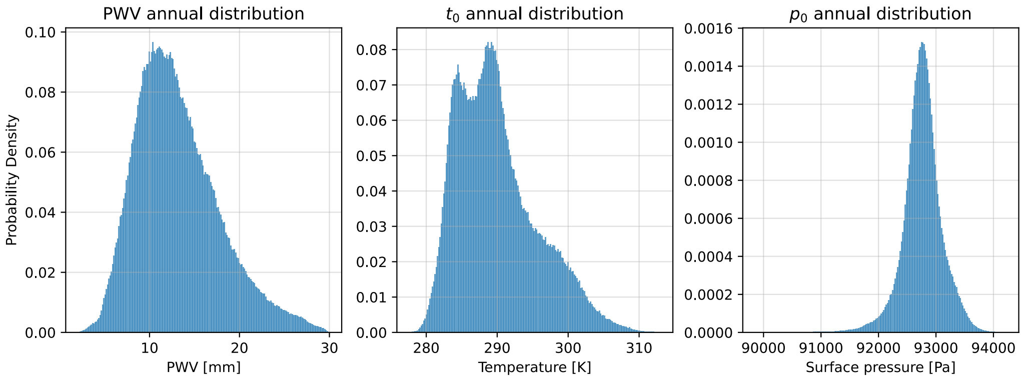

Figure 4.9: Annual distribution of the Precipitable water vapor, surface temperature and surface pressure generated with CAL with the ERA-5 dataset.

In the left panel of Fig. 4.10 we show the atmosphere brightness temperature versus frequency simulated with CAL (with the values provided in Tab. 4.1) and AM (with measured vertical profiles). The right panel shows the ratio of the two curves ($k_\nu = (T^{\rm A}_{\rm atm,AM}/T^{\rm A}_{\rm atm,CAL})$), which represents the extra contribution in $T^{\rm A}_{\rm atm}$ due to the higher PWV in the ERA-5 CDFs.

Assuming that the ERA-5 spatial resolution is enough to consider a constant ratio between the parameters above the observing site and the other parts of the ERA-5 pixel, we can consider the coefficient k_ν constant in time.

In Fig. 4.11 we check the consistency of my calibration procedure with QUIJOTE measurements by showing the ratio between the QUIJOTE measurements and CAL simulations (red dots) compared with the k_ν parameter. We can see that the two ratios are consistent, which underlines the robustness of the calibration procedure.

Now, we can use the k_ν coefficient to correct the atmospheric brightness temperature evaluated with CAL. Eq. 4.8 can be rewritten as follows

$$T^{\rm A}_{\rm atm}(\nu, P_0, T_0, {\rm PWV}) = \left(T_{\rm sky}(\nu, P_0, T_0, {\rm PWV}) - T_{\rm CMB}(\nu) \cdot e^{-\tau_{\rm A}(\nu, P_0, T_0, {\rm PWV})}\right) \cdot k_\nu \quad (4.11)$$

QUIJOTE measurements

We can now compare the atmosphere brightness temperature derived from QUIJOTE measurements with CAL simulations corrected with the calibration factor, k_ν. I present this comparison in the four panels of Fig. 4.12. The bottom panel represents the boxplot of the residuals for each frequency channel. We can appreciate that all the points are compatible with zero within a CL of 95%. Also, the statistical distributions of the atmosphere brightness temperature relative to simulations and measurements are consistent (see Fig. 4.14).

We notice that the error bar for the 19 GHz channel is significantly larger than other channels. This behavior is confirmed in Fig. 4.14 where the 19 GHz distribution, made

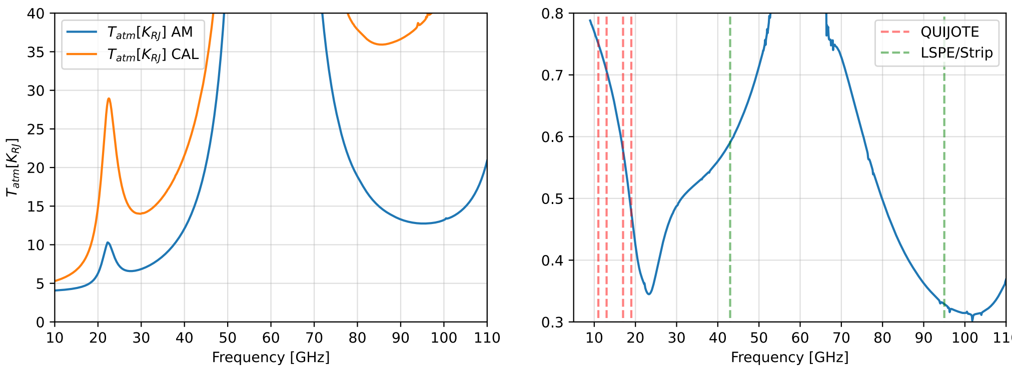

Figure 4.10: *Left panel*: atmosphere brightness temperature versus frequency simulated with CAL (orange line) and AM (blue line). *Right panel:* Calibration coefficient obtained from the ratio between AM and CAL curves.

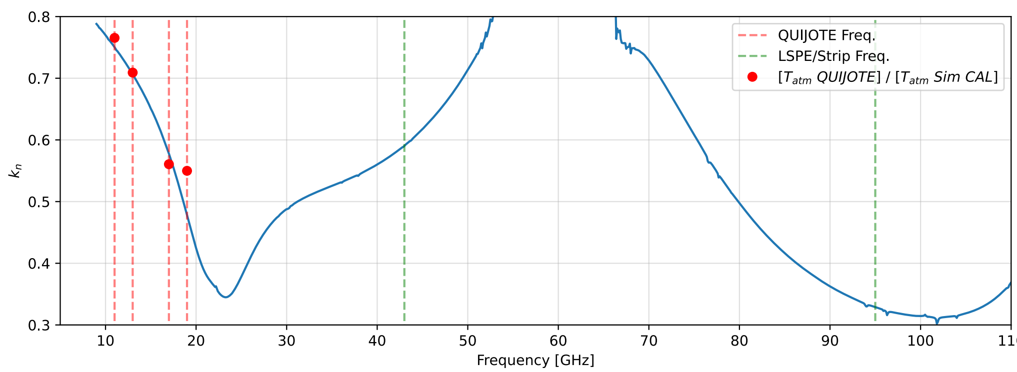

Figure 4.11: Comparison between AM/CAL and QUIJOTE/CAL ratios. The points are the ratio between QUIJOTE-MFI data and CAL simulations. They are compatible with the pattern evaluated with AM (using the median annual vertical profiles) and CAL (using the distribution generated in Fig. 4.9)

with the QUIJOTE data, is very asymmetric. At higher frequencies, we get closer to the water vapor line at 22 GHz. In this way, the sensitivity of the instrument to the water vapor in the atmosphere is greater than 11 GHz. Moreover, the FWHM of the 19 GHz beam is narrower than the 11 GHz channel and it is characterized by a greater resolution. The increase in resolution and sensitivity to the water vapor resolve the smallest atmospheric structures. These statements cannot be verified and sound like speculations, but they rely on a very likely scenario based on QUIJOTE 19 GHz proprieties and the physics of the atmosphere.

In particular, the heavy right-tailed could represent the turbulent structures of the atmosphere. The high peak at 4K shows that, on average, we can identify the white noise atmospheric contribution at 19 GHz, but the heavy-tailed populations show that the atmosphere, at a higher frequency, is very complicated to model and the effects of the turbulent structures of the water vapor are significant and with these data and analysis we cannot resolve them out.

In conclusion, we can state that we can estimate the average white noise contribution of the atmosphere but there is another correlated contribution that we have to figure out.

This behavior is confirmed by the box plot of all QUIJOTE measurement frequencies, which is represented in Fig. 4.13. For the channel at 11 GHz, the scatter of the measurements is very low and increases as the frequency is getting higher. This effect could be a specific sign of water vapor fluctuations.

As we have seen by the boxplots in Fig.4.12, Fig. 4.13 and by the distributions in Fig. 4.14 we have to improve the atmospheric analysis by introducing the atmospheric turbulent structures. The only seasonal fluctuations and white noise balance do not represent a comprehensive atmospheric description but we have to assess these scatters that now can be only speculative connected to the atmospheric turbulent structures.

4.2.3 Application of CAL to the Q & U Bolometric Interferometer for Cosmology (QUBIC)

In this section, I apply CAL to the case of QUBIC, a CMB experiment that will be deployed in the Argentinean Atacama plateau at the end of 2022.

QUBIC is a very interesting experiment because he proposes a novel technical approach based on the *bolometric interferometry* (Mousset et al. 2022). During my Ph.D. thesis, I was directly involved in atmospheric forecast simulations that are summarized in the paper by Hamilton et al. (2022).

In my analysis, I used atmospheric data acquired by the QUBIC collaboration in 2015 using a small receiver feedhorn sensitive in the 150 GHz and 220 GHz bands.

The use of CAL, in this case, has been much simpler and straightforward compared to the case of Tenerife, because the Alto Chorrillos plateau is characterized by a wide area with the same weather statistics. For this reason, the spatial resolution of the weather reanalysis does not represent a concern. Fig. 4.15 represents the total quantity of water vapor (TQV) above the QUBIC site obtained from the MERRA-2 reanalysis. It is possible to appreciate that the weather is relatively stable and uniform for a wide area so I could

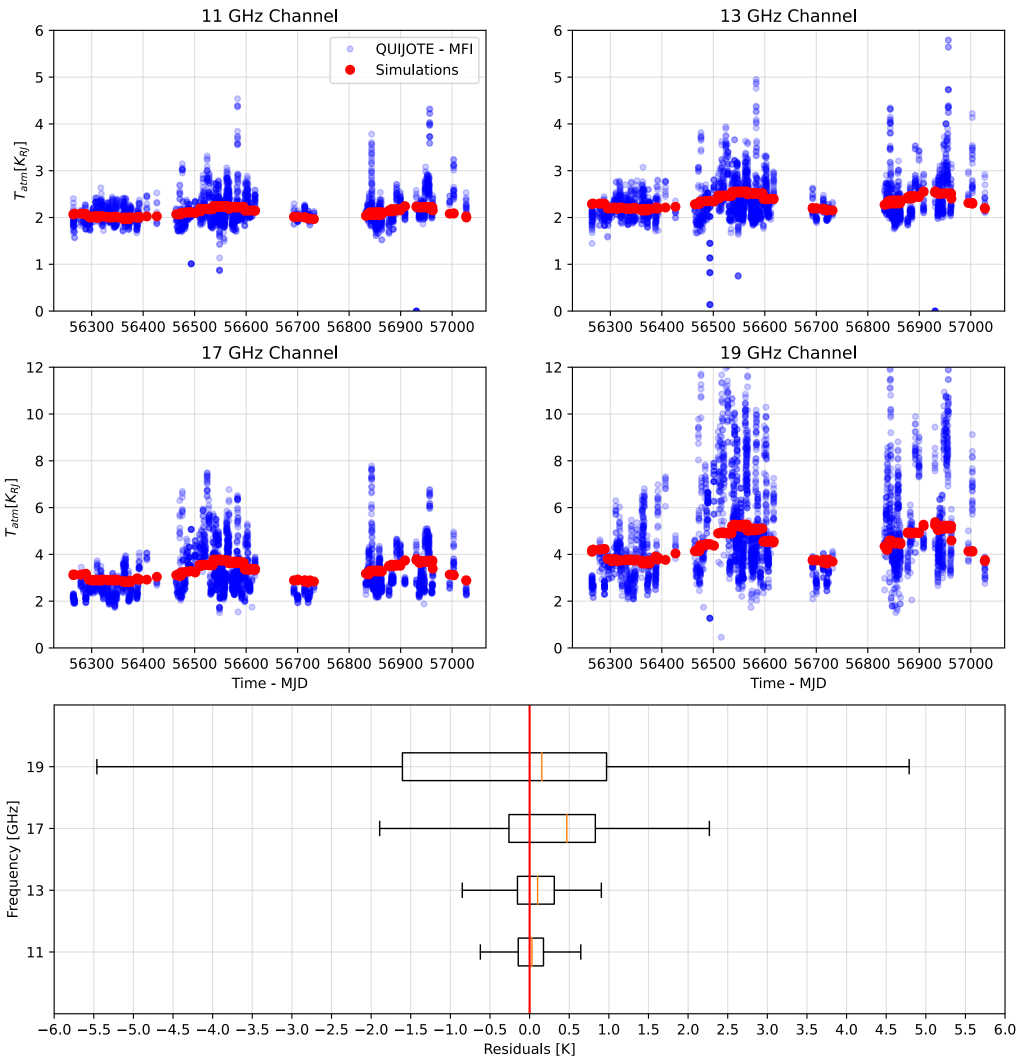

Figure 4.12: *Four panels:* atmosphere brightness temperature versus time from QUIJOTE measurements (blue points) and calibrated CAL simulations (red points). *Bottom panel:* boxplot of residuals of the differences between measurements and simulations.

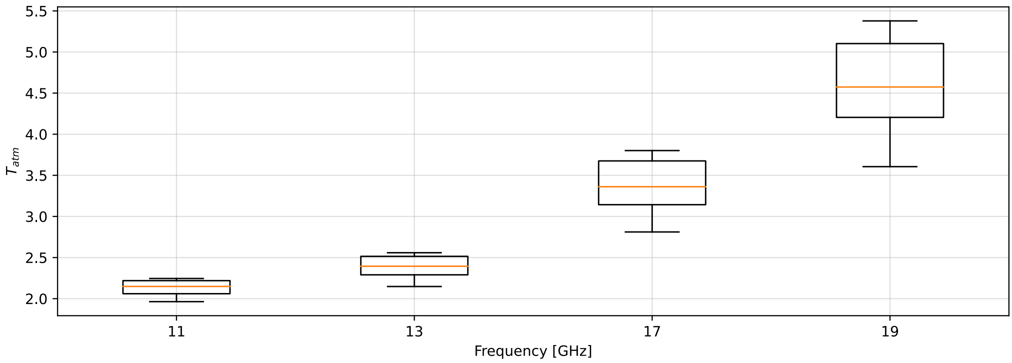

Figure 4.13: QUIJOTE channel fluctuations

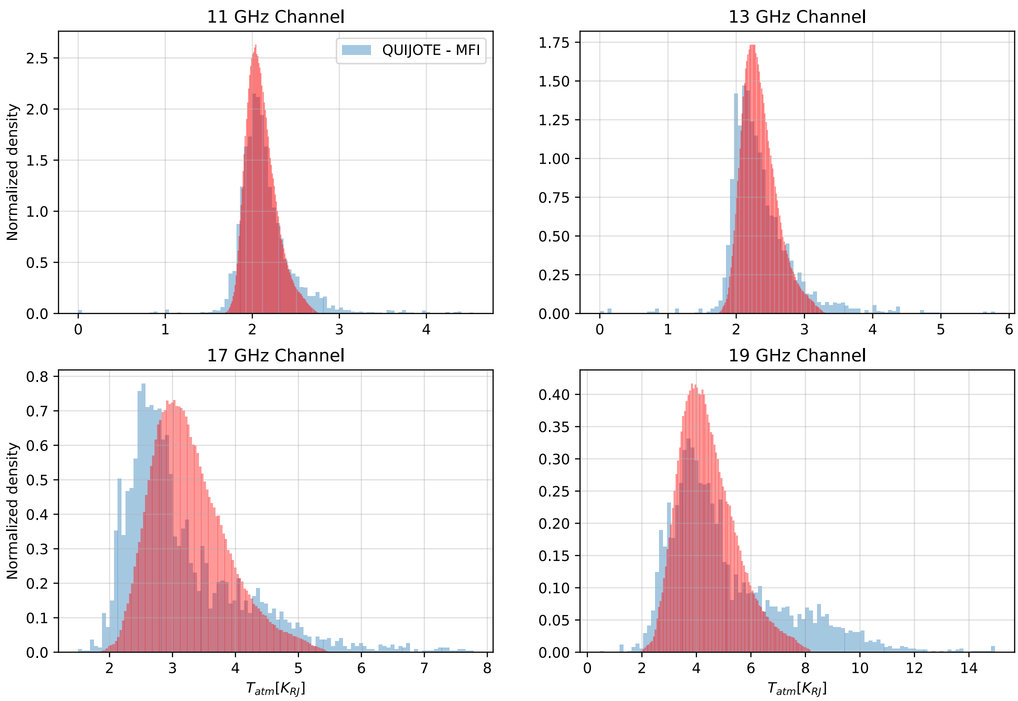

Figure 4.14: T_{atm} distribution derived from QUIJOTE-MFI measurements (in blue) and calibrated CAL simulations (in red).

use the MERRA2 data with no additional corrections.

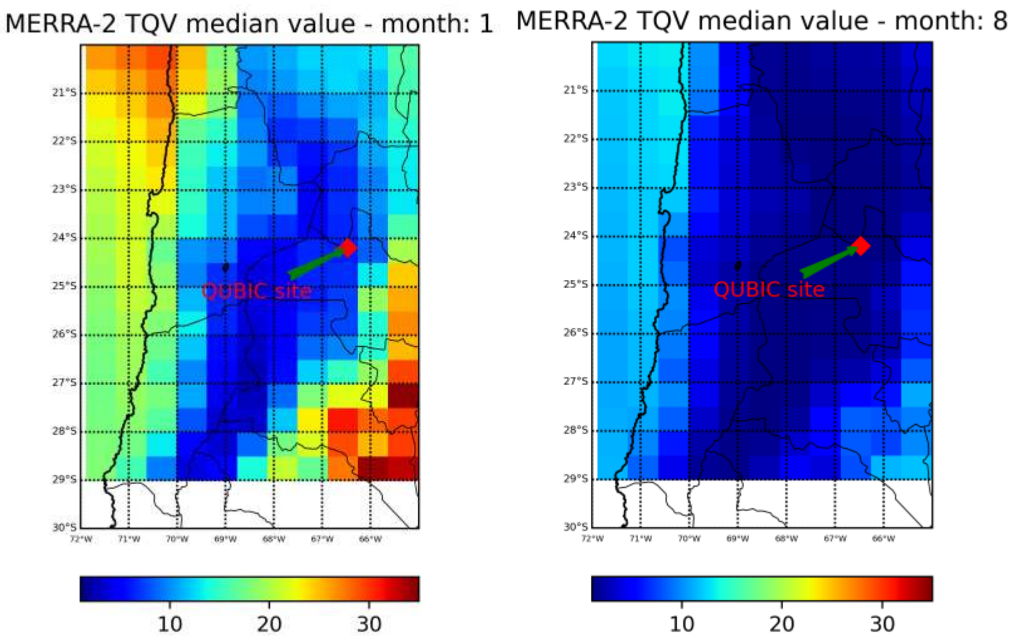

Figure 4.15: Maps of the total quantity of water vapor (TQV) above the QUBIC site for two months of the year: January (left panel) and August (right panel). Data obtained from MERRA-2 reanalysis.

Starting from the MERRA2 weather parameters CDFs, I have evaluated the atmospheric brightness temperature above the QUBIC site and assessed the level of white noise introduced by the atmosphere. The results of the simulations are shown in the left panel of Figure 4.16, while the right panel shows a direct measurement taken at the site (private letter with J.C.Hamilton).

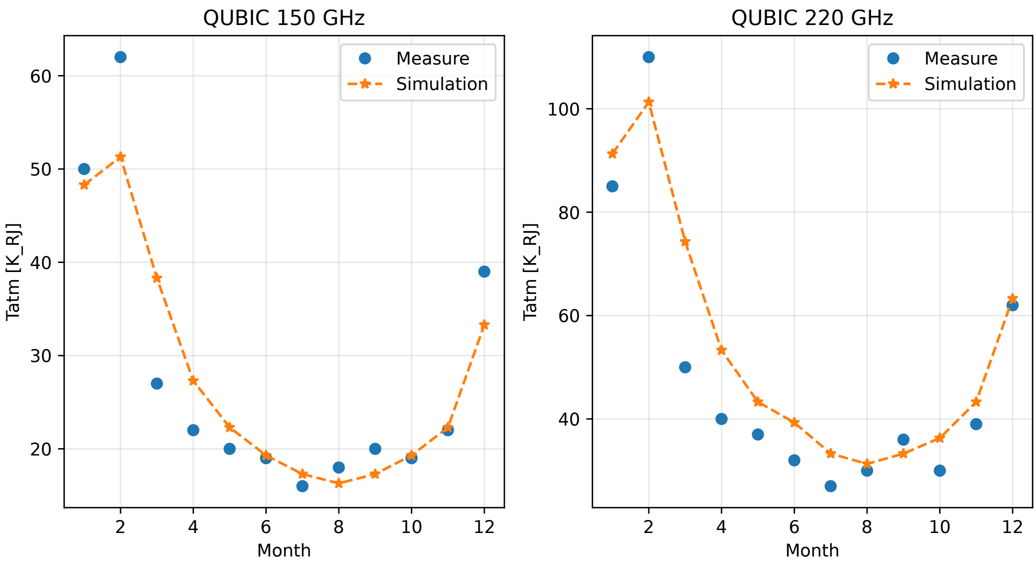

Figure 4.16: *Left Panel*: Simulated atmosphere brightness temperature for the Alto Chorrillos site using the MERRA2 CDF. Every point represents the median of 10^9 random extractions homogeneously distributed on the hours of that specific month. *Right Panel*: The atmospheric brightness temperature in K, directly measured at the QUBIC site.

Chapter 5

Turbulent Atmosphere

In this chapter, I introduce the theory of the turbulent atmospheric effects for ground-based CMB experiments and, in the next chapter, I apply it to the simulation of QUIJOTE and Strip observations.

5.1 The atmospheric antenna temperature

The atmospheric load seen by a telescope, in terms of antenna temperature, is proportional to the atmospheric absorption coefficient α, the physical temperature of the atmosphere T_{p}, the working frequency of the telescope (given in terms of wavelength λ) and by the angular response of the telescope B. Let us consider a given direction $\vec{r}_i$, at the time t, the atmospheric emission of the antenna temperature, integrated along the whole line of sight is given by:

$$T_A(\vec{r}_i, t_i) = \frac{1}{\lambda^2} \int_0^{+\infty} B(\vec{r}_i)\alpha(\vec{r}_i, t_i) T_p(z) \; d\vec{r} \tag{5.1}$$

where t is the observation time, and $\vec{r}$ is the direction of the line of sight of the telescope. The term $B(\vec{r}_i)$ is the telescope response along the line of sight $\vec{r}_i$, and $T_p(z)$ represents the vertical linear gradient temperature (it depends on the hight z).

To evaluate the eq. 5.1 we have to know the function $\alpha(\vec{r}_i, t_i)$ for each detector i and for each time, t_i. A more straightforward representation of the atmosphere is in terms of the correlation level between the antenna temperatures acquired by pairs of receivers at different times, in this way we can write an equation comprehensive of both cross-correlations between receivers and the time evolution of the correlation spurious noise for each detector.

Considering the monochromatic case, the antenna temperature $T_A(\vec{r}_i, t_i)$ depends only by λ and the correlation coefficient between two radiometers i, j is defined straightforwardly by

$$\langle T^i, T^j \rangle = \frac{1}{\lambda^4} \iint_0^{+\infty} \langle \alpha_i, \alpha_j \rangle B_i B_j T_p^i T_p^j \; d\vec{r} \, d\vec{r}'. \tag{5.2}$$

The eq. 5.2 can be analytically solved two different edge cases. The term $\langle \alpha_i, \alpha_j \rangle$ can be decomposed into two independent statistical terms

$$\langle \alpha_i, \alpha_j \rangle = \chi_1 \left(|\vec{r} - \vec{r}'| \right) \chi_2(z, z'), \tag{5.3}$$

the first term χ_1 represents the spatial distribution of the turbulent structures, while the second term χ_2 represents the magnitude of the correlations that vanishe with the altitude, accordingly with the water vapor profile.

The statistical term χ_1 is known by the works of Frisch & Kolmogorov (1995); Chernov (2017); Tatarski (2016), and the term χ_2 follows the exponential profile of the vater vapor distribution in atmosphere. The eq. 5.3 shows how the correlations between pairs of detectors are moved to the correlation between the absorption coefficients seen by them. Eventually, it means that the correlation between the antenna temperatures of pairs of detectors follows the same statistic of the correlation coeffient evaluated only on the absorption coefficients. The term χ_1 following the description of a turbulent atmosphere

$$\chi_1^{\mathrm{K}}(\Delta r) = \frac{1}{\Delta r}\int_{k_{min}}^{k^{max}} k^{-11/3}\sin(k\,\Delta r)\,k\,dk, \tag{5.4}$$

and it represents the spatial distribution of turbulent structures. The parameters k_{min} and k_{max} are defined in Fig. 5.1, and they are the inverse of the outer and inner turbulent lengths, respectively.

The term χ_2 modules the magnitude of the correlations. It is proportional to the water vapor density, and it scales exponentially with the altitude. It is an exponential decay

$$\chi_2(z,z') = \chi_2^0 \exp\left[-\frac{z+z'}{2z_0}\right]. \tag{5.5}$$

The parameter z_0 is the cut-off value of the water vapor. Fig. 4.8-panel 3 shows the water vapor vertical profile above Teide Observatory. The PWV level vanishes above 10 Km.

The time evolution of the correlation coefficient can be defined evaluating the temporal correlation function $\langle T_A(\vec{r}_i,t_i), T_A(\vec{r}_i,t_i+\tau)\rangle$. In simple cases, this equation can be integrated in order to reach a simplified model of the power spectrum density of the atmospheric fluctuations. The Fourier transform of the temporal correlation function represents the covariance matrix of this correlated spurious contribution. The description is very simple

$$\Phi(\omega) = \mathcal{F}\left[\langle T_A(\vec{r}_i,t_i), T_A(\vec{r}_i,t_i+\tau)\rangle\right], \tag{5.6}$$

and in the next section I integrate eq. 5.6 for obtaining simplified (but meaningful!) results.

5.2 A simplified case and analytical results

We cannot resolve the equation 5.6 analytically. To integrate eq.5.6 we have to do some approximations. We consider the telescope pointed at the zenith, and it is fixed. The time evolution of the noise is given by the wind, which rigidly blows the atmospheric structures.

The size of the turbulent structures of the atmosphere depends on the energy absorbed by the atmosphere. In Figure 5.1 is shown the definition of the inner and outer atmospheric lengths represented by the parameters l_0 and L_0, respectively.

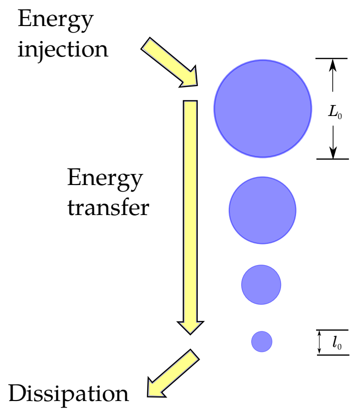

Figure 5.1: The energy balance of isotropic turbulent atmosphere and the definition of the parameters L_0 and l_0

Consider the focal plane of our imaginary telescope represented by only one detector. It is placed at the center of the focal plane. In this way, we have $i = j$ and the cross-correlation coefficient now it is a simple auto-correlation coefficient. The equation 5.2, can be rewritten as

$$\begin{aligned}\langle T_A(\vec{r})^2\rangle = \frac{2L_0^{2/3}}{\pi^2} \iint_{-\infty}^{\infty} \int_{z_1}^{z_u} \iint_{-\infty}^{\infty} \int_{z_2}^{z_u} C_\alpha^2 \left(\frac{z_1+z_2}{2}\right) b_\alpha(x_1-x_2, y_1-y_2, z_1-z_2) \times \\ \times \frac{T_p(z_1)T_p(z_2)}{w^2(z_1)w^2(z_2)} \exp\left[-\frac{2(x_1^2+y_1^2)}{w^2(z_1)}\right] \exp\left[-\frac{2(x_2^2+y_2^2)}{w^2(z_2)}\right] dx_1\, dx_2\, dy_1\, dy_2\, dz_1\, dz_2\end{aligned} \tag{5.7}$$

The coefficient $C_\alpha(z)$ represents the vertical expolential decay of the water wapor and $b_\alpha(|\vec{r}-\vec{r}'|)$ is the normalized Kolmogorov correlation function. Both the functions were defined in equation 5.4, respectiveley.

The two exp terms and w_1 and w_2 represent the spatial distribution of the beam pattern along the z axes (description given by Goldsmith (1982). The effective area of a dish pointing in the z-direction is

$$B(x,y,z) = \frac{2\lambda^2 z^2}{\pi w^2(z)} \exp\left(-\frac{2(x^2+y^2)}{w^2(z)}\right) \tag{5.8}$$

where $w(z)$ is linked to the FWHM of the beam ϕ_b by the relation

$$w_0 = \frac{\lambda\sqrt{2\log 2}}{\pi\phi_b} \tag{5.9}$$

and the beam width is given by

$$w(z) = w_0\sqrt{1+\frac{\lambda^2 z^2}{\pi w_0^4}}. \tag{5.10}$$

The eq. 5.7 can be simplified using some useful substitutions

$$
\begin{aligned}
x_1 - x_2 &= \xi_x \ ; \ x_1 + x_2 = 2X \\
y_1 - y_2 &= \xi_y \ ; \ y_1 + y_2 = 2Y \\
z_1 - z_2 &= \xi_z \ ; \ z_1 + z_2 = 2Z
\end{aligned}
\tag{5.11}
$$

and with the assumptions that $\xi_z \ll Z$ and $z_u \gg L_0$ we can consider $w^2(z_1) \sim w^2(z_2)$ and integrate on X and Y

$$
\begin{aligned}
\langle T_A(\vec{r})^2 \rangle = \frac{L_0^{2/3}}{2\pi} \int_{z_1}^{z_u} \frac{dZ}{w^2(Z)} C_\alpha^2(Z) T_p^2(Z) \cdot \\
\iiint_{-\infty}^{\infty} b_\alpha(\xi_x, \xi_y, \xi_z) \exp\left[-\frac{(\xi_x^2 + \xi_y^2)}{w^2(Z)} \right] d\xi_x \, d\xi_y \, d\xi_z .
\end{aligned}
\tag{5.12}
$$

The auto-correlation coefficient represented in equation 5.12 is easy to be read. It is composed of a first term, the integral on Z, which represents the water vapor decay, and the second integral is the convolution between the atmospheric structures b_α and the instrumental filter.

At this time it is very easy to introduce the dynamic part of the atmosphere. Let's assume that the wind blows the structures along the $x-axes$, with velocity v. We can introduce the wind effect in eq 5.12 directly in the beam filter representation.

In this way, we assume that the atmosphere is fixed and the telescope moves rigidly within the box of the atmosphere. It is weird but produces exactly the effect of the wind on the atmospheric structures. Consider the time interval $(t, \, t+\tau)$

$$
\begin{aligned}
\langle T_A(t), T_A(t+\tau) \rangle = \frac{L_0^{2/3}}{2\pi} \int_{z_1}^{z_u} \frac{dZ}{w^2(Z)} C_\alpha^2(Z) T_p^2(Z) \cdot \\
\iiint_{-\infty}^{\infty} b_\alpha(\xi_x, \xi_y, \xi_z) \exp\left[-\frac{(\xi_x + v\tau)^2 + \xi_y^2}{w^2(Z)} \right] d\xi_x \, d\xi_y \, d\xi_z
\end{aligned}
\tag{5.13}
$$

the power spectrum of the autocorrelation function is given by

$$
\begin{aligned}
\mathcal{F}\left[\langle T_A(t), T_A(t+\tau) \rangle \right](\omega) = \frac{1}{2\pi\sqrt{2}} \frac{L_0^{2/3}}{v} \int_{z_1}^{z_2} \frac{dZ}{w(Z)} C_\alpha^2(Z) T_p^2(Z) \exp\left[-\frac{w^2(Z)\omega}{4v^2} \right] \\
\iiint_{-\infty}^{\infty} \exp\left[\frac{i\xi_x \omega}{v} \right] \exp\left[-\frac{\xi_y^2}{w^2(Z)} \right] b_\alpha(\xi_x, \xi_y, \xi_z) \, d\xi_x \, d\xi_y \, d\xi_z
\end{aligned}
\tag{5.14}
$$

The eq. 5.14 can be integrated in two different conditions: $w(Z) \gg L_0$ and for $w(Z) \ll L_0$. The integration of these two cases is known as *atmospheric two-slopes model* and in the next section, we discuss the result of the integrations.

5.3 The two-slopes model: for high and low atmosphere

We can analytically evaluate the equation 5.6 only in two different regimes. The power spectrum can be factorized in two different terms

$$
S(\omega/v) = \Phi(\omega/v) \times I(\omega/v)
\tag{5.15}
$$

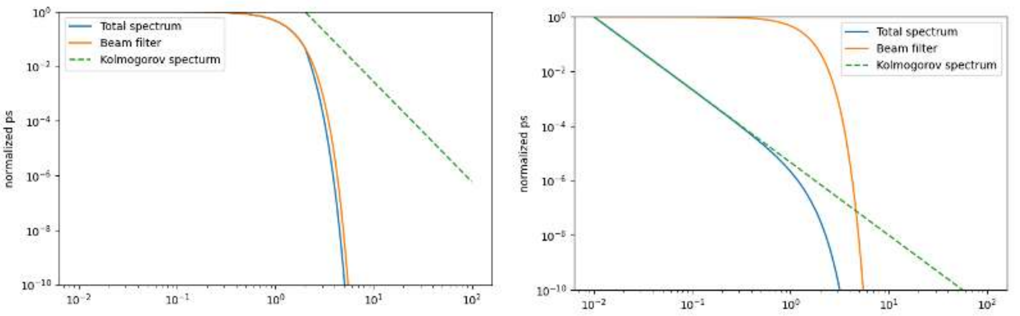

Figure 5.2: The figure shows the two components of the Fourier transform presented in equation 5.15. The left panel shows the case for the low-atmosphere case and the high-atmosphere case. The beam filter is the same in both panels because the instrument remains the same, but the Φ component changes. In the first case, the TOD is dominated by the beam filters, while in the second case the spectrum is dominated by the atmospheric noise.

where $\Phi(\omega)$ represents the temporal power spectrum due to the motion of the atmosphere in front of the telescope, and $I(\omega/v)$ represents the beam filter.

In the condition of $w(Z) > L_0$ we are taking into account the high-altitude atmosphere layers. The exponential in ξ_y changes slowly compared to b_α and we the atmospheric power spectrum can be integrated and the result is given by

$$\Phi(\omega) = \begin{cases} (\omega/v)^{-11/3} & 1/L_0 \ll \omega/v \ll 1/l_0 \\ \text{const.} & \omega/v \ll 1/L_0 \end{cases}, \tag{5.16}$$

while for $w(Z) < L_0$, this condition represents the low atmosphere layers. The integration of the power spectra gives

$$\Phi(\omega) = \begin{cases} (\omega/v)^{-8/3} & 1/L_0 \ll \omega/v \ll 1/l_0 \\ \text{const.} & \omega/v \ll 1/L_0 \end{cases}. \tag{5.17}$$

These results show that we cannot define an atmospheric noise covariance matrix using a noise prior with a defined slope and knee frequency. In this case, the slope is different and it depends on the altitude of the atmospheric layer that we are taken into account. For this reason, a more effective way to simulate the atmospheric load on the detector is to create a box of atmosphere around the telescope and feed it with the typical turbulent atmospheric structures.

Even if the atmospheric TODs power spectrum cannot be analytically evaluated, the stochastic spatial structures of the atmosphere are well described by the literature cited above.

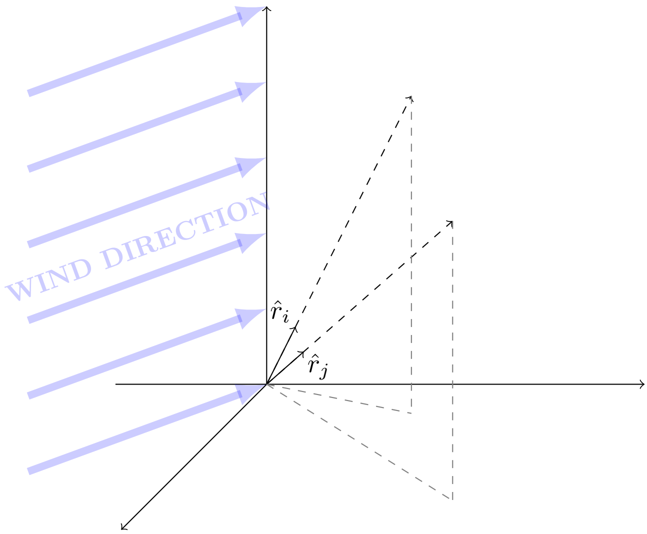

Figure 5.3: The lines of sigth of two different detectors. In blue is represented the wind direction

5.4 Simulation of the telescope observations

The telescope observation process was simulated with *Cmb Atmospheric Library* - CAL written by Mandelli et al. (2021) and strongly based on TOAST framework by Kisner et al. (2020). Starting from the Strip weather file, I have created a full focal plane simulation of Strip observation, updating the atmosphere condition every hour.

In function of the simulated hour and month, the atmosphere is generated with initial input given by the CDF weight of the weather parameters. Next, I simulate a modulated scan at constant elevation as represented by Figure 5.4.

The atmospheric realization is loaded in RAM into a compressed form. The water vapor structures that are visible in Figure 5.4 are blown by the wind and past the line of sight of the telescope. The atmospheric temperature is evaluated directly by the integral in eq. 5.1. The integration boundaries are represented by the sum of every small contribution given by the cells that are intercepted by the receiver's line of sight.

Comparison test with POLARBEAR

Unlike a satellite where the cross-correlation matrix can be treated as a matrix whose off-diagonal terms are small, the off-diagonal terms are essential and strictly related to the scanning strategy and wind velocity and direction.

Figure 5.5 shows the autocorrelation coefficient of the central detector of the POLARBEAR focal plane. To check the code, I reproduce the result obtained by Errard et al. (2015) analyzing the POLARBEAR data.

I realized the same atmospheric condition during the data taken process. I plotted the eq. 5.2 for $i = j =$*central detector* and we obtain the same pattern of the measured auto-correlation.

The good agreement between the plots in Fig. 5.5 ensures that we can use this code, with an appropriate weather file (constructed using the guide-line given in chap. 4 for a given observation site), to predict the fluctuations level of the antenna temperature directly in the TOD acquired by the receivers.

The plots in Figure 5.5 show the complexity of the atmospheric simulation. In the previous section, we derived the *two-slopes* power spectrum analytically using rigid approximations. In the exercise of Fig. 5.5, we also include the movements of the telescope with its scanning strategy, which results in the TODs being a convoluted effect of all these factors: scanning strategy, atmospheric emission, and the wind-driven dynamics of the atmosphere.

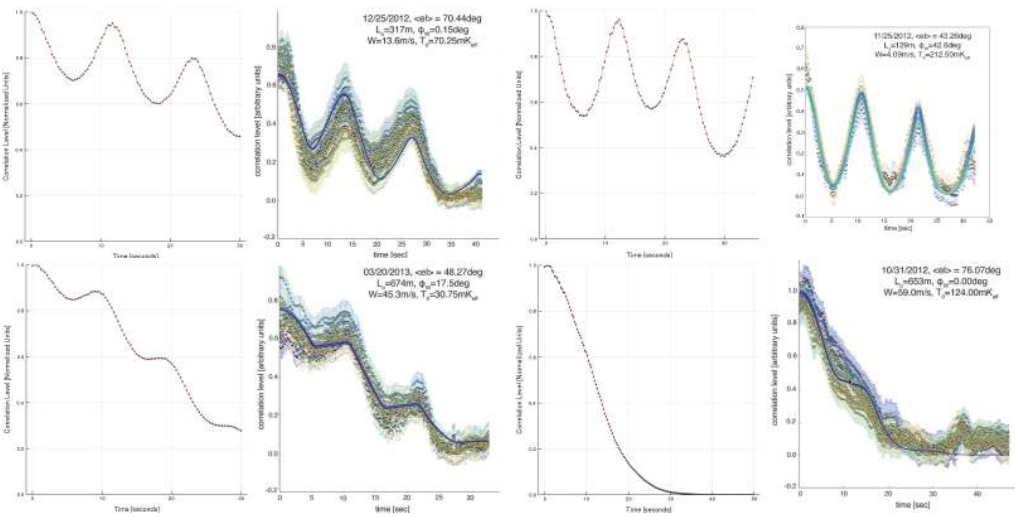

Figure 5.5: This figure shows four different comparisons between the atmospheric simulation code and the comparison with POLARBEAR Errard et al. (2015) measurements. I have simulated the same atmosphere, with the same weather parameters, and I have compared the simulated auto-correlation coefficient of the central detector.

5.5 QUIJOTE fluctuations

From the previous section, we have seen that we can reconstruct the autocorrelation coefficient pattern of the central detector of the POLARBEAR telescope with a reasonable degree of compatibility. Now, we construct a possible TOD acquired by QUIJOTE - MFI and compare the scatter of the atmospheric temperatures with the measured ones. The target is to explain the large scatter, seen in the 19 GHz channel introducing the turbulent effects of the atmosphere.

Using the atmospheric statistical picture constructed in the previous chapter, we conditioned CAL to recreate a TOD of a possible QUIJOTE detector at 11 GHz and 19 GHz. Due to limited time and computational resources, I constructed a TOD of a representative

QUIJOTE detector of about 24 hours, in two different seasons (winter and summer) and built the distribution of the antenna temperature scatter from the zero-average.

In Fig. 5.6, and Fig. 5.7, I present four different 24-h TOD acquired by the 11 GHz channel in winter and summer time,

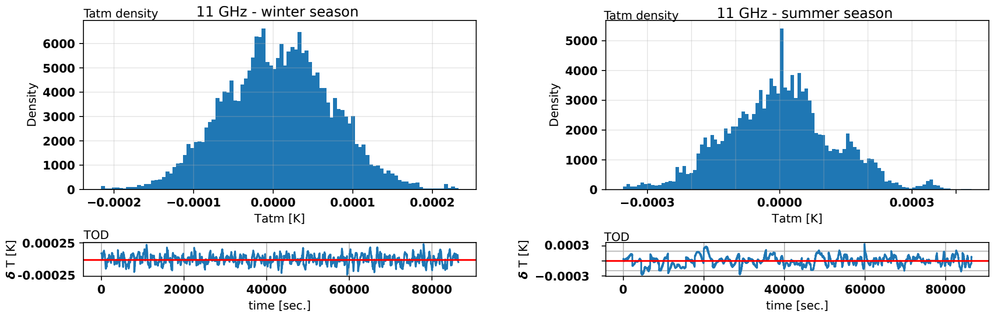

Figure 5.6: Atmospheric antenna temperature fluctuation simulated for a representative QUIJOTE detector at 11 GHz during winter and summer time. The top panel represents the fluctuation distribution density histogram, the bottom panel represents the 24-hour timestream

and the same for the 19 GHz channel.

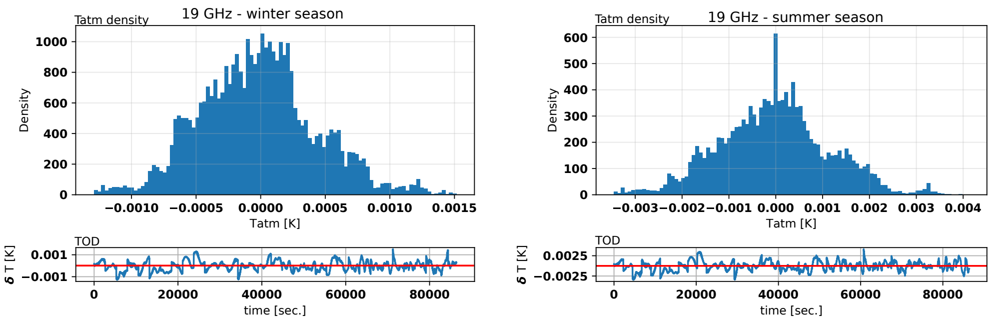

Figure 5.7: Atmospheric antenna temperature fluctuation simulated for a representative QUIJOTE detector at 19 GHz during a representative day in winter and summer seasons. The top panel represents the the fluctuation distribution density histogram, the bottom panel represents the 24-hour timestream

Although the Tatm-scatter increases by moving from winter to summer season and increasing the frequency, we do not reach the scatter levels seen in the QUIJOTE-MFI data. The peak-to-peak scatters are of the order of

From private communications with J. A. Rubino-Martin and R.T.G. Santos (the PIs of QUIJOTE), we have been able to ascertain that the level of small-time fluctuations (of the order of 24h) due to the atmospheric contribution is compatible with the latest TOD reconstructions. Thus, we have a PtP atmospheric fluctuations, for the worst case,

Table 5.1: Peak-to-Peak values of the atmospheric antenna temperature fluctuations simulated and presented in Fig. 5.6, and Fig. 5.7

Freq. [GHz]	Season	Peak-to-Peak [μK]
11	winter	450
11	summer	670
19	winter	2500
19	summer	6800

of the order of 6800μK for the channel most sensitive to water vapor (19 GHz) during the season most affected by atmospheric emission, i.e., the summer months in the Northern Hemisphere.

The same exercise can be extended to the Strip frequency using the instrument focal plane in order to predict the level of atmospheric antenna temperature fluctuations for the 43 GHz and 95 GHz channels.

5.6 Strip fluctuations

I used the Strip instrumental database[1] to extract the information of the Strip focal plane. Fig. 5.8 shows the sky projection of the receivers. The 43 GHz receivers are divided into hexagons identified by the letters: I (central), R, O, Y, G, B, and V. The 95 GHz receivers are identified by the letter W and are located at the edges of the internal hexagon. The red line identifies the polarization angle of each detector.

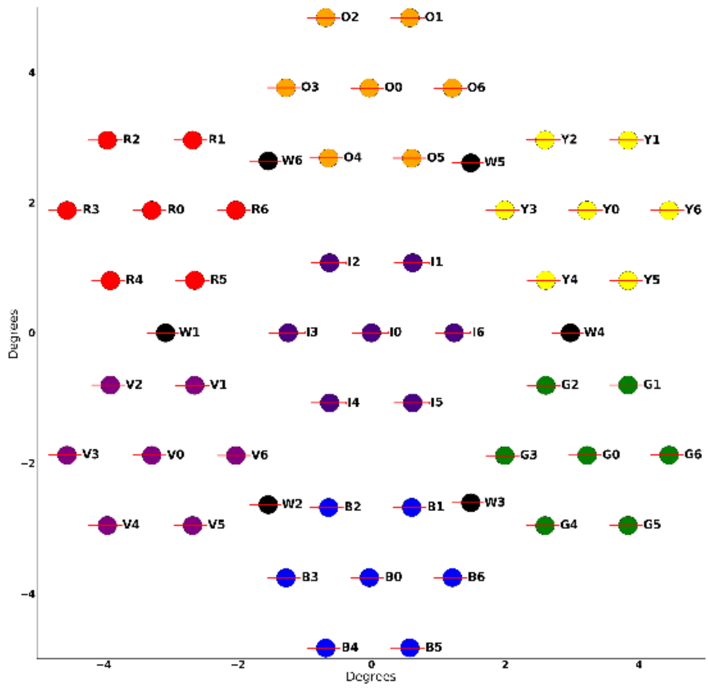

Figure 5.8: Strip focal plane: with the capitol letter I, R, O, Y, G, B are identified the 43 GHz receivers. The capital letter W, identifies the 95 GHz receivers.

Following the same simulation performed in the previous section, I extended the exercise to the Strip frequencies, evaluated in the winter and summer seasons. The results are presented in Fig. 5.9 and Fig. 5.10. As expected, compared with the QUIJOTE channel, the strip receivers are characterized by a higher scatter of the antenna temperature due to atmospheric emission.

[1] `https://github.com/lspestrip/Stripeline.jl/tree/master/instrumentdb`

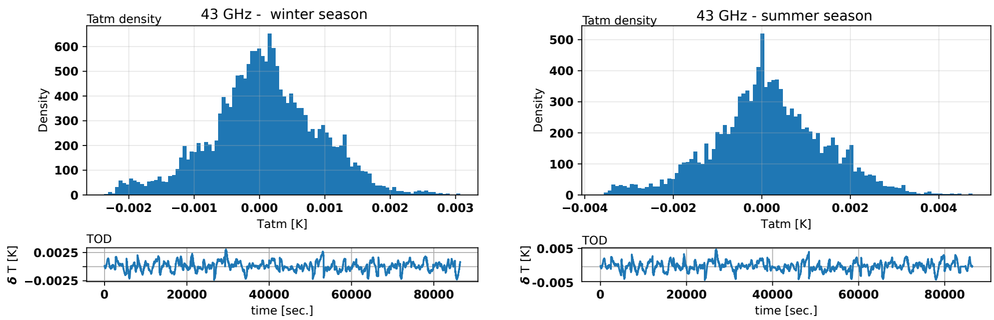

Figure 5.9: Atmospheric antenna temperature fluctuation simulated for a representative Strip detector at 43 GHz during winter and summer time. The top panel represents the fluctuation distribution density histogram, the bottom panel represents the 24-hour timestream

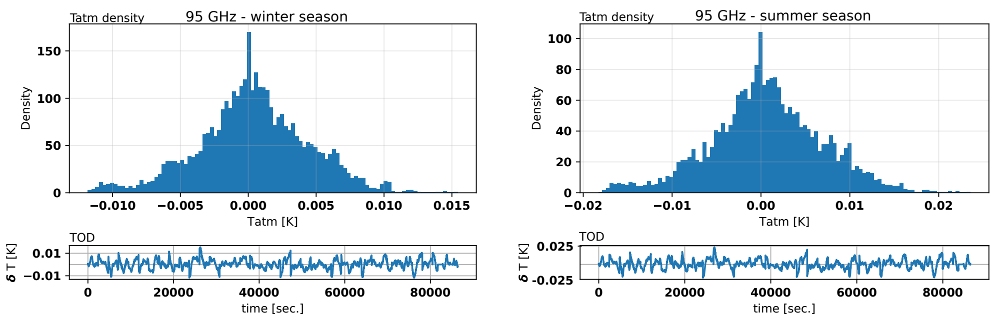

Figure 5.10: Atmospheric antenna temperature fluctuation simulated for a representative Strip detector at 95 GHz during winter and summer time. The top panel represents the fluctuation distribution density histogram, the bottom panel represents the 24-hour timestream

Table 5.2: Peak-to-Peak values of the atmospheric antenna temperature fluctuations simulated and presented in Fig. 5.9, and Fig. 5.10

Freq. [GHz]	Season	Peak-to-Peak [μK]	Expected PtP in Pol. [μK]
43	winter	5500	55
43	summer	10000	100
95	winter	25000	250
95	summer	50000	500

In Tab. 5.2 are reported the peak-to-peak level for each channel in different seasons. These numbers are evaluated in total intensity. As described in chap.3, the Strip radiometers are sensitive only to polarized signals and the contribution of the instrumental leakage from total intensity to polarized channel is of the order of 1%. In conclusion, the expected fluctuations in the Strip polarized channel will be of the order of 1% of that simulated for I Stokes' parameter.

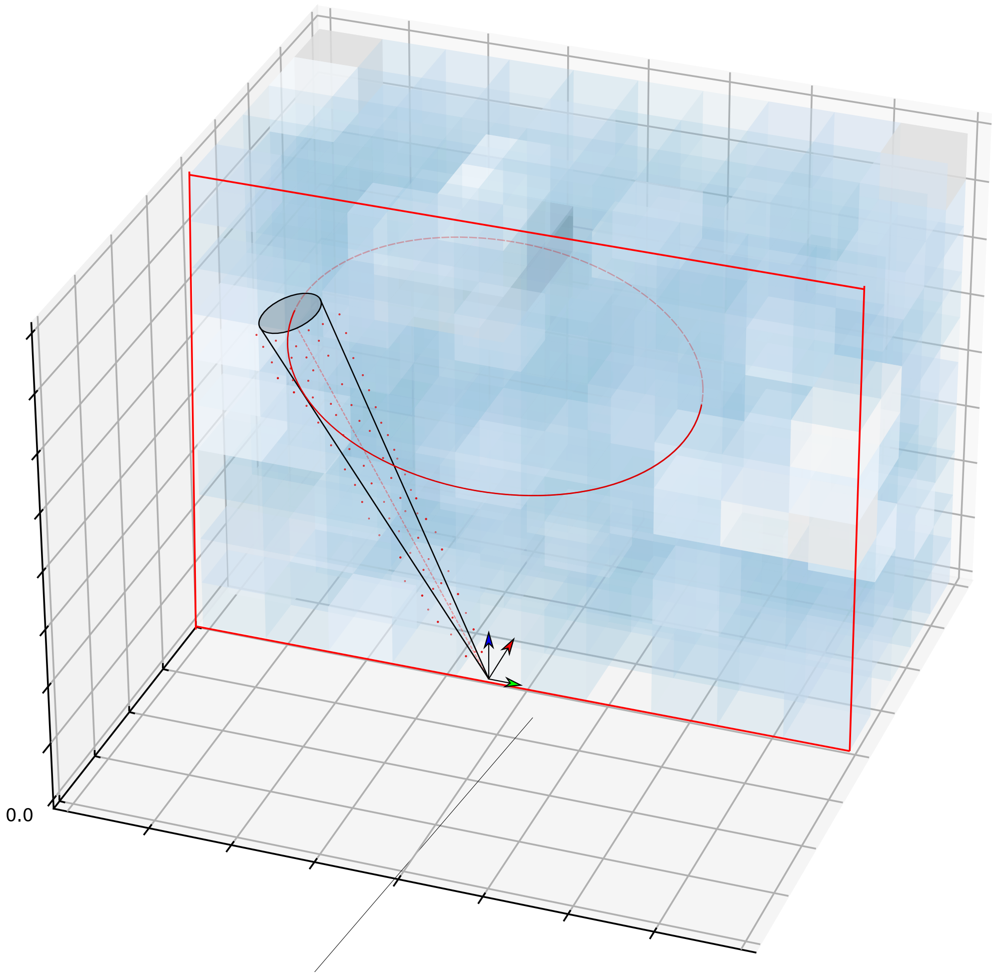

Figure 5.4: The figure shows a vertical cut of the atmosphere. The color of the cells represents their contribution dT_A evaluated at that specific point. The cells are correlated with the Kolmogorov spatial power spectrum. The cone represents the observation cone of the detector that scans the sky with a spinning scanning strategy.

Chapter 6

Simulation results

In chapters four and five, I described an approach based on reanalysis data and actual measurements to obtain the statistical weather picture of a particular geographical site with high time and spatial resolution. Two main components characterize this approach: the first is represented by the CDFs collection of the weather parameters of interest, and the second is represented by the calibration coefficient k_ν.

Subsequently, I compared the simulated data with the QUIJOTE - MFI measurements obtaining an excellent agreement that is shown in Fig 4.12.

With these two pieces of information, we are able to evaluate the statistical picture of the atmospheric quality at the LSPE/Strip site. We extrapolate, from Fig.4.10, the calibration coefficient k_ν for the LSPE/Strip telescope frequencies, and we evaluate the white noise contribute, in terms of T^A_{atm}, due to the atmospheric emission.

In this work, we do not consider the complete frequency band response of the detectors, but it was done monochromatically.

6.1 LSPE/Strip Q-channel and W-channel

The focal plane of the LSPE/Strip telescope is composed of 49 polarimeters at 43 GHz and 6 polarimeters at 95 GHz. We have extrapolated the calibration coefficient for these frequencies, and the values are reported in Tab. 6.1. With CAL, we repeat the same

Table 6.1: Calibration coefficient for LSPE/Strip focal plane

	Frequency	k_ν
Q-band	43 GHz	0.590
W-band	95 GHz	0.329

Monte Carlo process done for QUIJOTE data. We have extracted 10^3 samples per hour for each month and evaluated the median. The results are reported in Fig. 6.1.

A lower frequency characterizes the Q-channel compared to the W-channel, but in spite of this, the simulations show a higher median T_{atm} for the Q-channel with small daily fluctuations. The W-band channel is characterized by a lower median T_{atm}, but its seasonal and daily median fluctuations are higher compared with the Q-band channel.

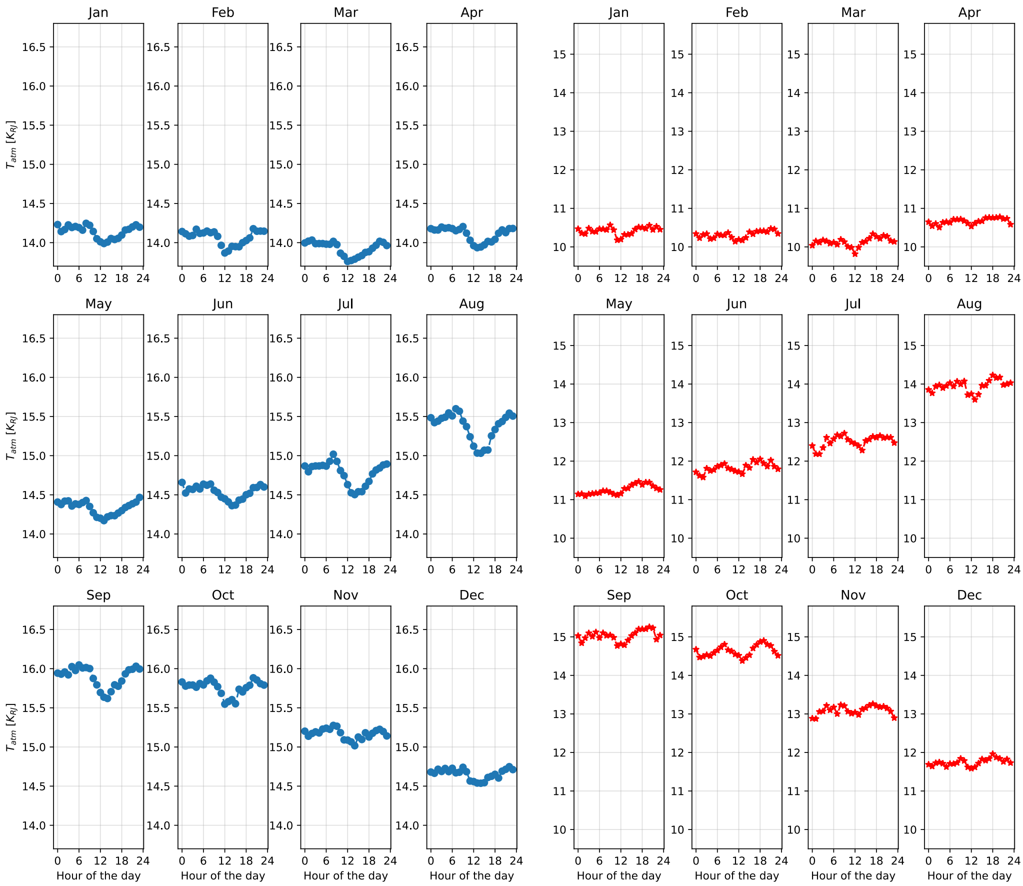

Figure 6.1: *Left Panel:* Daily fluctuation of the brightness temperature at 43GHz. *Right Panel:* Daily fluctuation of the brightness temoperature at 95GHz. In both panels are every points is the median of one billion of atmospheric realizzation. Each box represents a month and its daily fluctuation of a the atmospheric brightness temperature. The scale is the same for every box at same frequency. In this way it is possible to appreciate that during the summer time the temperature grows up increasing the white nose balance. The cleaner sky are characterized by the winter season when the PWV concentration is at its minimum.

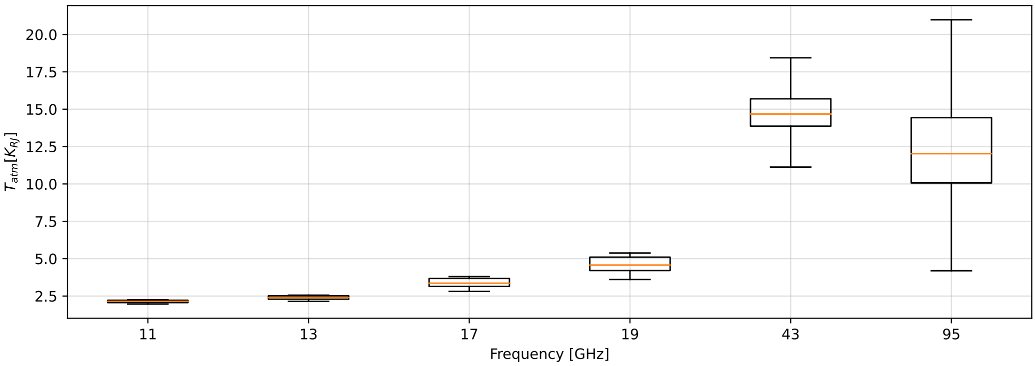

Figure 6.2: This figure shows the comparison between the fluctuation of the atmospheric brightness temperatur for the QUIJOTE frequencies (11, 13, 17, 19)GHz and for LSPE/Strip (43, 95) GHz. The scatter is higher for higher frequency but the median is lower at 95GHz because at this frequency the atmospheric brightness temperature is dominated by the water vapor that it is characterized by a wide range of scatter. The atmospheric signal at 43 GHz is dominated by the Oxygen line that produce less scatter but in median higher brightness temperarures.

In Fig. 6.2 is shown a comparison between the boxplots built with the whole set of atmospheric realizations, for the frequency of QUIJOTE telescope and, in addiction the LSPE/Strip frequencies. The orange line represents the median of the samples. At higher frequencies, the scatter of the sample get higher.

The median of the samples at 95 GHz is lower compared to that at 43 GHz, but the scatter between the min/max of the samples is extremely large for the 95 GHz channel. The atmospheric brightness temperature at 43 GHz is always lower than 20 K whithinthe 95% CL. The atmospheric brightness temperature at 95 GHz presents some samples greater than 20 K in the same 95% CL.

We can conclude that the median of the atmospheric temperature is lower for the W channel because the Pico del Teide site, in median, presents an excellent and dry atmosphere, and the O_2 dominates the atmospheric emission. Fig. 6.3 shows that the dyoxygen emission affects the Q-band channel primarily compared with the W-band channel in the dry atmosphere regime. In the same way, small fluctuations of the water vapor can produce a significant fluctuation of the atmospheric temperature at 95 GHz with oscillation of amplitude of the order of 15 K.

6.2 Mapmaking and atmospheric cleaning

Figure 3.10 shows that the spurious atmospheric signal will be present in the polarized channel only as residual leakage. The 1% of the intensity signal will be leaked into the polarized channels quite at the same level.

Despite this first mitigation performed by the polarimeter structure, the spurious

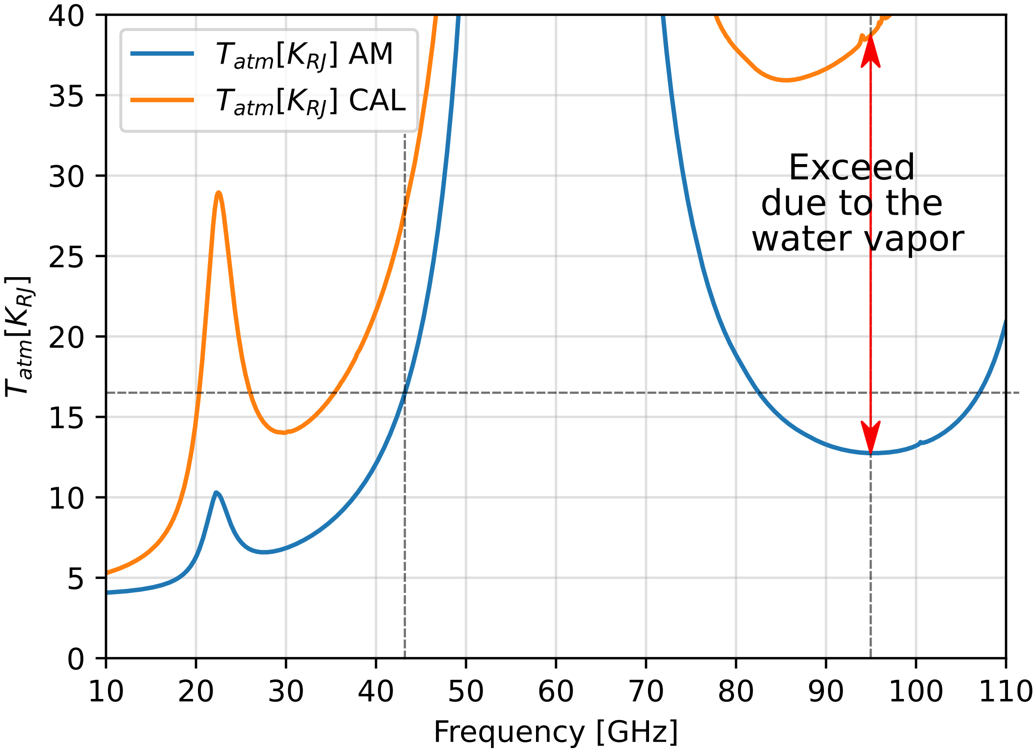

Figure 6.3: This figure shows how the atmospheric brigthness temperarure changes in function of the water vapor. The T_{atm} at 43 GHz oscillates between 16K and 27K while at 95 GHz between 13K and 38K. In dry condition, the atmosphere emission is low at 95GHz but it more susceptibility to the changes in water vapor. This plot explain the Figure 7.2 in particular why the median is lower at 95GHz instead at 43GHz. Moreover it explains the larger bars at 95GHz compared to 43GHz.

signal remains significant.

The maps that are shown in Figure 6.4 represent the binning map of January and the difference between the sky input.

Since the atmospheric signal is not polarized and what I expect to find in the polarized channels is, in addition to the scientific signal, the intensity channel for the leakage coefficient, my analysis was focused on looking for the typical atmospheric signature in the intensity channel. In the bottom panel of Figure 6.4 is shown the residual (binned maps - input sky) maps, and it shows the atmospheric contribution in the intensity channel. Only 1% of this signal will be leaked into the polarization channels.

6.3 Consideration about mapmaking limitations

The starting point of the mapmaking is the calibrated time ordered data recorded by the recievers. We collect all these time samples in a vector $\vec{d}$ which contains $\mathcal{N}$ elements.

The entire data vector can be represented in a compact way as,

$$\vec{d} = \mathbf{A}\vec{s} + \vec{n}. \tag{6.1}$$

The vector $\vec{n}$ represents the noise that we considered characterized by the covariance matrix $\mathcal{C}_n$. The pointing-matrix $\mathbf{A}$ is a know matrix (the output of the pointing model reconstruction, presented in Chapeter 3), and $\vec{s}$ is a time-domain signature, telling us when a given sky pixel was observed and with what weight it contributed to the measured signal.

To build up a sky-maps from the data vector $\vec{d}$ we use the map-making, that can be formalized with a linear problem. We can use a generalised last square (GLS) method, that provides the following estimator of the signal vector

$$\hat{s} = (\mathbf{A}^T\mathbf{M}\mathbf{A})^{-1}\mathbf{A}^T\mathbf{M}\vec{d} \tag{6.2}$$

for anny choice of positive define weight matrix $\mathbf{M}$.

We want to reconstruct the sky map. It is unknown and we can call it $\vec{x}$ that has to satisfy

$$\mathbf{B}\vec{x} = \vec{b} \tag{6.3}$$

where $\mathbf{B} = (\mathbf{A}^T\mathbf{M}\mathbf{A})^{-1}$ and $\vec{b} = \mathbf{A}^T\mathbf{M}\,\vec{d}$.

The equation of the map-maker 6.3, can be solved with explicit method, but it require the explicit knowlegde of $\mathbf{B}$.

The problem can be resolved with an iterative method like the preconditioned conjugate gradient (PCG). If $\mathbf{B}$ is symmetric and positive definite, it can be used to define a scalar product iin the vector space. The component of the solution along a normalized vector $\vec{p}$ is equal to

$$\vec{p}^T\mathbf{B}\vec{x} = \vec{p}^T\vec{b}, \tag{6.4}$$

thus computable without actually having $\vec{x}$.

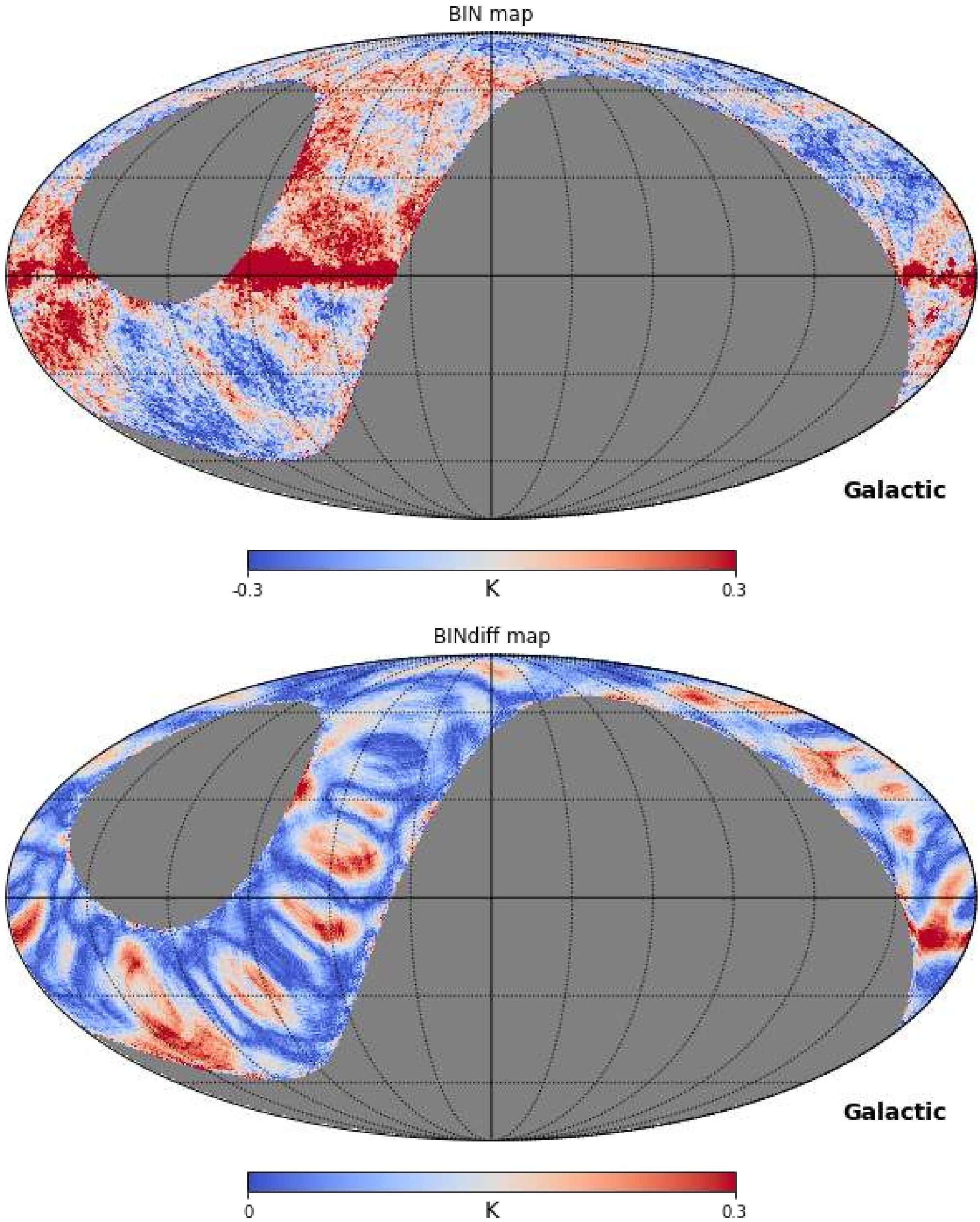

Figure 6.4: Intensity maps. The top panel represent the binned maps while the bottom panel is the residual maps (I subtracted the sky-input) in order to enlight the intensity of the atmospheric fluctuations in intensity maps

The iterative process finds the projection of the solution over the space spanned by a growing set of orthonormal vectors. The first basis vector is typically $\vec{p}_0 = \vec{b}/\sqrt{\vec{b}^T\mathbf{B}\vec{b}}$, the approximate solution is thus $\vec{x}_0 = (\vec{p}_0^T\vec{b})\vec{p}_0$. The next dimension of the basis is chosen to be $\vec{r}_0 = \vec{b} - \mathbf{B}\vec{x}_0$, and $\vec{p}_1$ is defined by removing the component of $\mathbf{r}_0$ along the previous basis vector and normalizing the result. It is not ensured that $\vec{p}_1$ actually exist since $\vec{r}_0$ could be proportional to $\vec{p}_0$. Assuming it is not the case, the solution can now be refined as $\vec{x}_1 = (\vec{p}_0^T\vec{b})\vec{p}_0 + (\vec{p}_1^T\vec{b})\vec{p}_1$. The process continues analogously by choosing as next dimension $\vec{r}_i = \vec{b} - \mathbf{B}\vec{x}_i$. The iterations are stopped either after some predefined number of iterations or when a convergence criterion is reach, e.g. $|\vec{r}_i|^2$ is lower than a fixed threshold.

The convergence is not ensure, in particular for $\mathbf{B}$ matrix particularly problematic. It is exactly the case of the ground-based TODs.

The $\mathbf{B}$ matrix contains that part of unknown noise-covariance-matrix given by the atmosphere. It is charcaterized by a strong level of correlation between detectors and the now we are working to resolve this problem.

6.3.1 Possible solutions

To manage the map-making problem, we have to find a way to recognized the atmospheric signal from what is not atmosphere. We know that the Strip focalplane is characterized by a significant leakage from $I \to Q$ and small leakage from $I \to U$ with the reference to the focal plane.

As shown in Figure 6.5 When we move on the polarized time stream $\vec{d_p}$ we use che continuous changing of the polarization angle of the receivers as a function of the Azimuth angle.

The polarized time-stream can be written as

$$d_p(t) = \cos(2\varphi(t))Q_p(t) + \sin(2\varphi(t))U_p(t) + n_t \tag{6.5}$$

where the n_t is the noise, Q and U are the Stokes parameters of the incoming light for the sky pixel p being observed at the time t, and $\varphi(t)$ is the polarization angles projected into the sky.

Since the instrumental leakage from $I \to U$ and $I \to Q$ is strongly unbalanced and it is quite negligible in U but it is amounts at $\sim 1\%$ in Q, and since the atmosphere is quite unpolarized, the $Q_p(t)$ and $U_p(t)$ signals are correlated to $\varphi(t)$ that it is directly linked to the AZ angles.

The continuos spinning scanning strategy create a continuos modulation of the polarization angle $\varphi(t)$ that, it will be sufficiently strong, it can be used to identify the spurious atmospheric contributions and elaborate some mitigation technique in order to get rid of it.

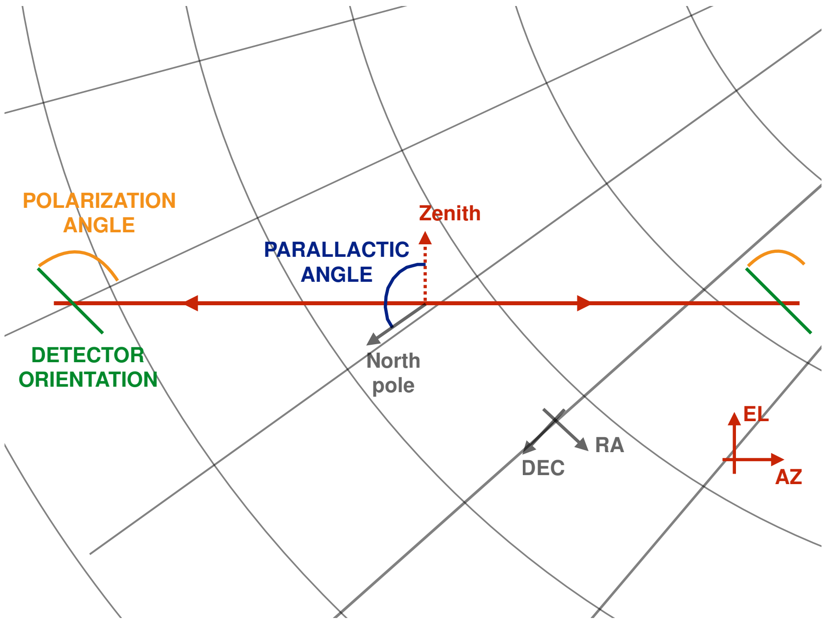

Figure 6.5: Graphical representation of the rotation of the polarization angle of the recievers. Since the telescope scans the sky with a spin rotation at constant elevation, the orientation of the Q/U frame with the reference of the focal plane rotates with respect to the frame of the sky.

Chapter 7

Conclusions

In chap.4, we saw how it was possible to create a *weather-file* from reanalysis data such as MERRA-2 (in the case of QUBIC, which is located at an observational site characterized by a sizeable spatial homogeneity). The ERA-5 reanalysis permits to create a weather files with an higher spatial resolution and it is particularly indicated for characterizing sites located on small islands. In general ERA-5 can be used where weather conditions are not homogeneous on a large spatial scale but are concentrated only in a minimal area around the observational site.

Despite the higher spatial resolution of ERA-5, we have seen that it is still insufficient to describe the atmosphere's statistics above the Teide observatory site. In this context, I used the atmosphere temperatures taken from QUIJOTE-MFI and compared them with those obtained with LibAATM.

As we can see in Fig.4.6 the statistical representation of the atmosphere above Teide observatory overestimates T_{atm} acquired by QUIJOTE-MFI. It is due to an overestimation of the water vapor mixed in the atmosphere. Therefore, I used the atmosphere vertical profiles acquired directly from the Teide observatory to correct the percentage of water vapor in the atmosphere evaluated from ERA-5 reanalysis, defining the water vapor correction coefficient k_μ that depends on the frequency.

Correcting the antenna temperatures calculated with libAATM, we found the same statistics followed by the atmosphere temperatures of QUIJOTE-MFI with an incompatibility on the 19 GHz. This channel shows a large scatter of temperatures not identifiable, at first glance and in the absence of housekeeping data, with instrumental or environmental systematics.

To explain this wide scatter of the 19 GHz channel, I simulated the scatter expected in the winter and summer TOD from the correlated structures of the atmosphere. In chap.6, I performed this analysis, arriving at a scatter level much lower than that visible in QUIJOTE MFI's T_{atm} measurements. From private correspondences with J.A. Rubino-Martin and R.T.G. Santos, we ascertained that in a short TOD of 24 hours, such as the one simulated, the order of magnitude of the fluctuations in the various channels is compatible with that observed. In this way, we can say that the scatter given by the turbulent fluctuations of the atmosphere is present and has an order of magnitude like the one calculated in Tab.5.1. In contrast, the scatter of the intensity, visible in the T_{atm} measured by QUIJOTE and plotted in the Fig. 4.6 cannot have been created by the turbulent structures of the atmosphere but by an environmental variable that could not be kept under control.

Based on the result obtained for QUIJOTE-MFI, we estimated the possible antenna temperature fluctuations due to atmospheric emission in the 43 GHz and 95 GHz of Strip channels. The architecture of Strip's radiometers is only sensitive to polarised signals, so knowing the leakage from total intensity to polarised channels, we estimated the atmospheric temperature fluctuations scatter in the summer and winter months. The results are reported in Tab. 5.2 and for the polarization channel, the fluctuations are strongly mitigated.

Future perspectives

In this thesis, we did not take into account the mapmaking algorithm for reconstructing the intensity and polarized maps. The well-known mapmaker algorithm like MADAM can not be used for mitigating the atmospheric spurious correlations. A possible way to mitigate the atmospheric small-scale fluctuations in time is to create a series of atmospheric TOD templates, created from a wide span of atmospheric conditions and fit the data with those templates in order to find the best "atmosphere" conditions that fit the data, and remove the contributions.

Bibliography

Abazajian, K. N., Adshead, P., Ahmed, Z., et al. 2016, arXiv preprint arXiv:1610.02743

Ade, P., Ahmed, Z., Aikin, R., et al. 2016, The Astrophysical Journal, 833, 228

Ade, P. A., Aghanim, N., Ahmed, Z., et al. 2015, Physical review letters, 114, 101301

Ade, P. A., Aikin, R., Barkats, D., et al. 2014, Physical Review Letters, 112, 241101

Albrecht, A. & Steinhardt, P. J. 1982, Physical Review Letters, 48, 1220

Ali, A. M., Adachi, S., Arnold, K., et al. 2020, Journal of Low Temperature Physics, 200, 461

Alpher, R. A., Bethe, H., & Gamow, G. 1948, Physical Review, 73, 803

Barkats, D., Bischoff, C., Farese, P., et al. 2005, The Astrophysical Journal Supplement Series, 159, 1

Baumann, D. 2009, arXiv preprint arXiv:0907.5424

Bersanelli, M. & Mandolesi, N. 2000, Astrophysical Letters and Communications, 37, 171

Birkhoff, G. D. & Langer, R. E. 1923, Relativity and modern physics, Vol. 1 (Harvard University Press Cambridge)

Burigana, C., Danese, L., & De Zotti, G. 1991a, Astronomy and Astrophysics, 246, 49

Burigana, C., De Zotti, G., & Danese, L. 1991b, The Astrophysical Journal, 379, 1

Chernov, L. A. 2017, Wave propagation in a random medium (Courier Dover Publications)

Church, S. 1995, Monthly Notices of the Royal Astronomical Society, 272, 551

Cleary, K. A. 2010, in Millimeter, Submillimeter, and Far-Infrared Detectors and Instrumentation for Astronomy V, Vol. 7741, International Society for Optics and Photonics, 77412H

Coleman, S. 1977, Physical Review D, 15, 2929

Collaboration, K., Ade, P. A. R., Ahmed, Z., et al. 2021, BICEP / Keck XIII: Improved Constraints on Primordial Gravitational Waves using Planck, WMAP, and BICEP/Keck Observations through the 2018 Observing Season

Collaboration, P., Ade, P., Aghanim, N., et al. 2015, XIII. Cosmological parameters

Columbro, F., de Bernardis, P., & Masi, S. 2018, Review of Scientific Instruments, 89, 125004

Coppi, G., De Bernardis, P., May, A. J., et al. 2016, in Advances in Optical and Mechanical Technologies for Telescopes and Instrumentation II, Vol. 9912, SPIE, 1858–1865

Dan Moulton. January 2008, Stokes Parameters, cC BY-SA 3.0, via Wikimedia Commons

De Bernardis, P., Aquilini, E., Boscaleri, A., et al. 1993, Astronomy and Astrophysics, 271, 683

Dodelson, S. 2003, Modern cosmology (Elsevier)

Errard, J., Ade, P., Akiba, Y., et al. 2015, The Astrophysical Journal, 809, 63

Errard, J., Stivoli, F., & Stompor, R. 2011, Physical Review D, 84, 063005

Farese, P. C., Dall'Oglio, G., Gundersen, J. O., et al. 2004, The Astrophysical Journal, 610, 625

Fetter, A. L. & Walecka, J. D. 2012, Quantum theory of many-particle systems (Courier Corporation)

Friedmann, A. 1922, Zeitschrift für Physik, 10, 377

Frisch, U. & Kolmogorov, A. N. 1995, Turbulence: the legacy of AN Kolmogorov (Cambridge university press)

Goldsmith, P. F. 1982, Infrared and millimeter waves, 6, 277

Guth, A. H. 1981, Physical Review D, 23, 347

Hamilton, J.-C., Mousset, L., Battistelli, E., et al. 2022, Journal of Cosmology and Astroparticle Physics, 2022, 034

Hazumi, M., Ade, P., Adler, A., et al. 2020, in Space Telescopes and Instrumentation 2020: Optical, Infrared, and Millimeter Wave, ed. M. Lystrup, M. D. Perrin, N. Batalha, N. Siegler, & E. C. Tong, Vol. 11443, International Society for Optics and Photonics (SPIE), 431 – 450

Hoffman, Y., Pomarède, D., Tully, R. B., & Courtois, H. M. 2017, Nature Astronomy, 1, 1

Hu, W. & White, M. 1997, New Astronomy, 2, 323

Hubble, E. 1929, Proceedings of the national academy of sciences, 15, 168

Hubble, E. & Tolman, R. C. 1935, Ap. J., 82, 302

Kasten, F. & Young, A. T. 1989, Applied optics, 28, 4735

Keihänen, E., Keskitalo, R., Kurki-Suonio, H., Poutanen, T., & Sirviö, A. 2010, Astronomy & Astrophysics, 510, A57

Kisner, T., Keskitalo, R., Zonca, A., Puglisi, G., & Borrill, J. 2020, hpc4cmb/toast: Small fixes discovered post 2.3.11

Kogut, A., Spergel, D., Barnes, C., et al. 2003, arXiv preprint astro-ph/0302213

Kolb, E. W. & Turner, M. S. 2018, The early universe (CRC press)

Kompaneets, A. 1957, Soviet Journal of Experimental and Theoretical Physics, 4, 730

Kosowsky, A. 2003, New Astronomy Reviews, 47, 939

Kovac, J. M., Leitch, E., Pryke, C., et al. 2002, Nature, 420, 772

Krachmalnicoff, N., Baccigalupi, C., Aumont, J., Bersanelli, M., & Mennella, A. 2016, Astronomy & Astrophysics, 588, A65

Kramers, H. A. 1927, Atti del Congresso Internationale dei Fisici, 545

Krönig, R. 1926, J. Opt. Soc. Am., 12, 547

Kurki-Suonio, H., Keihänen, E., Keskitalo, R., et al. 2009, Astronomy & Astrophysics, 506, 1511

La Porta, L., Burigana, C., Reich, W., & Reich, P. 2008, Astronomy and Astrophysics, 479, 641

Landau, L. D. & Lifshitz, E. M. 2013, Quantum mechanics: non-relativistic theory, Vol. 3 (Elsevier)

Lange, A., De Bernardis, P., De Petris, M., et al. 1995, Space Science Reviews, 74, 145

Lawrence, C. R., Gaier, T. C., & Seiffert, M. 2004, in Millimeter and Submillimeter Detectors for Astronomy II, Vol. 5498, SPIE, 220–231

Legg, S., Lamagna, L., Coppi, G., et al. 2016, in Millimeter, Submillimeter, and Far-Infrared Detectors and Instrumentation for Astronomy VIII, Vol. 9914, SPIE, 255–268

Lemaître, G. 1950, The primeval atom: An essay on cosmogony (Gonseth)

Liddle, A. 2015, An introduction to modern cosmology (John Wiley & Sons)

Linde, A. D. 1982, Physics Letters B, 108, 389

LiteBIRD Collaboration, Allys, E., Arnold, K., et al. 2022, JCAP

LIV, P. C. I. 2018, Astronomy&Astrophysics, 619, A94

Mandelli, S., Kisner, T., Keskitalo, R., Zonca, A., & Puglisi, G. 2021, cmbground-based/cal: First official release - v1.0

Mangilli, A., Foënard, G., Aumont, J., et al. 2018, arXiv preprint arXiv:1804.05645

Masi, S., Battistelli, E., de Bernardis, P., et al. 2021, arXiv preprint arXiv:2110.12254

Matsumura, T., Kataza, H., Utsunomiya, S., et al. 2016, IEEE Transactions on applied superconductivity, 26, 1

McGuffie, K. & Henderson-Sellers, A. 2014, The climate modelling primer (John Wiley & Sons)

Molinari, L. G. 2007, Journal of Mathematical Physics, 48, 052113

Montier, L., Mot, B., de Bernardis, P., et al. 2020, in Space Telescopes and Instrumentation 2020: Optical, Infrared, and Millimeter Wave, ed. M. Lystrup, M. D. Perrin, N. Batalha, N. Siegler, & E. C. Tong, Vol. 11443, International Society for Optics and Photonics (SPIE), 451 – 471

Mousset, L., Lerena, M. G., Battistelli, E., et al. 2022, Journal of Cosmology and Astroparticle Physics, 2022, 035

Oguri, S., Choi, J., Damayanthi, T., et al. 2016, in Ground-based and Airborne Telescopes VI, Vol. 9906, International Society for Optics and Photonics, 99063L

P. A. R. Ade, T. P. C., Akiba, Y., Anthony, A. E., et al. 2014, The Astrophysical Journal, 794, 171

Padin, S., Shepherd, M., Cartwright, J., et al. 2001, Publications of the Astronomical Society of the Pacific, 114, 83

Paine, S. 2019, The am atmospheric model

Partridge, R. B. & Partridge, R. 1995, 3K: the cosmic microwave background radiation, Vol. 393 (Cambridge University Press Cambridge)

Peebles, P. 1971, This is a textbook introduction to the"standard"treatment of cosmology, and the whole issue of applying general relativity to cosmology

Penzias, A. A. & Wilson, R. W. 1965, The Astrophysical Journal, 142, 419

Perlmutter, S., Aldering, G., Goldhaber, G., et al. 1999, The Astrophysical Journal, 517, 565

Perlmutter, S. et al. 2003, Physics today, 56, 53

Peverini, O. A., Virone, G., Addamo, G., et al. 2021, 1

Pisano, G., Ade, P., Tucker, C., & Ng, M. W. 2015a, in 2015 40th International Conference on Infrared, Millimeter, and Terahertz waves (IRMMW-THz), IEEE, 1–1

Pisano, G., Ng, M. W., Haynes, V., & Maffei, B. 2012, Progress In Electromagnetics Research M, 25, 101

Pisano, G., Tucker, C., Ade, P. R., Moseley, P., & Ng, M. W. 2015b, in 2015 8th UK, Europe, China Millimeter Waves and THz Technology Workshop (UCMMT), IEEE, 1–4

Planck Collaboration, Aghanim, N., Akrami, Y., et al. 2020, Astronomy & Astrophysics, 641, A6

Pozar, D. M. 2011, Microwave engineering (John wiley & sons)

Presta, G., Ade, P., Battistelli, E., et al. 2020, 1548, 012018

Realini, S., Franceschet, C., Villa, F., et al. 2022, Journal of Instrumentation, 17, P01028

Riess, A. G., Filippenko, A. V., Challis, P., et al. 1998, The Astronomical Journal, 116, 1009

Rubiño-Martín, J. A., Rebolo, R., Tucci, M., et al. 2010, in Highlights of Spanish Astrophysics V, ed. J. M. Diego, L. J. Goicoechea, J. I. González-Serrano, & J. Gorgas (Berlin, Heidelberg: Springer Berlin Heidelberg), 127–135

Samtleben, D. 2008, arXiv preprint arXiv:0806.4334

Sekimoto, Y., Ade, P. A. R., Adler, A., et al. 2020, in Millimeter, Submillimeter, and Far-Infrared Detectors and Instrumentation for Astronomy X, ed. J. Zmuidzinas & J.-R. Gao, Vol. 11453, International Society for Optics and Photonics (SPIE), 189 – 209

Stompor, R., Errard, J., & Poletti, D. 2016, Physical Review D, 94, 083526

Sunyaev, R. & Zeldovich, Y. B. 1970, Astrophysics and Space Science, 7, 20

Tajima, O., Choi, J., Hazumi, M., et al. 2012, in Millimeter, Submillimeter, and Far-Infrared Detectors and Instrumentation for Astronomy VI, Vol. 8452, International Society for Optics and Photonics, 84521M

Tatarski, V. I. 2016, Wave propagation in a turbulent medium (Courier Dover Publications)

Taylor, A., Challinor, A., Goldie, D., et al. 2004, arXiv preprint astro-ph/0407148

The LSPE collaboration, G. A., Ade, P. A. R., Baccigalupi, C., et al. 2020, JCAP

Vaccaro, D., Baldini, A., Cei, F., et al. 2019, Nuclear Instruments and Methods in Physics Research Section A: Accelerators, Spectrometers, Detectors and Associated Equipment, 936, 169

Virone, G., Peverini, O. A., Lumia, M., Addamo, G., & Tascone, R. 2014, IEEE Transactions on Microwave Theory and Techniques, 62, 1487

Watts, D. J., Wang, B., Ali, A., et al. 2018, The Astrophysical Journal, 863, 121

Weinberg, S. 1972, Gravitation and cosmology: principles and applications of the general theory of relativity (Wiley)

Weymann, R. 1965, The Physics of Fluids, 8, 2112

Wick, G.-C. 1950, Physical review, 80, 268

Wu, W. L. K., Mocanu, L. M., Ade, P. A. R., et al. 2019, The Astrophysical Journal, 884, 70

XII, P. C. L. P. C. 2020, Astronomy and Astrophysics, 641, A12

Zeldovich, Y. B. & Sunyaev, R. 1969, Astrophysics and Space Science, 4, 301

Zilic, K., Aboobaker, A., Aubin, F., et al. 2017, Review of Scientific Instruments, 88, 045112